CONCENTRATION POLARIZATION AT MICROFLUIDIC-NANOFLUIDIC INTERFACES

A DISSERTATION
SUBMITTED TO THE DEPARTMENT OF MECHANICAL ENGINEERING
AND THE COMMITTEE ON GRADUATE STUDIES
OF STANFORD UNIVERSITY
IN PARTIAL FULFILLMENT OF THE REQUIREMENTS
FOR THE DEGREE OF
DOCTOR OF PHILOSOPHY

Thomas A. Zangle
February 2010

© 2010 by Thomas Andrew Zangle. All Rights Reserved.
Re-distributed by Stanford University under license with the author.

This work is licensed under a Creative Commons Attribution-Noncommercial 3.0 United States License.
http://creativecommons.org/licenses/by-nc/3.0/us/

This dissertation is online at: http://purl.stanford.edu/rz014nz6164

I certify that I have read this dissertation and that, in my opinion, it is fully adequate in scope and quality as a dissertation for the degree of Doctor of Philosophy.

Juan Santiago, Primary Adviser

I certify that I have read this dissertation and that, in my opinion, it is fully adequate in scope and quality as a dissertation for the degree of Doctor of Philosophy.

John Eaton

I certify that I have read this dissertation and that, in my opinion, it is fully adequate in scope and quality as a dissertation for the degree of Doctor of Philosophy.

Roger Howe

Approved for the Stanford University Committee on Graduate Studies.

Patricia J. Gumport, Vice Provost Graduate Education

This signature page was generated electronically upon submission of this dissertation in electronic format. An original signed hard copy of the signature page is on file in University Archives.

Abstract

Nanofluidic devices have the potential to offer unique functionality by exploiting length scales comparable to the Debye length or the size of individual biomolecules. Integration of nanofluidics with microfluidics also has potential benefits as a system can thereby draw from the benefits of both technologies. To leverage these functionalities, the physics associated with interfacing microchannels and nanochannels needs to be understood rigorously. In particular, when current is applied across a microchannel-nanochannel interface, surface charge effects inside the nanochannel often lead to an imbalance of fluxes of positive and negative species. This, in turn, creates a region of high ionic strength on one side of the nanochannel and low ionic strength on the other side, a phenomena known as concentration polarization (CP). Prior work on the physics of microchannel-nanochannel interfaces has neglected several key issues which we will address in this work.

Our experiments show that CP enrichment and depletion regions can propagate over large distances into and profoundly change the flow and electric field conditions in a microfluidic system. We will outline an analytical model of propagating CP and also present a computational model which captures these effects. We will also present an experimental study of this phenomena and validation of this model. In particular, our results show that enrichment and depletion regions propagate as 'shockwaves' of concentration with a velocity proportional to current through the nanochannel. These shocks can cause order of magnitude changes in the concentration and electric field throughout a microfluidic system.

We will present a model comparing between propagating CP at constant current and constant voltage conditions. We validate this model using computations and experiments. This work demonstrates that, at constant voltage, enrichment and depletion shocks propagate as $x \sim t^{1/2}$.

We will present an analytical model which predicts the behavior of analyte ions in a microchannel-nanochannel system with CP. This work shows that cationic species are appropriate for tracing the location of enrichment and depletion shocks in typical microchannel-nanochannel systems. This work also shows that CP can cause anionic species to accumulate at increased concentration at each of four different interfaces in a microchannel-nanochannel system. We validate this model by comparison to our own work and to published experiments.

Finally, the model for propagating CP also predicts that the concentration inside a nanochannel changes when an electric field is applied. We will present an experimental study which shows that, for some cases, the propagating CP model is a fair predictor of trends in nanochannel concentration. However, in some cases, the concentration inside the nanochannel reaches a temporary 'meso' state before transitioning to a final, significantly different concentration which is not described by theory. The latter shows that there is yet much room for further studies of this phenomenon.

Acknowledgements

This work was sponsored by National Institutes of Health (Contract No. N01-HV-28183) and an NSF PECASE Award (Juan G. Santiago, award number NSF CTS0239080). Thomas A. Zangle was supported by a Regina Casper Stanford Graduate Fellowship.

Work was performed in part at the Stanford Nanofabrication Facility (a member of the National Nanotechnology Infrastructure Network) which is supported by the National Science Foundation under Grant ECS-9731293, its lab members, and the industrial members of the Stanford Center for Integrated Systems.

Table of Contents

Abstract iv

Acknowledgements vi

Table of Contents vii

List of Tables x

List of Illustrations xi

1 Introduction 1

  1.1 Background 1

    1.1.1 Nanochannel and EDL physics 4

  1.2 Prior work on Concentration Polarization (CP) and Microchannel-Nanochannel Interfaces 8

    1.2.1 Concentration Polarization Models and Experiments 8

    1.2.2 Recirculation Effects 8

    1.2.3 Work Describing Ion Concentration 10

    1.2.4 Propagating versus Non-propagating CP and Nanochannel Ion Concentration 12

    1.2.5 Applications 16

  1.3 Thesis work methodology 18

2 Concentration Polarization Effects in Microfluidic Systems 20

  2.1 Introduction 20

  2.2 Numerical Study 25

  2.3 Experimental Setup 28

    2.3.1 Materials and Instrumentation. 28

    2.3.2 Device Fabrication. 30

    2.3.3 Preliminary Quantifications of Electrophoretic and Electroosmotic Mobilities. 30

    2.3.4 CP and Imaging Protocol. 31

  2.4 Results and Discussion 32

    2.4.1 Scaling Derivation from Simple Model. 32

    2.4.2 Numerical Results. 34

2.4.3 Experimental Results. 39
2.5 Section Conclusions 46
3 Effects of Constant Voltage on Time Evolution of Propagating Concentration Polarization 47
3.1 Introduction 47
3.2 Analytical Model 49
3.3 Computational Model 51
3.4 Experimental Measurements 52
3.5 Section Conclusions 56
4 Analyte Species Behavior in Systems with Concentration Polarization 57
4.1 Introduction 57
4.2 Cationic species 60
4.2.1 Analytical predictions 60
4.2.2 Non-propagating CP 64
4.2.3 Propagating CP, $v_2^* \geq 1$ 66
4.2.4 Propagating CP, $v_2^* < 1$ 70
4.2.5 Comparison to results from literature 73
4.3 Anionic species 75
4.3.1 Analytical predictions 77
4.3.2 Depletion shock 86
4.3.3 Depletion Side Microchannel-Nanochannel Interface 89
4.3.4 Enrichment Side Microchannel-Nanochannel Interface 90
4.3.5 Enrichment Shock 91
4.4 Section Conclusions 93
5 Temporal Variations in Nanochannel Conductance and Concentration 94
5.1 Introduction 94
5.2 Experimental Setup 97
5.3 Experimental Results 99
5.4 Summary 103
6 Conclusions and Future Work 105
6.1 Conclusions and Contributions 105

6.2 Recommendations for Future Work 106
7 Bibliography 109
Appendix A Details of Experimental Setup 120
Appendix A.1 Channel Conditioning Procedure 120
Appendix A.2 Channel Fabrication 121
Appendix A.3 Reservoir Attachment 121
Appendix A.4 Imaging Setup and Image Analysis 122
Appendix A.5 Current/Voltage Measurement Setup 125
Appendix A.6 Matlab Code to Read .spe Files 127
Appendix B Supporting Information for Chapter 2 129

List of Tables

Table 2.1 Summary of Experimental Conditions and Measured Values Presented in Figure 2.5 39
Table 4.1 Predicted and Observed Analyte Ion Behaviors. 84
Table 5.1 Summary of experimental results and analytical predictions based on the theory of Mani *et al.*[30] 96

List of Illustrations

Figure 1.1 Schematic of channels with (a) non-overlapped electrical double layers (EDLs) and (b) overlapped EDLs. 7

Figure 1.2 Schematic showing background electrolyte profiles in a typical microchannel-nanochannel geometry for propagating and non-propagating CP. 11

Figure 1.3 Experimental spatiotemporal data showing enrichment and depletion shock waves emanating from both sides of a nanochannel between two microchannels. 13

Figure 1.4 Propagating versus non-propagating CP: Analytical predictions and experimental results from literature. 15

Figure 1.5 Nanofluidic preconcentrator used to increase sensitivity and dynamic range of a bead-based immunoassay.[24] 17

Figure 2.1 Schematic of microchannel-nanochannel-microchannel system. 24

Figure 2.2 Schematic of experimental setup of microchannel-nanochannel-microchannel system. 26

Figure 2.3 Zeta potential measurement results versus Alexa Fluor 488 and sodium-fluorescein concentration. 31

Figure 2.4 Representative simulations and experimental visualizations of ion transport and accumulation in our micro-nano-micro-channel system with 1 μm high microchannels. 36

Figure 2.5 Phase diagram showing CP magnitude, c_5/c_r, from computations versus $c_r^* h_n^*$ and ν_{2n}^* and experimental observations covering the major parametric regimes. 38

Figure 2.6 Measurements of enrichment (a) and depletion (b) shock velocities versus applied current for Alexa Fluor 488 experiments. 43

Figure 2.7 Scaled enrichment region concentration, $c_5/c_r \left(c_r^* h_n^*\right)/\left(c_5^* h_n^*\right)$,versus applied current. 44

Figure 2.8 Background electrolyte enrichment factor, c_5/c_r, versus depletion-to-enrichment shock velocity ratio for 73 realizations. 45

Figure 3.1 Schematic of microchannel-nanochannel system. 48

Figure 3.2 Computational and experimental results showing spatiotemporal plots for constant current and constant applied voltage. 54

Figure 3.3 Computational results for applied potentials of (a) 10 V, (b) 100 V and (c) 1000 V, at otherwise the same conditions as in Figure 3.2(c) and Figure 3.2(d). 55

Figure 4.1 Schematic showing various possibilities of anionic species focusing or stacking in a typical microchannel-nanochannel geometry. 58

Figure 4.2 Summary of results for area-averaged stacking ratios of cationic analytes. 72

Figure 4.3 Summary of results for critical values of ν_i^* for anionic analytes 76

Figure 4.4 Phase boundaries in the field defined by $c_{0,r}^* h_n^*$ versus ν_2^*. $c_{0,r}^* h_n^*$ describes the ratio of bulk conductance to surface conductance. 83

Figure 4.5 Worked example of predictions for anionic analyte behavior 86

Figure 4.6 Experiments showing (a) non-propagating CP with focusing on the depletion side nanochannel and (b) propagating CP with focusing on the depletion shock and stacking on the enrichment shock. 88

Figure 5.1 Analytical results for ratio of final nanochannel concentration to reservoir concentration, c_n/c_r. 96

Figure 5.2 Channel geometries used in nanochannel concentration study. 98

Figure 5.3 Sample experimental results showing current measurements and fluorescence intensity measurements for channels of the design shown in Figure 5.2(a) 100

Figure 5.4 Sample spatiotemporal plot of 100 nm deep, 100 μm long nanochannel between two microchannels (of the design shown in Figure 5.2(b)). 102

Figure A.1 Image of (from left to right) mercury bulb power supply, CCD camera temperature controller, CCD camera gain controller, Keithley sourcemeter. 124

Figure A.2 Image of ICCD camera, 0.31x demagnifier, and Olympus IX70 inverted epifluorescence microscope. 124

Figure A.3 Image of Olympus inverted epifluorescence microscope with the computer used to control the camera and Keithley sourcemeter in the background. 125

Figure A.4 Image of Faraday cage used for microchannel-nanochannel experiments. 126

Figure A.5 Images of copper faraday cage used in microchannel-nanopore experiments. 127

Figure B.1 Measured spatiotemporal plots showing the effect of increasing current density. 130

Figure B.2 Measured spatiotemporal plots showing several anomalous behaviors of propagating CP fronts. 131

1 Introduction

Some of the contents of this chapter (sections 1.1.1-1.2.5) have been accepted for publication by *Chemical Society Reviews* (Zangle, T. A., Mani, A., and Santiago, J. G., "Theory and experiments of concentration polarization and ion focusing at microchannel and nanochannel interfaces," Chemical Society Reviews, 2010, DOI: 10.1039/b902074h, http://xlink.rsc.org/?doi=B902074H.)[1] and are reproduced here by permission of The Royal Society of Chemistry with minor modifications.

1.1 Background

Microfluidics is a field which seeks to build miniaturized tools for biological and chemical analysis. These miniaturized devices have fluidic channels with typical length scales of 1-100 μm and, among other possible benefits, offer the potential for:[2-3]

1. high throughput through parallelization,
2. small (μL to nL) sample volume,
3. shortened analysis time,
4. integration of many components into one compact device, and
5. exploitation of novel physics to enable new functionalities.

In a typical microfluidic system, multiple different fluidic elements are connected in series to detect a specific substance present in a sample fluid. An example of this type of microfluidic system was fabricated by Easley *et al.*[4] for detection of bacteria in blood samples. The Easley *et al.* device checks for the presence of bacterial DNA as a marker of infection. In operation, first, 750 nL of blood mixed with buffer (ions introduced to the system to control the pH and ionic strength) are introduced into an inlet fluid reservoir. The initial buffer lyses the cells present in the blood. Second, the solution flows through a channel section used for extraction of DNA, and third, the solution flows through a channel section where polymerase chain reaction (PCR) is performed to amplify the DNA. By choice of the primers for PCR, PCR can be tuned to only amplify DNA from a specific type of bacteria. The final stage is to apply an electric field and check for the presence of amplified bacterial DNA labeled with a fluorescent marker as it flows past a detector.

The Easley *et al.* device illustrates many of the elements of microfluidic devices used for sample analysis. First, the fluid in the system is essentially water (the blood sample is diluted in large volumes of buffer before it is introduced and during analysis) containing some initial concentration of background electrolyte (BGE) salt ions (about 100 mM in this case). Second, The Easley *et al.* device is designed to detect a specific sample ion, or analyte which is initially present in low concentration, DNA in this case. Third, the device uses a method (here, PCR) to preconcentrate, or increase the concentration of, the sample before the final detection step.

Since typical microfluidic systems consist mainly of water filled with electrolytes (typically high concentration BGE ions and low concentration sample ions) the study of ion transport and electrokinetics in these systems has focused on analogous systems.[5-9] A primary reason for fundamental work on electrokinetics is to optimize and control the basic elements of sample analysis in microfluidic systems.[5,8,10] Prior work has shown, for example, that in a system with a discontinuous background electrolyte, shock waves of ion concentration can form and propagate at a rate proportional to the current through the system.[10] These shock waves have a profound impact on sample ion transport in microfluidic systems and have been used, for example, to separate and detect nonfluorescent ionic species.[11]

Nanofluidics typically refers to the study of fluidic devices with length scales on the order of 1-100 nm. The primary reason to study devices at this length scale is to exploit unique physics. This is because channel sizes of 1-100 nm are on the order of the Debye length,[12-13] biomolecule size,[14-15] or the dimension at which the number of ions associated with charged nanochannel surfaces is comparable to the number of ions inside the channel in the absence of wall charge.[1,16-17] Among other applications, nanofluidic devices have been used to perform free-solution separations[13,18] and to count and characterize individual proteins or DNA molecules.[14-15,19]

A variety of fabrication techniques are now available to construct nanofluidic devices and interface them with microfluidic systems.[20-23] This has motivated the study of nanofluidic devices as modules within microfluidic systems (as a substitute for one of the modules in the Easley *et al.*[4] system, for example) to preconcentrate analytes[20,24-25] or detect and analyze DNA.[26] However, application of an electric field across a nanofluidic device creates regions of enriched and depleted (net neutral) ion concentration, an effect called concentration polarization (CP). CP can change the conductivity and electric field in adjoining microchannels by orders of magnitude[27] which, in turn, influences sample transport throughout these systems.[28-29] Recent work has shown that CP enrichment and depletion zones can propagate through hybrid microchannel-nanochannel devices and profoundly affect the global behavior of the system.[21,30]

CP occurs when an electric field is applied across a nanofluidic device located between larger dimension reservoirs or microchannels. In electrokinetic nanochannels, the number of diffuse ions associated with electric double layers (EDLs) is often of the same order as the number of ions in the background electrolyte (BGE) solution. This leads to an imbalance of current transport by positively charged (cationic) and negatively charged (anionic) ions.[29,31-33] In contrast, in typical microchannels, the number of ions associated with EDLs is low relative to the number of background ions. Therefore, for a symmetric electrolyte, current in a microchannel is carried equally by cations and anions. So, as when current passes from a nanochannel with negative wall charge, where a large proportion of current is carried by cations, into a microchannel, where current is carried roughly equally (for similar mobility positive and negative species) by cations and anions an ionic flux imbalance results at each interface. At the side closer to the positive electrode (anode), ions of both signs are depleted and at the side closer to the negative electrode (cathode) ions of both signs are enriched. The formation of net-neutral regions of high and low concentration on either side of a nanofluidic device (or nanoporous membrane or nanoscale material) is called concentration polarization.

In this dissertation we will examine the effects of CP on BGE concentration and sample ion transport in microfluidic systems with axial variation in channel height. We will see that, similar to the case of microfluidic systems with variations in buffer properties,[10] under certain conditions, a microfluidic-nanofluidic system will create shock waves of ion concentration proportional to the current through the system.[21,30] This finding has important implications for the design of hybrid microfluidic-nanofluidic systems. In some cases, for example, where sample ions need to be detected as they pass through a nanofluidic device,[15] CP shock waves should be avoided because they may disrupt sample transport and overall device operation. In other cases, CP shock waves can be desirable and used to focus and preconcentrate sample ions.[16,24] In this dissertation we will present results of an in depth experimental, computational, and analytical study of CP in hybrid microfluidic-nanofluidic systems in order to better design and use these systems.

Note that we here consider electrokinetic CP in microchannel systems caused by forcing current through a nanochannel or a nanoporous membrane. There are at least two other physical phenomena which are commonly referred to as concentration polarization and which are not the topic of this review. These include solute buildup at a (steric) filter membrane[34] or performance losses in a fuel cell due to the concentration of reactants.[35]

1.1.1 Nanochannel and EDL physics

In this section we will review nanochannel electrokinetics as it pertains to concentration polarization at a microchannel-nanochannel interface including brief scaling arguments which highlight key physical effects. CP occurs when current flows into or out of an electric double layer (EDL) shielding a charged surface. The common case is when ionic current passes from a microchannel into a nanochannel. In the nanochannel, a significant portion of the current is carried by the EDL which, unlike the bulk solution, has an appreciably different number of negative versus positive charges. This deviation from bulk conductance is well known and has been characterized experimentally.[36-38] We can use a formulation of this deviation from bulk conductance to show that the primary parameter that governs CP is a type of Dukhin number, relating bulk and surface conductances. This is consistent with the analytical model we presented[30] in which a type of Dukhin number appears as a nondimensional parameter in the differential equations governing CP. This is also consistent with our experimental results showing that using a Dukhin number can predict accurately the behavior of CP enrichment and depletion regions.[21]

Neglecting for the moment current due to diffusive fluxes, ion current through a wide, shallow (micro or nano) channel can be written as a sum of advection and electromigration current as:

$$I = w\sum_i \left[\int_0^h \left(Fz_i c_i\left(y\right) U^{bulk}\left(y\right)\right) dy + \int_0^h \left(F^2 z_i^2 \nu_i c_i\left(y\right) E\right) dy \right], \qquad (1.1)$$

where w is the width of the channel; h is the channel height; F is Faraday's constant; z_i, and ν_i, are the valence and mobility of the ith species; c_i is the concentration of the ith species which can vary with channel location; E is the external electric field; and U^{bulk} is the bulk velocity. In the thin electric double layer (EDL) limit the total channel conductance, $G_{tot} = I/E$ can be estimated for a symmetric electrolyte as:

$$G_{thinEDL} \approx 2z^2 F^2 \nu c_0 wh, \qquad (1.2)$$

where c_0 is the concentration outside of the EDL. Eqn (1.2) is the definition of bulk conductance, so $G_{thinEDL} = G_{bulk}$. Similar to the analysis of Stein *et al.*[36], and for simplicity, we impose a boundary condition of constant and uniform wall charge, σ, and take the limit of eqn (1.1) for thick EDLs (i.e., the limit of $h/\lambda_D \ll 1$), we obtain an expression for the surface conductance:

$$G_\sigma \approx |\sigma| 2Fz\nu w\left(1 + \frac{|\sigma| h}{6Fz\nu\eta}\right). \qquad (1.3)$$

In eqn (1.3), the second term in parentheses indicates the effects of electroosmotic transport on current and is briefly derived in Appendix I. Schoch *et al.*[37] modeled the total conductance of a nanochannel as the sum of a bulk conductance term (as in eqn (1.2)) and a surface conductance term (as in eqn (1.3) but without the advective current component) and found a good fit to experimental data. Following this approach, and neglecting the advective current contribution, we can take the ratio of eqn (1.2) to the leading term of eqn (1.3) to obtain a good indication of the relative importance of bulk conductance, G_{bulk}, to surface conductance, G_{σ}:

$$\frac{G_{bulk}}{G_{\sigma}} \approx \frac{Fhzc_0}{\sigma}. \tag{1.4}$$

Eqn (1.4) is an inverse Dukhin number, for a symmetric, monovalent electrolyte, and is equal to the more general parameter used by Mani *et al.*[30] and Zangle *et al.*[21] in descriptions of CP. This scaling has also been noted by Kim *et al.*[20] for microchannel-nanochannel CP and Lyklema[39] for CP around a spherical particle.

Importantly, CP depends primarily on Dukhin number, and not the ratio of channel height to the Debye length, h/λ_d.[21,30] We note h/λ_d is often quoted as a key parameter in the determination and characterization of CP, but we find this parameter is in fact not nearly as useful as $Fhzc_0/\sigma$, which relates the number of ions in the bulk to the number of ions associated with EDLs. Also, we note that overlapped EDLs (h/λ_d of order unity or less) are often cited as a requirement of (or as being correlated with) CP,[24,27,31-33] but this is not true. From simple Boltzmann distribution arguments, EDL mobile counter ion density scales as $c_0 \exp(-\zeta ez/kT)$ where ζ is the zeta potential and c_0 is the bulk concentration far from the wall.[30,40] For typical glass or silica surfaces, with zeta potentials of roughly -100 mV, this implies near-wall counter ion densities can be order 50-fold higher than the bulk. Therefore, as shown in Figure 1.1, such systems can have values of $Fhzc_0/\sigma$ significantly smaller than unity even for h/λ_d values of 10 or more. For example, strong CP effects have been reported for h/λ_d values of greater than 100.[17]

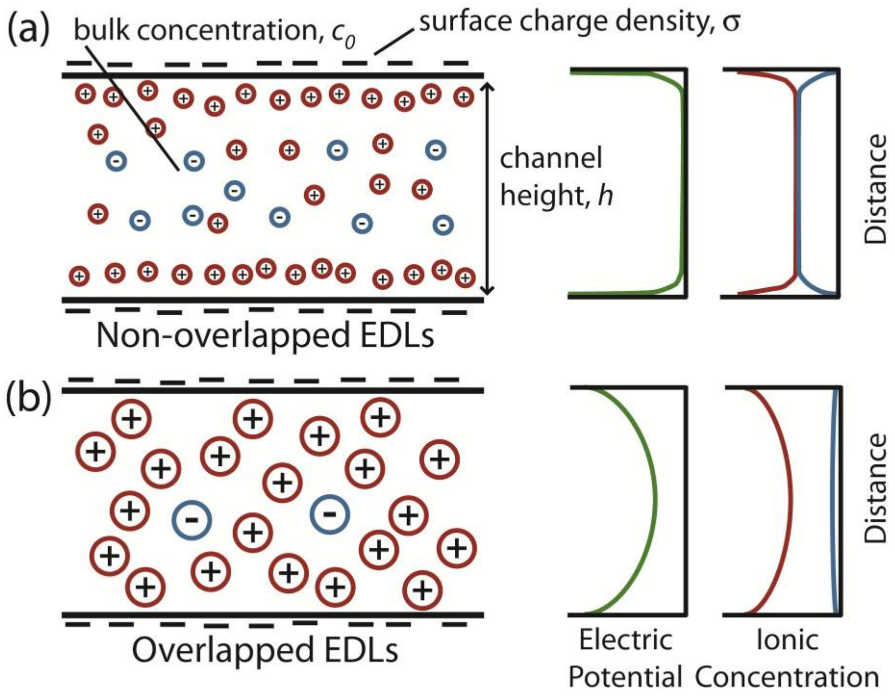
(a)
bulk concentration, c_0
surface charge density, σ
channel height, h
Distance
Non-overlapped EDLs
(b)
Distance
Overlapped EDLs
Electric Potential
Ionic Concentration

Figure 1.1 Schematic of channels with (a) non-overlapped electrical double layers (EDLs) and (b) overlapped EDLs. In channels with EDLs of finite thickness (b), there can be a much greater concentration of positive ions than negative ions. If the EDLs are overlapped, then the potential at the center of a channel does not fall to zero. In a channel with non-overlapped EDLs (a), the electric potential caused by the wall charge falls to zero at the center of the channel. However, the total number of counter-ions to the wall charge(positive ions for negatively charged walls) can still be much greater than the concentration of co-ions when $Fhzc_0/\sigma$, (where c_0 is bulk concentration, h is channel height, z is ion valence, F is Faraday's constant and σ is surface charge density) is significantly smaller than unity. $Fhzc_0/\sigma$ is similar to an inverse Dukhin number, describing the number of ions in the center of the channel relative to the number of ions associated with the EDLs. We note that strong CP effects have been demonstrated in literature for systems with non-overlapped EDLs and $Fhzc_0/\sigma \ll 1$.[17] Figure adapted from Karnik *et al.*[41]

1.2 Prior work on Concentration Polarization (CP) and Microchannel-Nanochannel Interfaces

1.2.1 Concentration Polarization Models and Experiments

CP has been studied extensively in the context of colloids[39,42] and membranes.[43-45] In early work on membrane CP, Block and Kitchener[43] studied nanoporous materials and speculated on the role of water dissociation in the low-concentration depletion regions. In a seminal CP contribution, Dukhin and Shilov[42] presented a simplified description of CP based on a model with very thin EDLs that carry current due to surface conduction. Their model showed that CP occurs when electric field lines cross from net neutral, bulk solution, into electrical double layers. More recent work has shown that electrokinetic instabilities can cause systems with nanoporous membranes to have higher ("overlimiting") conductance than the limit dictated by ion diffusion.[46] Tallarek and coworkers have examined CP in beds of porous beads and glass monoliths.[47-48] See the review by Höltzel and Tallarek[49] for more information on CP around nanoporous membranes, packed beds, and glass monoliths.

In microfluidic systems, Pu *et al.*[31] showed the first reported visualization of CP near nanochannels and presented a qualitative model describing CP. Major themes of research on microfluidic-nanofluidic interfaces since this work have been the study of recirculation zones and the effects of CP on the concentration of ionic species. We review this research in the following sections.

1.2.2 Recirculation Effects

Recirculation near microfluidic-nanofluidic interfaces has been noted in several studies[27,30,32,50-51] and at least three different physical origins of this recirculation have been noted. Park *et al.*[50] presented an analytical model suggesting two different mechanisms for the formation of vortices at a gradual microchannel to nanochannel constriction. Though this model neglects the effects of CP on the background electrolyte concentration, it does capture two possible mechanisms for vortex generation at a microchannel-nanochannel interface. First, surface conductance causes the ratio of ionic current to bulk flow to vary with changes in the channel cross-sectional area. Second, the effects of finite EDLs cause the electroosmotic flow (EOF) velocity profile to be non-uniform across a microchannel-nanochannel interface. Both of these effects create internal pressure gradients. The analysis of Park *et al.* demonstrates that these internal pressure gradients can create vortices at the channel centerline, along the channel walls, or in both regions.[50] Similar vortices were noted in the computational results of Mani *et al.*[30] and Postler *et al.*[51] Postler *et al.*[51] also examined the coupling of CP and electroosmotic flow. The latter two studies found that an adverse pressure gradient can lead to local flow reversal and the formation of eddies near microchannel-nanochannel interfaces.

The work of Zaltzman, Rubinstein, and co-workers[44,46] suggests that electrokinetic flow instability is another possible mechanism for the formation of vortices at a microfluidic-nanofluidic interface. This work has focused on nanoporous membrane systems in which current is observed to initially increase linearly with increasing applied electric field up to a point where current through the membrane becomes limited by diffusion through the depletion region. This is called the "limiting current" regime. Zaltzman, Rubinstein, *et al.*[44,46] demonstrated that a fluid instability is responsible for mixing the depletion region (with fluid regions of less depleted ion density) at electric fields beyond the limiting current regime. Mixing due to instability at high electric fields reduces the resistance of the depletion region, resulting in a notably higher current through the nanoporous membrane, which is called "overlimiting current." See Zaltzman *et al.*[46] for more details on overlimiting current in membrane systems. Kim *et al.*[32] studied overlimiting current in microchannel-nanochannel systems and found that the observed behavior of analyte molecules in the depletion region was correlated to changes from limiting to overlimiting current behavior. Recent work by the same group[27] studied the physics of the depletion region in a nanofluidic preconcentrator where recirculation was observed. From measurements made using microfabricated electrodes the authors estimated the electric field in the depletion region to be up to 33 times higher than the nominal electric field applied to their device.

1.2.3 Work Describing Ion Concentration

Plecis *et al.* described different focusing and stacking[*] regimes of analyte species using a computational model.[28] In simultaneous work, we presented stacking and separation of two low concentration anionic species on a CP enrichment shock.[29] These two species were assumed to be low concentration relative to the background electrolyte (BGE) so that they do not affect the dynamics of CP and the axial electric field. This work included an analytical model for stacking of an anionic species on the enrichment shock. In the following sections, we will present a generalization of this model which describes ion behavior at each region indicated in Figure 1.2. Figure 1.2 shows computations[21] for the concentration of a background electrolyte (dominant ion) in a microchannel-nanochannel system resulting from CP as black lines.

---

[*] Consistent with Bharadwaj *et al.*,[7] we use focusing to describe the condition where there is a focal point for the analyte. A focal point is a point or region in some reference frame where the drift velocity of the focused species changes sign so that sample is driven to the focal point. We use “stacking” to describe the less stringent situation where an analyte drift velocity decreases in magnitude (causing an increase in concentration) as the analyte migrates through some stacking region containing an electric field gradient.

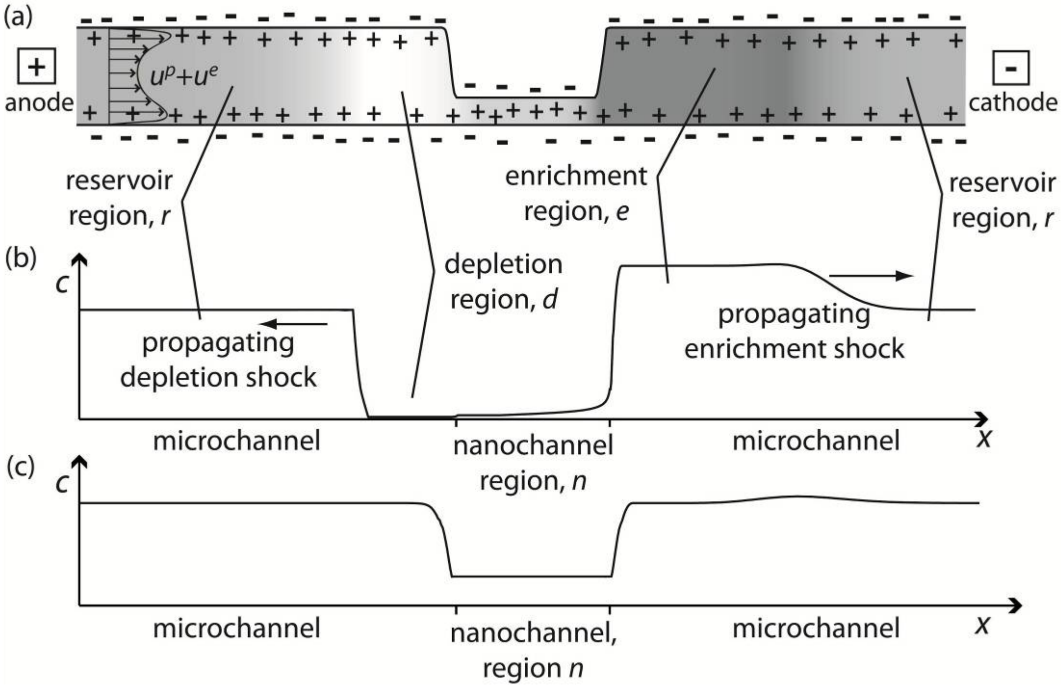
(a)
u^p+u^e
anode
cathode
reservoir region, r
depletion region, d
enrichment region, e
reservoir region, r
(b)
c
propagating depletion shock
propagating enrichment shock
microchannel
nanochannel region, n
microchannel
x
(c)
c
microchannel
nanochannel, region n
microchannel
x

Figure 1.2 Schematic showing background electrolyte profiles in a typical microchannel-nanochannel geometry for propagating and non-propagating CP. (a) shows a typical microchannel-nanochannel-microchannel layout with enrichment and depletion of the background electrolyte (BGE) for a propagating CP case shown as a greyscale map (darker regions correspond to enrichment). The 'reservoir' region is the section of microchannel which is not yet affected by progress of CP front; therefore, the concentration of each ion in this region is equal to the concentration inside of the end-channel reservoir (not shown). (b) and (c) show computed BGE concentration from a propagating and non-propagating CP case, respectively.[21]

We also recently presented an analytical description of the behavior of the background electrolyte (BGE) in microchannel-nanochannel systems.[21,30] In particular, our model shows that, under certain conditions, enrichment and depletion zones in a microfluidic system propagate outwards from nanochannel interfaces. We supported our model with experiments and computations and found it to be a good qualitative predictor of the behavior of CP zones, and a fair-to-good predictor of the quantitative limits of the associated regimes. In order to provide a framework for comparing as many experimental cases as possible, we will use the most general analytical theory of CP in a channel system to date, which was presented by Mani *et al.*[30] In the following sections, we will look at experimental results in the context of this binary electrolyte theory's predictions of CP propagation.

1.2.4 Propagating versus Non-propagating CP and Nanochannel Ion Concentration

In this section, we summarize the physical regimes which lead to the propagation of CP zones away from nanochannels and regimes which lead to non-propagating CP. In a two-paper series, Mani *et al.*[30] and Zangle *et al.*[21] developed and tested a simplified model of charged species transport in a series microchannel-nanochannel-microchannel system. We showed that concentration polarization (CP) enrichment and depletion zones will propagate as shock waves if the following condition is satisfied:

$$c_{0,r}^{*}h_{n}^{*} < \max(\nu_{2}^{*}, 2\nu_{2}^{*} - 1) \tag{1.5}$$

where $c_{0,r}^{*}h_{n}^{*} = (\nu_1 z_1 - \nu_2 z_2)Fh_n c_{0,r} / (-2\nu_1 \sigma)$ is an inverse Dukhin number which describes the ratio of bulk to surface conductance, and $\nu_2^{*} = \nu_2 z_2 F\eta / \zeta_n \varepsilon$ is the mobility of the co-ion (to the wall charge) nondimensionalized by the electroosmotic mobility. Here, $c_{0,r}$ is the BGE reservoir concentration. h_n is the nanochannel height; ν_1 and ν_2 are the mobilities of the positive and negative species; z_1 and z_2 are the valences of the positive and negative species, σ is wall charge, ζ is the zeta potential, F is Faraday's constant, ε is permittivity and η is viscosity.

The enrichment and depletion shock waves predicted by Mani *et al.*[30] are sharp, propagating boundaries between regions of the microchannel where concentration has been influenced by the nanochannel and regions which are still at the initial, reservoir concentration. These shocks are clearly seen in plots of concentration versus time and axial dimension as in Figure 1.3 below. In Figure 1.3, the depletion shock on the left separates the low concentration (black) depletion region from undisturbed regions. Similarly, the enrichment shock on the right is the moving boundary between the high concentration (white or yellow) region and the undisturbed region. For a constant applied current through the nanochannel, these shocks will propagate at constant rates to the reservoirs at the end of the microchannels.[21]

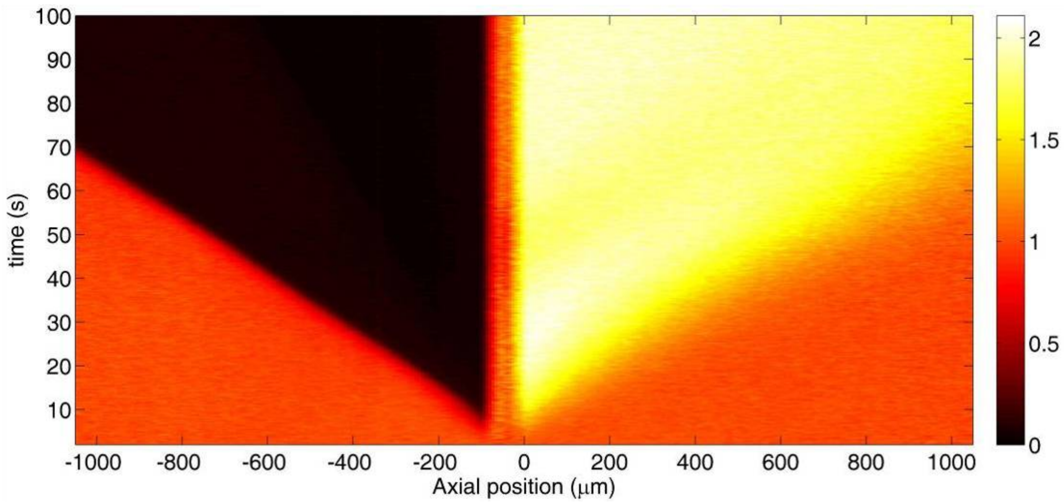

Figure 1.3 Experimental spatiotemporal data showing enrichment and depletion shock waves emanating from both sides of a nanochannel between two microchannels. This plot shows width-averaged fluorescence intensity (using a colormap) as a function of axial position (x-axis) and time (y-axis). Electric field was applied from left (anode) to right (cathode). In this constant-current experiment the enrichment region spreads towards the cathode (on the right) at constant velocity and the depletion region spreads at constant velocity towards the anode (to the left). The nanochannel is located between x = -100 and 0 μm. Adapted from Zangle *et al.*[21]

Mani *et al.*[30] gave predictions of both the dynamics and steady state values of ion concentrations in the microchannel and the nanochannels. For non-propagating CP, the final values achieved in the microchannel and nanochannel are

$$c^*_{0,d} = c^*_{0,e} = c^*_{0,r} \text{ and } c^*_{0,n} = c^*_{0,r} - \nu^*_2 / h^*_n , \tag{1.6}$$

where the subscripts *d*, *e*, *r* and *n* refer to the regions shown in Figure 1.2. For propagating CP, there are two relations corresponding to two ranges of $\nu^*_{2,n}$. For propagating CP with $\nu^*_2 < 1$,

$$c^*_{0,d} = c^*_{0,n} = 0 \text{ and } c^*_{0,e} = \nu^*_2 / h^*_n . \tag{1.7}$$

While for propagating CP with $\nu^*_2 \geq 1$, we have

$$
\begin{aligned}
c_{0,d}^{*} &= \left(\nu_2^{*}-1\right)^2 \Big/ \left[\left(2\nu_2^{*}-1\right) h_1^{*}\right], \\
c_{0,n}^{*} &= \left(\nu_2^{*}-1\right) \Big/ h_n^{*} \text{ and} \\
c_{0,e}^{*} &= \left(2\nu_2^{*}-1\right) \Big/ h_n^{*} .
\end{aligned}
\tag{1.8}
$$

The final concentrations inside microchannels and nanochannels given by eqns (1.6)-(1.8) in turn establish the electric field distribution in a microchannel-nanochannel systems with CP.

The existence condition for propagating CP defined by Eqn (1.5) is plotted as a solid line in Figure 1.4. The region below this phase line indicates conditions which lead to CP with propagation, while the region above denotes non-propagating CP. The phase line is plotted here over the range of most interest in experiments (see discussions of experimental data below). The mobility ratio ν_2^{*} is typically between 0.1 and 10, since electrophoretic and electroosmotic mobilities are typically within a factor of 10 of each other. The parameter with greatest influence is $c_{0,r}^{*} h_n^{*}$, the bulk-to-EDL conductance ratio. This parameter is proportional to nanochannel height and background electrolyte (BGE) reservoir concentration and inversely proportional to surface charge density; so that interesting values span more than 4 orders of magnitude.

In Figure 1.4 we also compare eqn (1.5) to published results from 56 sets of experiments reported in the literature. These data represent 43 unique values in the ν_2^{*} vs. $c_{0,r}^{*} h_n^{*}$ phase plot. For each experimental result, if the reported and/or presented data indicated propagating CP, then we show that data point in Figure 1.4 with an open symbol. We used a closed symbol for reports indicating non-propagating CP.† Zeta potentials for SiO$_2$, PET and PDMS were estimated using the data and curve fits in Kirby *et al.*[60-61] Zeta potential for HEMA hydrogel[33,56] was estimated using data from Kuo *et al.*[62] and You *et al.*[63] using a curve fit of the form $\zeta/\log(c) = A \cdot pH + B$.[61] Zeta potential of Nafion 117 was estimated using data from Ge *et al.*[64] and Daiko *et al.*[65]

---

† Most reported experiments show visualization of a fluorescent species in low concentration relative to a non-fluorescent background electrolyte. Therefore, in such cases we looked for evidence of propagating or non-propagating CP of the background electrolyte by observing the behavior of the fluorescent analyte species. The expected behaviors for low concentration (analyte) species in propagating and non-propagating CP are described in Chapter 4.

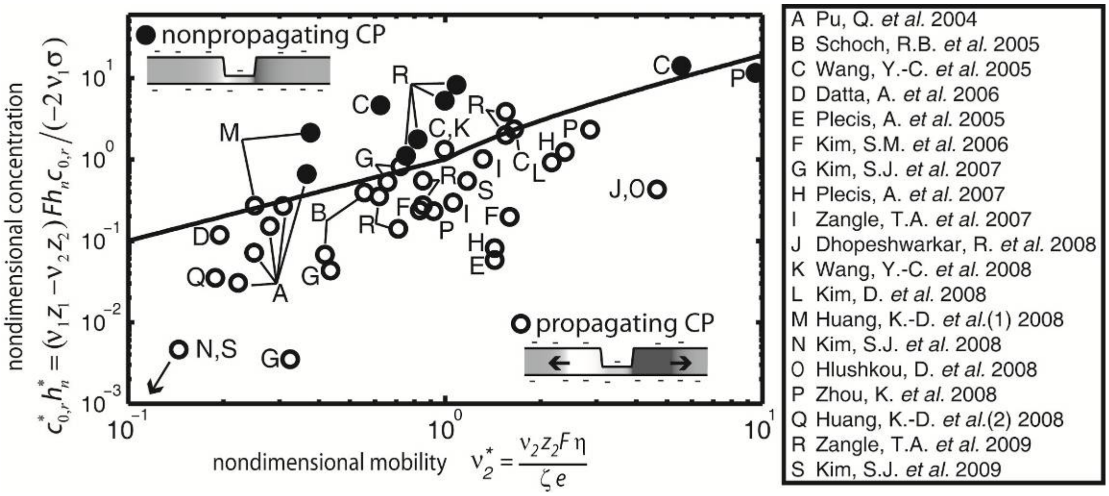

Figure 1.4 Propagating versus non-propagating CP: Analytical predictions and experimental results from literature. Propagating CP is predicted when the experimental condition lies below the solid line phase boundary, as predicted by Mani *et al.*[30] Symbols are data from 56 sets of reported experiments representing 43 unique values of ν^*_2 and $c^*_{0,r}h^*_n$ pairs.[16-17,20-22,24,27,29,31-33,52-59] Open symbols represent reported results consistent with propagating CP, closed symbols represent results consistent with non-propagating CP. Two reported propagating cases, N and S, lie out of the range of this figure (each used highly charged Nafion 117). The analytical model is a fairly good predictor of the propagation regime

Figure 1.4 shows that the analytical theory of Mani et al.[30] is a fairly good predictor of propagation behavior despite the simplifying assumptions made in deriving the model (for instance, the model assumes EDLs which are infinitely thin but which carry significant current, therefore, the definition of ν^*_2 does not include any nanochannel height effects). Because the model is presented in terms of two non-dimensional parameters, it is useful as a design tool for a wide range of experimental conditions. Figure 1.4 also shows that $c^*_{0,r}h^*_n$, a nondimensional concentration (inverse

Dukhin number), is the major parameter determining propagating vs. non-propagating CP. The parameter $c_{0,r}^{*}h_{n}^{*}$ varies over many orders of magnitude, while ν_{2}^{*} is typically of order unity. Therefore, to avoid the effects of propagating CP, a rule of thumb is to keep $c_{0,r}^{*}h_{n}^{*} \gg 1$. If propagating CP is desirable for operation of a microchannel-nanochannel device, as is the case with some nanofluidic preconcentrators,[16,20,22,24] then the rule of thumb is to insure that $c_{0,r}^{*}h_{n}^{*} \ll 1$. In cases where $c_{0,r}^{*}h_{n}^{*} \sim 1$ the designer should either consult the analytical theory[30] or perform a computation using the specific conditions to be used.[21,28,30,33]

As noted earlier, this theory assumes infinite $Pe\,L/h$. Mani *et al.*[30] provide a brief description of the effects of finite $Pe\,L/h$ on propagating CP. $Pe\,L/h$ effects may explain some reported observations including, for example, enrichment regions which first propagate and then stop in series microchannel-nanochannel-microchannel devices.[56] Additionally, Plecis *et al.*[28] showed that the applied potential is an important component of the regime 'map' of possible preconcentration regimes. This suggests that, in addition to the two nondimensional parameters considered in this description of the background electrolyte, ν_{2}^{*} and $c_{0,r}^{*}h_{n}^{*}$, a third nondimensional parameter related to diffusion effects may be important. Based on the results of Plecis *et al.*[28] and the description of Peclet number effects in Mani *et al.*,[30] we suggest that this additional parameter may be a Peclet number, which likely controls the thickness of enrichment and depletion shocks.

1.2.5 Applications

In this section, we present several example applications of CP in devices which are tools for analysis of chemical and biological species or fluid pumping. The main application of CP has been for on-chip sample preconcentration.[66] In a 2005 paper, Wang *et al.*[16] used current through a nanochannel to create a CP depletion zone, and then focus protein on the boundary between the depletion zone and a region of the microchannel at the reservoir concentration. This technique requires that the preconcentrator use a different geometry than the serial microchannel-nanochannel-microchannel geometry considered here. The Wang *et al.*[16] device has two independently-controlled, anode-side channels so that an electroosmotic flow can be directed perpendicular to the axis of the nanochannel (see, for example, a similar device used for analyte ion focusing shown in Figure 1.5). We hypothesize that, with this geometry, the depletion shock can be immobilized by adjusting the ratio of current across the two anode side channels (which controls bulk flow rate) to the current through the nanochannel (which controls the depletion region shock velocity). The Wang study reported 10^6-10^8 fold increase in concentration of a target protein, GFP (although we believe that at least the higher preconcentration value is an overestimate). In a similar study at University of Michigan, Kim *et al.*[20] used irreversible PDMS-glass bonding as a different method to create charged nanofluidic slits and reported 10^3-10^6-fold increase in fluorescence intensity.

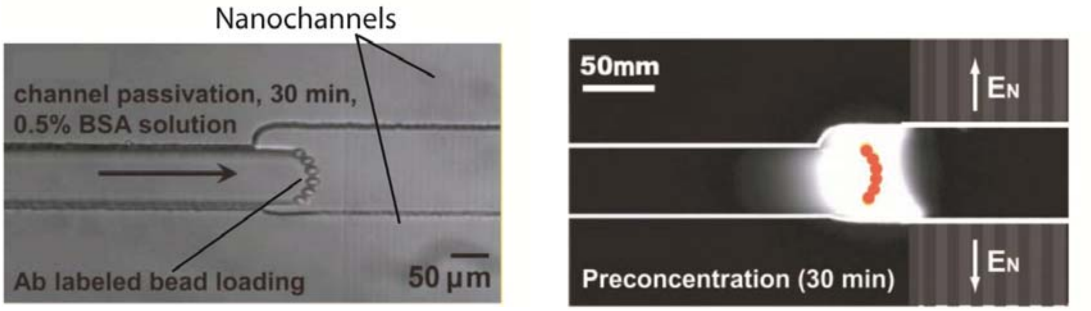
Nanochannels
channel passivation, 30 min, 0.5% BSA solution
Ab labeled bead loading
50 µm
50mm
E_N
E_N
Preconcentration (30 min)

Figure 1.5 Nanofluidic preconcentrator used to increase sensitivity and dynamic range of a bead-based immunoassay.[24] Antibody-labeled beads are loaded into the microchannel and held in place adjacent to the anode side of the nanochannels used for preconcentration (top image). When an electric field is applied, a zone of focused analyte forms on top of the immobilized beads, increasing the antibody-antigen binding rate. Adapted with permission from Wang *et al.*[24] Copyright 2008, Royal Society of Chemistry.

Since the first demonstration of basic microfluidic-nanofluidic CP preconcentrators, there have been a number of other applications of CP-based sample preconcentrators.[16,20,22,24,67-68] For example, Wang *et al.*[24] reported increased range and 500-fold improvement in sensitivity of immuno detection using immobilized, antibody labeled beads. In that study, the authors immobilized labeled beads and stopped the depletion shock at the same location inside the anode-side microchannel. The device then preconcentrated antigens using focusing on the strong electric field gradients of the depletion shock, which increased the rate of binding to antibody labeled beads.

Kim *et al.*[59] used vortices generated at a microchannel-nanochannel interface to create a mixing device. This device consisted of a set of parallel nanochannels connected to a U-shaped microchannel. Here, the strong electric field gradients at the depletion shock boundary are used to create strong vortices which mix the two fluid streams.

Finally, the nonlinear behavior of electroosmotic flow in the depletion region can be used to create an induced zeta potential which is proportional to the applied electric field, a phenomena called non-equilibrium electroosmosis, or electroosmosis of the second kind.[49] In flows of this kind, the total fluid velocity is proportional to electric field squared. This is in contrast to equilibrium electroosmosis where zeta potential is static and fluid velocity is directly proportional to the applied electric field. This has lead to work on using CP effects to pump fluids. In particular, in a device using nonequilibrium EOF Kim *et al*. [27] report a 5-fold increase in volumetric flow rate relative to a similar device using equilibrium electroosmosis.

1.3 Thesis work methodology

The main objectives of this dissertation are to provide the field of microchannel-nanochannel electrokinetics with:

1. An experimental study of CP and the effects of propagation in a model microchannel-nanochannel-microchannel system
2. Validation of the analytical theory of Mani *et al.*[30] for the effects of CP on microchannel concentration using experiments and computations.
3. An experimentally validated analytical model of the time evolution of CP in systems held at constant voltage.

4. An analytical model (and qualitative observations in support) of the effects of CP on analyte transport in microchannel-nanochannel systems
5. Presentation of the first simultaneous measurements of nanochannel concentration and conductance and evalutation of the theory of Mani *et al.*[30] for describing the effects of CP on nanochannel concentration.

This dissertation is organized into five main chapters. Chapter 2 presents results of an experimental study of CP effects on microchannel concentration in a system at constant applied current. Chapter 3 examines the effects of constant voltage conditions on the time evolution of CP. Chapter 4 presents an analytical model for analyte transport in systems with CP and validates this model using results from the literature. Chapter 5 presents experiments in which changes in concentration inside a nanochannel were measured over time and compares these measurements to analytical predictions. Chapter 6 provides a list of contributions of this work as well as recommendations for future work extending the results of this dissertation.

2 Concentration Polarization Effects in Microfluidic Systems

The contents of this chapter were previously published (Zangle, T. A., Mani, A., and Santiago, J. G., "On the propagation of concentration polarization from microchannel-nanochannel interfaces part II. Numerical and experimental study," Langmuir, vol. 25, pp. 3909-3916, 2009)[21] and are reproduced here with minor modifications.

2.1 Introduction

In electrokinetic nanochannels, the number of diffuse ions associated with electric double layers (EDLs) is of the same order as the number of background ions, leading to an imbalance of current transport by counter- and co-ions.[29,31-33] As presented in Mani *et al.*[30] this ionic flux imbalance drives concentration polarization (CP). In Mani *et al.*[30], we found that, under conditions with high-Dukhin number and co-ion mobility, CP coupled with bulk flow can create propagating enrichment and depletion shocks. These shocks can have a long-range influence on a system which contains both nano- and microchannels. Systems combining nanochannels and channels with micron or larger characteristic length scales are being used for a variety of applications including increasing sample ion concentration,[24] analyzing DNA,[18] and detecting single molecules (and single ligand-binding pairs) with nanopores.[15] There have been a significant number of experimental studies of microchannel-nanochannel interfaces. Wang et al.[16] reported the use of CP to generate high focusing ratios of an ionic protein near a microchannel-nanochannel junction. CP has since been used for preconcentration with nanofluidic channels[16,24] and ion-permselective membranes.[20,22] Kim et al.[32] experimentally observed vortices at the interface between a microchannel and a nanochannel.

Studies of colloids and nanoporous membranes were among the earliest basic experimental investigations of CP. Rubinshtein et al.[44] reported the use of a gel to stabilize the liquid on the depletion side of a nanoporous membrane, suppressing the instability mechanism which causes overlimiting conductance. In a microchannel system, Pu et al.[31] performed imaging with Fluorescein and reported enrichment and depletion zones below a threshold concentration of 3 mM sodium borate with a 60 nm nanochannel. Dhopeshwarkar et al.[33] reported focused peaks of fluorescein moving away from the cathode side interface between a microchannel and a nanoporous hydrogel plug. Finally, Hlushkou et al.[56] performed experiments showing the effects of neutral or negatively charge hydrogel plugs on the enrichment of size excluded analytes.

The typical electrolyte system used in previous experiments consists of a buffer ion, its co-ion, and a third, observable, fluorescent ionic species initially present in low concentration relative to the two other "background" ions. To date, outside of our own work,[29] we are aware of no microchannel CP experiments which directly observed the concentration distribution of one of two dominant ions which make up an electrolyte.[16,20,31-33]

Additionally, previous experiments were typically performed at potentiostatic (constant voltage) conditions.[31-33,56] This makes comparisons to models difficult as current density (and not voltage) directly dictates local ion transport throughout the system. When CP shocks propagate, the microchannel-nanochannel system resistance is dominated by the large resistance of the depletion region. However, as has been observed in studies of nanoporous membranes,[43] conditions in the depletion region may be governed by reaction equilibria (e.g., dissociation of water[69]) which have not been considered in microchannel CP models to date. Furthermore, constant current conditions yield linear growth of the enrichment and depletion regions with time (c.f. Figure 2.4), which simplifies comparison to models. We note, however, that constant current and constant voltage demonstrate essentially the same effects, with a difference only in the rate at which CP propagates.

In Mani *et al.*[30] we presented and discussed two models which describe CP, including CP with propagation. Our area-averaged model was presented in terms of the Boltzmann equilibrium concentration, c_0. c_0 equals the centerline counter-ion concentration for a channel with negative surface charge and non-overlapped EDLs. In the case of overlapped EDLs, c_0 is a concentration associated with evaluating the Boltzmann distribution at zero potential relative to the potential in a hypothetical reservoir. As discussed in Mani *et al.*[30], the centerline concentration is equal to $c_0 \exp(-z_i e\psi|_{y=0}/kT)$, where $\psi|_{y=0}$ is the centerline potential, obtained by solving the Poisson-Boltzmann equation with boundary conditions imposed at the walls ($y = \pm h/2$). c_0 varies in x and is fixed at the inlet and outlet of the system to the value of ionic concentration at end-channel reservoirs where $\psi = 0$. We found that the coupling of CP and bulk flow is captured analytically by a system of PDEs for the evolution of c_0 as follows:

$$\frac{\partial}{\partial t}(hfc_0) + \frac{\partial}{\partial x}[h(\bar{u}^p f_2^p + u_0^e f_2^e + \nu_2 z_2 FEf)c_0] = \frac{\partial}{\partial x}[hD_2 f \frac{\partial c_0}{\partial x}], \tag{2.1}$$

$$\frac{\partial}{\partial t}\left(hfc_0 - \frac{2\sigma}{z_1 F}\right) + \frac{\partial}{\partial x}[h(\bar{u}^p f_1^p + u_0^e f_1^e + \nu_1 z_1 FEf)c_0 - 2\nu_1 E\sigma] = \frac{\partial}{\partial x}[hD_1 f \frac{\partial c_0}{\partial x} - \frac{2D_1}{z_1 F}\frac{\partial \sigma}{\partial x}] \tag{2.2}$$

where $u_0^e = \left(-\varepsilon\zeta E/\eta\right)$ is the Helmholtz-Smoluchowski velocity and $\bar{u}^p$, the area-averaged pressure driven flow velocity, is determined from the conservation of mass,

$$\frac{\partial}{\partial x}(h\bar{u}^p + hu_0^e f^e) = 0, \tag{2.3}$$

The functions f, f^e, f_1^p, f_2^p, f_1^e and f_2^e are defined in Mani *et al.*[30]. These functions describe the effect of finite EDLs; h is the local channel height; ν_1 and ν_2 are the mobilities of the positive and negative species; z_1 and z_2 are the valences of the positive and negative species. We use the anion diffusivity, D_2, to approximate diffusion effects; ζ is the zeta potential; σ is wall charge; ε is permittivity, F is Faraday's constant; η is viscosity. Eqs (2.1)-(2.3) can be discretized and solved numerically for c_0, E, $\bar{u}^p$, and u_0^e to generate predictions of CP and CP propagation for more general cases than we considered with the simple model in Mani *et al.*[30].

The second model presented in Mani *et al.*[30] (the simple model) showed that a nonzero slope of the channel height, $\partial h/\partial x \neq 0$, gives rise to CP regardless of channel height. This is consistent with Dukhin's work on polarization around a spherical particle.[42] Dukhin showed that net neutral concentration is transferred into or out of the bulk solution whenever current crosses into or out of an EDL. Within the EDL, more current is carried by counter-ions to the wall charge than co-ions. Local enrichment occurs due to an ionic flux imbalance when more counter-ions emerge from an EDL than are required to carry current in the bulk solution. In our system, enrichment occurs at the micro/nanochannel interface on the cathode side where $\partial h/\partial x > 0$ (Figure 2.1(a), region 4). Similarly, at the anode side interface (region 2) $\partial h/\partial x < 0$, counter ions enter the EDLs, and there is a local depletion of c_0. In Mani *et al.*[30] we found that while a polarization of net charge (CP) always occurs to some extent in a microchannel-nanochannel-microchannel system, propagation of accumulation and depletion regions is governed by two key nondimensional parameters. One is an inverse Dukhin number, $c_r^* h_n^* = (\nu_1 z_1 - \nu_2 z_2) F h_n c_r / (-2\nu_1 \sigma)$, which describes the ratio of bulk conductivity to EDL conductivity, and the other is the mobility of the co-ion divided by the electroosmotic mobility, $\nu_{2n}^* = \nu_2 z_2 F \eta / \zeta_n \varepsilon$. Low $c_r^* h_n^*$ values and high ν_{2n}^* values result in sufficiently strong depletion at the anode side interface to cause negative characteristic velocities in the depletion region. Under these conditions a CP depletion shock propagates into the anode side microchannel (region 1); simultaneously an enrichment shock propagates into the cathode side channel (region 5). High values of $c_r^* h_n^*$ and low values of ν_{2n}^* result in positive characteristic velocities in the depletion zone and no shock propagation is observed. Therefore, the sign of the characteristic velocity in the depletion region fully determines the existence of CP with propagation.

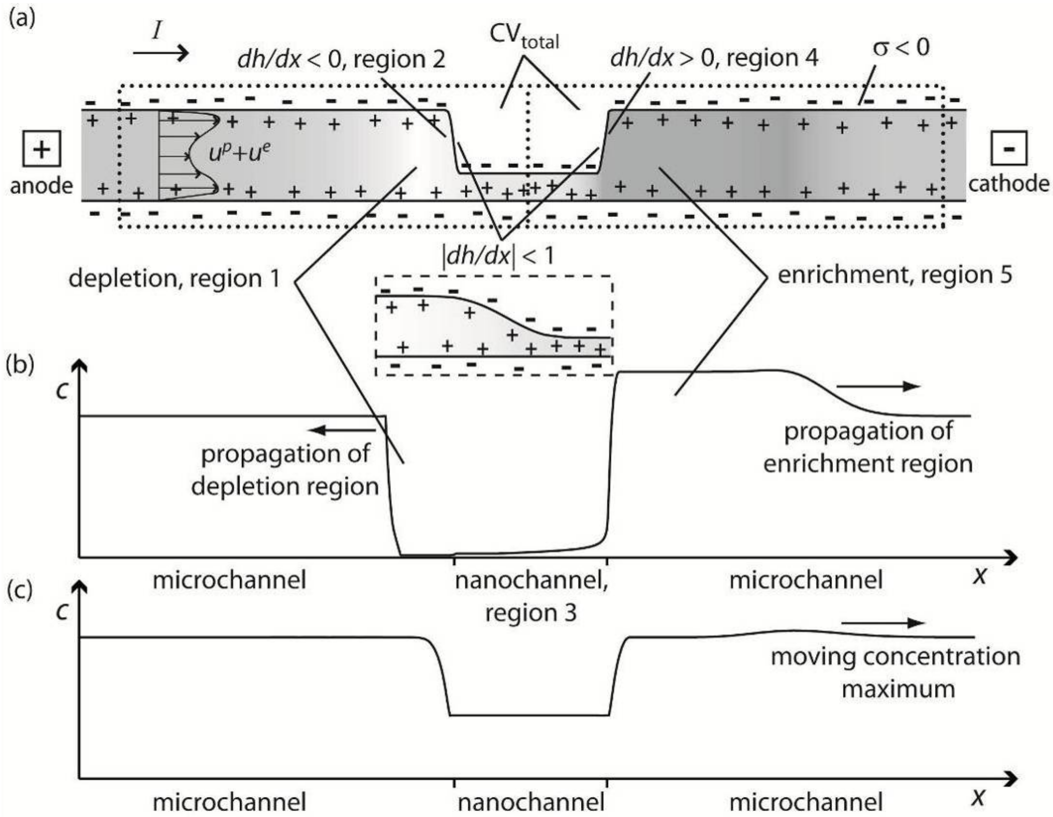
(a)
I
$dh/dx < 0$, region 2
CV_{total}
$dh/dx > 0$, region 4
$\sigma < 0$
u^p+u^e
anode
cathode
$|dh/dx| < 1$
depletion, region 1
enrichment, region 5
(b)
c
propagation of depletion region
propagation of enrichment region
microchannel
nanochannel, region 3
microchannel
x
(c)
c
moving concentration maximum
microchannel
nanochannel
microchannel
x

Figure 2.1 Schematic of microchannel-nanochannel-microchannel system. (a) The sign of the wall charge and the shallow micro-to-nano and nano-to-micro interfaces shown. Dotted lines depict control volumes (CV) used to derive the enrichment region concentration increase. Simulation results (concentration profiles) show cases where propagating CP occurs (b) and when there are negligible CP and no propagation of CP zones (c). In (b), the regions of strong depletion (anode side) and significant enrichment (cathode side) propagate as shockwaves up and downstream, respectively. The depletion shock is a strong shock is much stronger than the enrichment shock, therefore, the depletion shock appears much sharper. In (c), the final concentration in the microchannels is approximately equal to the initial value.

In this chapter, we present computations based on eqs (2.1)-(2.3) for a range of conditions which we also examined experimentally. The experiments and predictions presented here are in the high $Pe{\cdot}L/h$ regime where propagation of CP zones is readily detectable and where CP zone interface widths are small relative to the channel length. These results show that, because of CP with propagation, a nanochannel can have significant long-range (e.g., ~cm long) effects in a typical hybrid microchannel-nanochannel system. We show that computations based on eqs (2.1)-(2.3) using independent measurements of system parameters with no fitting parameters can be used to predict whether or not CP shocks will propagate. For the first time, we present experiments where the background electrolyte consists of only a fluorescent ion and its counter-ion. We use well-controlled experiments at constant current conditions, and quantify the spatio-temporal development of CP with propagation. These experiments confirm that the simple model of Mani *et al.*[30] provides useful scaling and intuition regarding propagating enrichment and depletion regions. In computations using nanochannel wall charge as the only fitting parameter, we show excellent agreement between predictions and experimentally measured enrichment and depletion shock velocities.

2.2 Numerical Study

This chapter considers devices fabricated with the simple microchannel–nanochannel-microchannel geometry depicted in Figure 2.1(a) and Figure 2.2. The numerical model solves species flux equations which are area-averaged (integrated over the channel height and assumed uniform across the channel width), resulting in one dimensional (along axial length), unsteady equations for species, electric flux, and ionic current. As discussed above, this area-averaged model includes the effects of EDLs in both the nano- and microchannels using the *f* factors given in Mani *et al.*[30].

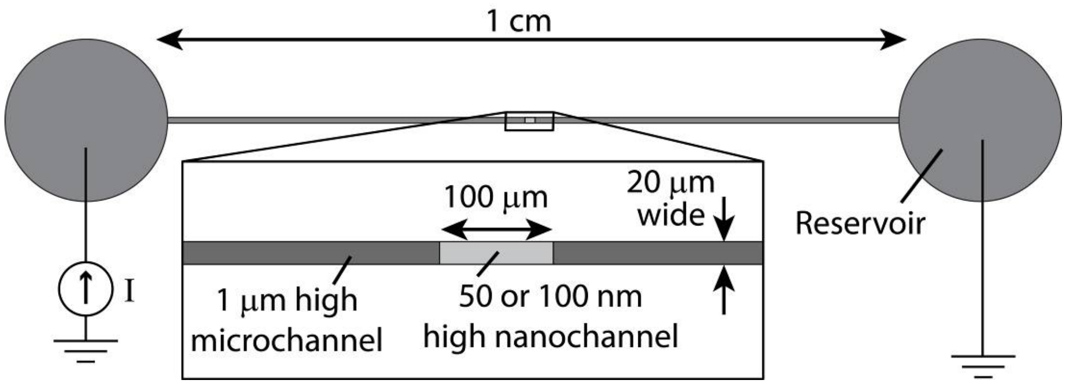

Figure 2.2 Schematic of experimental setup of microchannel-nanochannel-microchannel system. The device was fabricated using a two dry etch process on fused silica. We filled channels with a solution where lithium ions and fluorescent Alexa Fluor ions (in a small number of cases only sodium and Fluorescein ions) formed the primary electrolyte. We applied constant current using a high voltage (source-and-measure) power supply.

Here we will give the solution algorithm for eqs (2.1)-(2.3). As shown in Mani *et al.*[30], we can rewrite eq (2.3) as

$$\bar{u}^p = (Q - hf^e u_0^e)/h, \tag{2.4}$$

where $Q = \int_{x_1}^{x_2} \frac{f^e u_0^e}{h^2} dx \Big/ \int_{x_1}^{x_2} \frac{1}{h^3} dx$.is the volume flow rate per unit width. Substituting this expression for Q into eq (2.4) results in an explicit expression for $\bar{u}^p$ in term of u_0^e. Using this expression for $\bar{u}^p$ we subtract eq (2.1) from eq (2.2) to obtain an expression for conservation of current:

$$\begin{aligned} &\frac{\partial}{\partial t}\left(-\frac{2\sigma}{z_1 F}\right) + \frac{\partial}{\partial x}[h(\bar{u}^p(f_1^p - f_2^p) + u_0^e(f_1^e - f_2^e) + (\nu_1 z_1 - \nu_2 z_2)FEf)c_0 - 2\nu_1 E\sigma] \\ &\qquad = \frac{\partial}{\partial x}[h(D_1 - D_2) f \frac{\partial c_0}{\partial x} - \frac{2D_1}{z_1 F}\frac{\partial \sigma}{\partial x}]. \end{aligned} \tag{2.5}$$

The model allows us to study the effect of spatial and temporal variations of σ in eq (2.5) (e.g., with local ion densities). However, we here study mostly the case of fixed σ for simplicity. Also for simplicity, we neglect the diffusion term in eq (2.5), but keep the diffusion term in eq. (2.1) to approximately capture the effects of diffusion on concentration profiles.[30] Next, using the solution for $\bar{u}^p$ and u_0^e, we integrate eq (2.5) along the axial direction to obtain an integral equation for E:

$$\left\{\left[(\nu_1 z_1 - \nu_2 z_2)Ff - \frac{\varepsilon\zeta}{\eta}(f_1^e - f_2^e - f_1^p f^e + f_2^p f^e)\right]hc_0 - 2\nu_1\sigma\right\}E$$

$$-\frac{\varepsilon(f_1^p - f_2^p)c_0}{\eta\int_{x_1}^{x_2}\frac{dx}{h^3}}\int_{x_1}^{x_2}\frac{f^e\zeta E}{h^2}dx = \frac{I}{Fz_1}, \qquad (2.6)$$

where I is fixed for the constant current conditions considered here. To time advance the one dimensional partial differential eq (2.1), one can first obtain the previously discussed *f*-factors and ζ, which are known functions of c_0, and solve eq (2.6) to obtain $E(x)$. Then substituting $E(x)$ yields u_0^e, which can be used to obtain $\bar{u}^p$, providing all of the terms in eq (2.1).

For our computations we used a one dimensional grid for spatial discretization of eqs (2.1) and (2.6) with a grid spacing of 2 μm for the nanochannel and 20-100 μm for the microchannels. The height jumps at the channel interfaces were modeled as smooth gradients across a length of about 5 μm. The integral in eq (2.6) was discretized using a second order rectangle rule.[70] We used a Roe scheme[71] to discretize the nonlinear flux and employed a second order central difference[70] to approximate the diffusive flux in eq (2.1). For time integration, we used a first order implicit time advancement method[70] to enhance robustness of the numerical solution. We conducted a mesh and time step refinement study to ensure that the solutions are unbiased by discretization errors.

We computed the dynamics of CP as a function of the two major parameters discussed in Mani *et al.*[30]: $c_r^* h_n^*$ and ν_{2n}^* (c.f. Figure 2.5). To this end, we performed 732 full simulations of the microchannel-nanochannel system for conditions, covering the range of $c_r^* h_n^*$ and ν_{2n}^* considered experimentally. We chose all other parameters to match the experimental conditions: h_n = 50 nm, h_m = 1 μm, I = 1x10^{-4} A/m, t_{final} = 100s, z_1 = 1, z_2 = -2, L_{nano} = 100 μm, L_{total} = 10 mm, c_r = 2 mM, and ν_2/ν_1 = 0.35 (unless otherwise noted). The parameters $c_r^* h_n^*$ and ν_{2n}^* determined the wall charge, σ, and the mobility of the anionic species, ν_2, for each condition. For these computations, the wall charge was assumed to be constant and uniform throughout the channel system. We note that dynamics of wall charge are a complex and open problem in this field,[36,72] and that the assumptions we use here suffice to capture the major trends observed in experiments. In separate computations, for direct quantitative comparison to experiments (c.f. Figure 2.4) we used the nanochannel wall charge, σ_{nano}, as a single fitting parameter. We adjusted σ_{nano} until the depletion region shock velocity matched the experimental depletion shock velocity.[*]

2.3 Experimental Setup

In this section we describe the setup used to measure ion concentrations inside a microchannel-nanochannel system. Our system consists of a microchannel-nanochannel device (as in Figure 2.2) filled with water containing only a fluorescent ion and its counter-ion. We image the distribution of fluorescent dye in this system over time after current is applied using an epifluorescent microscope and a CCD camera. We use these measurements of dye distribution over time to quantify the enrichment and depletion shock velocities and the magnitude of the change in concentration inside the enrichment region.

2.3.1 Materials and Instrumentation.

We filtered deionized (DI) water prior to use with 0.2 μm pore syringe filters (Nalge Nunc International, Rochester, NY). We chose Alexa Fluor 488 (carboxylic acid succinimidyl ester, Molecular Probes, Eugene, OR) dye for insensitivity to pH and low rate of photobleaching.[73] Upon dissolution in deionized water, the electrolyte consists of the divalent Alexa Fluor anion and the lithium cation. In limited cases we also used sodium Fluorescein (J.T. Baker, Phillipsburg, NJ) at higher ionic strength (due to its strong solubility in water) to qualitatively determine if CP shocks propagate. Fluorescein fluorescence has a strong dependence on pH and is strongly susceptibility to photobleaching (relative to Alexa Fluor), precluding us from using Fluorescein as a quantitative measure of ion concentration. Note that these electrolyte systems are unbuffered, therefore, pH is determined by equilibrium with dissolved carbon dioxide and electrolysis at the electrodes. We measured $\mathrm{pH} \approx 5$ before the start of experiments which we attributed to the influence of carbon dioxide. To estimate the effect of pH during the experiment, we assume well mixed reservoirs, a maximum applied current of 4 nA, an experiment duration of 100 s and a typical well volume of 40 μL. This gives a maximum total concentration of order 1×10^{-7} M hydronium ions produced at the anode. This is negligible relative to the initial concentration of hydronium ($\sim 10^{-5}$ M) from atmospheric carbon dioxide, resulting in negligible change in pH.

---

[*] We also explored a version of the model where the surface charge was varied locally and in real time during the computation. This used an empirical fit for zeta potential as a function of local ion density (c.f. Figure 2.3) and the full Poisson-Boltzman equation to relate surface charge to zeta potential. We found this model performed worse than the fixed surface charge model (e.g., in predicting V_1, V_5 and c_5). We hypothesize that this is partly due to the fact that our CP and transport processes are fast (typically 100 s or less) relative to the timescale for equilibrium between the wall charge and bulk solution.[60].

We captured images using an upright, epifluorescent microscope (Olympus IX-70, Happauge, NY) with a dichroic filter cube with cut-offs at 493, 505 (dichroic), and 500 nm (Z488BP, Chroma Technology Corp., Rockingham, VT) and 10x, 0.4 NA (UPlanApo) or 20x, 0.5 NA (UPlanFl) objectives (Olympus, Happauge, NY). We recorded images using a 12-bit, intensified CCD camera (IPentaMAX, Roper Scientific, Trenton, NJ) using a 0.31x demagnifier (Diagnostic Instruments, Inc. Sterling Heights, MI) to increase field of view while preserving resolution. A manually adjustable pulse generator (BNC 555, Berkeley Nucleonics Corporation, San Rafael, CA) set the frame rate. We used a high-voltage source-and-measure power supply (Sourcemeter 2410, Keithley Instruments, Inc., Cleveland, OH) to control current density. The experimental setup is shown schematically in Figure 2.2.

2.3.2 Device Fabrication.

We fabricated microchannel-nanochannel devices in fused silica using conventional photolithography, dry etching, and bonding techniques.[13,74] Nanochannel sections were 49 and 97 nm high (corresponding to nominal heights of 50 and 100 nm) and all microchannel sections were 1 μm high. All sections were 20 μm wide (in plane). The region over which height changes between the nanochannel and the microchannels is ~2 μm long (determined by physics of our photolithography and etching). We characterized channel height using a Dektak profilometer (Veeco Instruments, Santa Barbara, CA).

2.3.3 Preliminary Quantifications of Electrophoretic and Electroosmotic Mobilities.

The mobility of the Alexa Fluor 488 dianion was determined experimentally given the known mobility of Li^+ and conductance measurements in a borosilicate microchannel. We quantified zeta potential, ζ, as a function of concentration for Alexa Fluor 488 and sodium Fluorescein concentrations in a set of preliminary calibration experiments. We used the current monitoring technique[75] in a 10 μm high, 70 μm wide borosilicate microchannel (Caliper Life Sciences, Mountain View, CA). Separate current monitoring experiments using 1 mM Alexa Fluor in a 1 μm high fused silica microchannel (negligible EDL) fabricated with the same technique and materials used for microchannel-nanochannel devices gave results within 8% of the measured ζ in borosilicate.

From the ζ measurements shown in Figure 2.3 we estimate wall ζ as a function of dye concentration according to a power law fit:

$$\zeta = -ac_r^b \tag{2.7}$$

A least squares fit provides excellent agreement to the data with a = 0.0553 V/mM^b and b = -0.261 for Alexa Fluor 488 as the electrolyte, and a = 0.0760 V/mM^b and b = -0.122 for Fluorescein. Calculations of shear plane charge (hereafter "wall charge") from Guoy-Chapman theory[76] based on measured ζ potentials showed a $\sim c_r^{-0.33}$

dependence for Alexa Fluor 488. To find a scaling for ζ inside the nanochannel, ζ_n, we used this calculated wall charge and the theoretical result that $c_n \sim 0$ for most experimental cases and found that, $\zeta_n \sim c_r^0$. These data are used later to analyze trends in measured shock velocities and enrichment region concentrations.

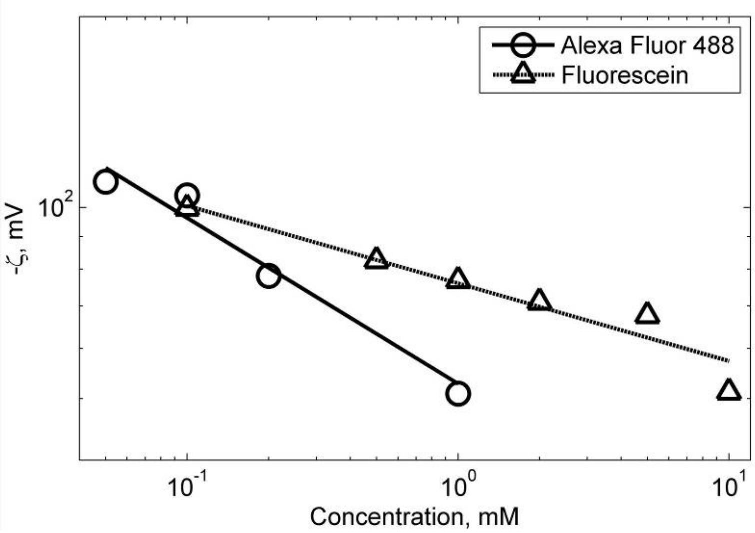

Figure 2.3 Zeta potential measurement results versus Alexa Fluor 488 and sodium-fluorescein concentration. A power law fit of the form $\zeta = -aC^b$ gave a = .0527 V/mM^b and b = -0.261 for Alexa Fluor 488 and a = 0.0760 V/mM^b and b = -0.122 for Fluorescein. Data are shown over the concentration range used in CP experiments.

2.3.4 CP and Imaging Protocol.

We filled our channels with dye solution via pressure driven flow (40 min at ~1 atm) before each experiment. For more information on channel conditioning, see Appendix A. Upon application of order 1 nA currents, voltage (which was automatically regulated by the high-voltage source-and-measure power supply) typically increased from zero to about 200 V over 2 min, and then increased steadily over the remainder of the experiment (~10 min). We recorded images at 0.5 to 10 fps depending on the applied current density. We corrected all images using flatfield and background images acquired before and after each experiment, respectively. We smoothed images with negligible loss in resolution[†] using a Gaussian filter with a standard deviation of 1.5 μm.

2.4 Results and Discussion

2.4.1 Scaling Derivation from Simple Model.

We here present some key scaling arguments of Mani *et al.*[30] which serve to frame the numerical results, yield intuition, and help explain observed experimental trends. In Mani *et al.*[30] we predicted that the enrichment shock velocity is equal to the bulk velocity in the microchannel. Therefore, assuming the nanochannel is the dominant pressure resistance (a good assumption for our geometry) the enrichment shock velocity is

$$V_5 = \frac{Q}{h_m} \approx \frac{U_n^{EOF} h_n}{h_m}, \tag{2.8}$$

where Q is the bulk flow rate, U_n^{EOF} is the area-averaged electroosmotic flow (EOF) velocity in the nanochannel, and h_m and h_n are the microchannel and nanochannel heights, respectively. Therefore, in terms of the experimental parameters

$$V_5 \approx \left(\frac{\varepsilon}{h_m \eta}\right)\frac{\zeta_n h_n I}{G_n}, \tag{2.9}$$

where G_n is the nanochannel conductance, ε is permittivity, ζ_n is nanochannel zeta potential, η is viscosity, and I is the applied current. For small $c_n^* h_n^* = (\nu_1 z_1 - \nu_2 z_2) F h_n c_n / (-2\nu_1 \sigma)$, nanochannel conductance is approximately independent of the channel height and proportional to σ,[37] and $V_5 \sim \zeta_n h_n I/\sigma$. Note that initial nanochannel wall charge is taken as a function of c_r. We use these scalings to examine trends in our measurements of enrichment shock velocity.

[†] The standard deviation of the Gaussian filter was chosen to be less than the point-response function of the microscope objective used in this study. The Rayleigh criterion for the 20x, 0.5 NA objective is 13 m, for the 10x, 0.4 objective the Rayleigh criterion is 8 μm.

Similarly, we can derive an equation relating the depletion shock velocity to the applied current. Based on eqs 41-44 of Mani *et al.*[30] and the scaling for bulk velocity given by eq (2.8)

$$V_1 = V_5 - \left(\frac{\varepsilon}{h_m \eta}\right)\frac{\zeta_n h_n I}{G_n}\cdot\frac{c_5^* h_n^*}{c_r^* h_n^*}. \tag{2.10}$$

where, from eqs 43 and 45, $c_5^* h_n^* = \nu_{2n}^*$ for $\nu_{2n}^* < 1$ and $c_5^* h_n^* = \left(2\nu_{2n}^* - 1\right)$ for $\nu_{2n}^* \geq 1$. Assuming $G_n \sim \sigma$, $\left(V_1 - V_5\right) \sim \zeta_n h_n I / \sigma \cdot c_5^* h_n^* / c_r^* h_n^*$. Physically, there are two contributions to V_1: One due to bulk flow, which is equal to V_5, and one which is driven by current through the EDLs. Therefore, the quantity $\left(V_1 - V_5\right)$ is the portion of the depletion region shock velocity which is driven by current through the EDLs. We will show that measured $\left(V_1 - V_5\right)$ is proportional to applied current and scales as predicted by eq (2.10).

Next, we derive a scaling for the measured cathode side enrichment ratio, c_5/c_r ,which sets the electric field in the cathode side microchannel. Based on eqs 41 and 43 of Mani *et al.*[30]

$$\frac{c_5}{c_r} = \frac{c_5^* h_n^*}{c_r^* h_n^*}. \tag{2.11}$$

where, again, $c_5^* h_n^* = \nu_{2n}^*$ for $\nu_{2n}^* < 1$ and $c_5^* h_n^* = \left(2\nu_{2n}^* - 1\right)$ for $\nu_{2n}^* \geq 1$. Hence, the enrichment region concentration ratio is independent of applied current. Later we will show experimental evidence which demonstrates this somewhat non-intuitive result.

Finally, using the analytical results of Mani *et al.*[30], we can derive a simple relation among all of the experimentally measurable parameters, c_5, c_r, V_1, and V_5. Substituting Mani *et al.*[30], eq 41 into eq 42, or Mani *et al.*[30] eq 43 into eq 44, yields

$$\frac{c_5}{c_r} = 1 - \frac{V_1}{V_5}. \tag{2.12}$$

This expression is a general result which can be derived from a much simpler control volume analysis and the observation that $c_1 \sim 0$. Conserving species, current, and bulk velocities in the large control volume, CV_{total}, of Figure 2.1(a), we see the net accumulation, Σ_{total}, is zero. Dividing this region into two respective CVs for the anode and cathode sides, we write $\Sigma_{anode} + \Sigma_{cathode} = 0$; so the rate of concentration depletion on the anode side is proportional to $(c_r - c_1)V_1 \approx c_r V_1$. This is equal to the rate at which the concentration increases on the cathode side

$$c_r V_1 = (c_r - c_5)V_5. \tag{2.13}$$

Eqs (2.12) and (2.13) are equivalent, and eq 8 is derivable from a CV analysis which yields intuition about system-wide reorganization of charge. CP redistributes ionic strength from the anode side of the nanochannel (forming depletion) to the cathode side (creating enrichment).

2.4.2 Numerical Results.

Figure 2.1(b) and Figure 2.1(c) show two illustrative anecdotal results of the computations. Figure 2.1(b) shows a representative computation for a propagating CP case with $c_r^* h_n^*$ = 0.71 and ν_{2n}^* = 0.7. Under these conditions, CP formed an anode-side depletion region with $c_1 \approx 0$ and a cathode side enrichment region with $c_5 > c_r$. At these values of $c_r^* h_n^*$ and ν_{2n}^*, we see the CP depletion and enrichment regions at the anode and cathode-side nanochannel interfaces. However, unlike classic, stationary models, the computational model captures transient propagation of CP depletion and enrichment regions toward the anode and cathode, respectively (c.f. Figure 2.4(a) and (b)).

Figure 2.1(c) shows a representative computation for $c_r^* h_n^*$ = 0.85 and ν_{2n}^* = 0.37. In this regime of the $c_r^* h_n^*$ and ν_{2n}^* map, the depletion region characteristic velocity is positive and so CP enrichment and depletion shocks do not propagate (c.f. Figure 2.5). Here, the steady state concentrations in both the anode and cathode side microchannels are approximately equal to the initial concentration. The region just downstream of the nanochannel shows a slight enrichment versus that just upstream (as discussed in Mani *et al.*[30]). As predicted by the analytical results presented in Mani *et al.*[30], the nanochannel concentration quickly decreases (to 55% of its initial value) within a few hundred milliseconds. As the nanochannel concentration adjusts to its steady state value, the cathode side interface collects ionic strength and causes a slight increase in c_0 which moves at the bulk velocity through the cathode-side microchannel. (In the CP propagation case of Figure 2.1(b), the adjustment of the concentration in the nanochannel also causes a slight local maxima in concentration near the leading edge of the enrichment shock.)

Figure 2.4(a), (b), and (c) show predicted spatiotemporal plots of the ion concentration in the series micro-nano-microchannel system as a function of the axial coordinate and time. The parameters are identical to those of the experiments (discussed below). White/yellow color indicates high concentration (enrichment) and black represents low concentration (depletion). Figure 2.4(a) shows predictions for a constant current of 200 pA and a 50 nm high nanochannel. We used the known mobility of Li^+ ion and the measured mobility of the Alexa Fluor 488 dianion (as determined from independent experiments). We assumed the microchannel wall charge was constant and uniform and determined this using the measured zeta potential at the initial concentration of 1 mM. We found excellent agreement with experimental results for $\sigma_{nano} = 0.25 \ \sigma_{micro}$ (and this empirical value of 0.25 constitutes our only fitting parameter). The enrichment and depletion shocks spread as straight lines on this plot, indicating a constant shock velocity. Figure 2.4(b) shows computations for the same conditions and geometry as in Figure 2.4(a), but with a constant current of 800 pA. As predicted by the analytical model of Mani *et al.*[30] and the current numerical model, the enrichment and depletion shock velocities are directly proportional to current density. Note also the diffuse leading edge of the enrichment region for the 800 pA case, and the increased width of this transition in the 200 pA case.

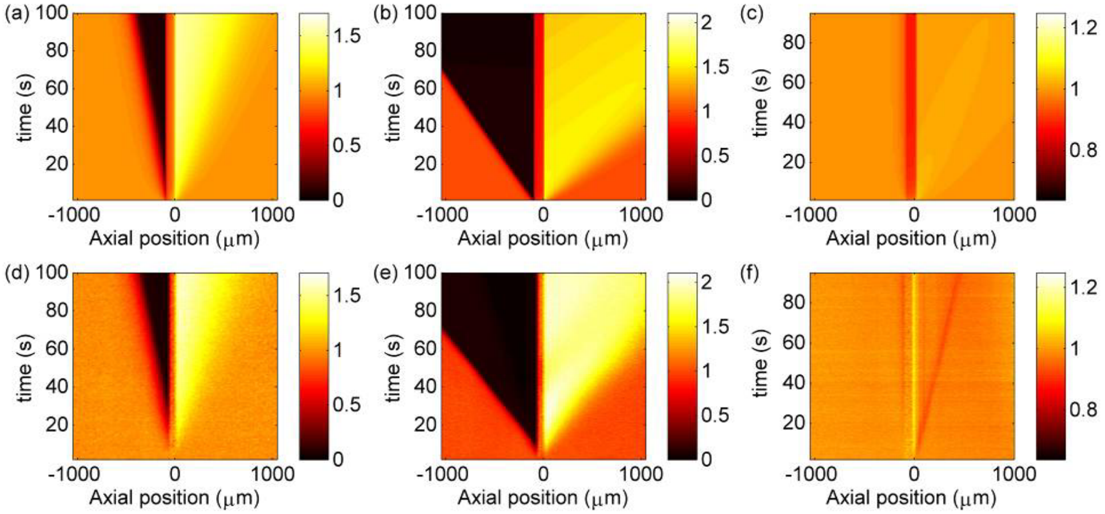

Figure 2.4 Representative simulations and experimental visualizations of ion transport and accumulation in our micro-nano-micro-channel system with 1 μm high microchannels. We show predicted spatiotemporal diagrams (ion concentration vs. time and axial position) for (a) , I = 200 pA and (b) I = 800 pA. Both (a) and (b) are for 1 mM Alexa Fluor 488, 50 nm high nanochannel, and $\sigma_{nano} = 0.25\ \sigma_{micro}$. Also shown are results for (c) I = 800 pA, 10 mM Fluorescein, 100 nm high nanochannel, and $\sigma_{nano} = \sigma_{micro}$ (no fitting parameter in this thin-EDL case). In the second row, we show experimental results for (d) I = 200 pA and (e) I = 800 pA. Both (d) and (e) used 1 mM Alexa Fluor 488 and 50 nm high nanochannel. Also shown are results for (f) I = 800 pA, 10 mM Fluorescein, and 100 nm high nanochannel. For the conditions of experiments (d) and (e), the model captures the essential observed features of propagating depletion (left side) and enrichment (right side) zones, and the proportionality of shock velocities with applied current. The model (in (c)) successfully predicts a slight disturbance and steady state microchannel concentrations approximately equal to the initial values observed in experiment (f). The colormaps used for (a) through (f) are shown to the left of each spatiotemporal plot.

Figure 2.4(c) shows a spatiotemporal plot for a sample case where CP enrichment and depletion shocks do not propagate (and CP is slight and confined to near-interface regions). This case corresponds to 10 mM sodium Fluorescein and a 100 nm high nanochannel. Here, we did not use a fitting parameter; we fixed both the microchannel and nanochannel wall charge based on independently measured ζ . As shown in Figure 2.1(c), a small "bump" region of increased concentration advects away from the nanochannel into the cathode side microchannel (note the slight contour ridge at about 30 degrees from the vertical on the cathode side). Other than this slight transient, the rest of the microchannel sections remained at the initial concentration. The nanochannel adjusted to a new concentration 12% lower than the initial value.

Figure 2.5 shows contours of c_5/c_r at steady state computed with our area-averaged (one-dimensional) computational model. (The simple model of Mani *et al.*[30] well predicts trends in c_5/c_r , but the computational model better accounts for the effects of EDL.) Here, c_5 is measured ~10 μm away from the cathode side interface. These results show that c_5/c_r decreases smoothly as $c_r^* h_n^*$ increases and ν_{2n}^* decreases. We also show a contour of U_1/V_5 = 0, where U_1 is the characteristic velocity in the depletion region ~10 μm away from the anode side interface. This provides a practical definition of the boundary between the regions where CP shocks propagate and where they do not ("no propagation"). The strong depletion shocks characteristic of CP with propagation can only occur when U_1 is negative. Figure 2.5 also shows the predicted phase boundary based on the simple model of Mani *et al.*[30] as a grey dashed line.

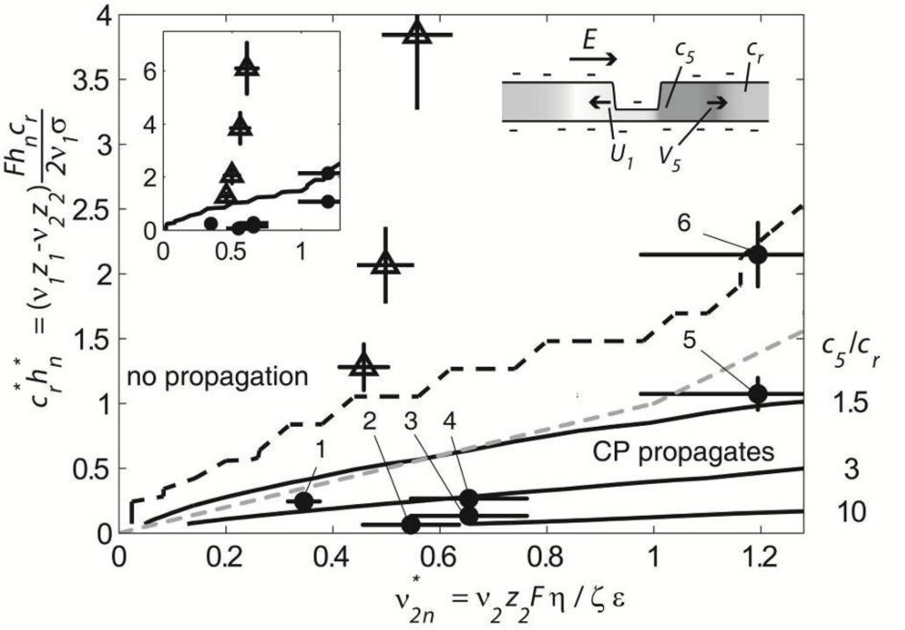

Figure 2.5 Phase diagram showing CP magnitude, c_5/c_r, from computations versus $c_r^* h_n^*$ and ν_{2n}^* and experimental observations covering the major parametric regimes. Contours reflect magnitude of computed c_5/c_r from 732 simulated conditions. The black dashed line is an approximate contour of $U_1/V_5 = 0$, a practical cutoff defining boundary between conditions with and without propagating shocks. U_1/V_5 is the ratio of the characteristic velocity in the depletion region to the enrichment shock velocity. The gray dashed line is the phase boundary between conditions with and without propagation predicted from simple theory of Mani *et al.*[30]. Filled circles and open triangles respectively denote observations with and without CP propagation. The numbers next to the filled circles indicate the concentration enrichment measurements shown in Table 2.1. Vertical and horizontal error bars represent the propagation of uncertainties in measured ζ (based on reservoir concentration) and ion mobility on $c_r^* h_n^*$ and ν_{2n}^* with 95% confidence intervals. (Only one observation of $c_5/c_r = 4.7$ was made for the Fluorescein case at $c_r^* h_n^* = 0.25$, $\nu_{2n}^* = 0.35$.) Top left insert shows an enlarged view of the $c_r^* h_n^*$ and ν_{2n}^* domain containing one additional experiment. Schematic at the top right shows measurement locations of concentrations and velocities.

Table 2.1 Summary of Experimental Conditions and Measured Values Presented in Figure 2.5

condition number	electrolyte	c_r (mM)	h_n (nm)	measured concentration enrichment[*]	number of realizations
1	Fluorescein	0.1	100	4.7	1
2	Alexa Fluor	0.05	50	7.36 +/- 0.41	18
3	Alexa Fluor	0.1	50	4.81 +/- 0.45	19
4	Alexa Fluor	0.1	100	2 +/- 0.16	18
5	Alexa Fluor	1	50	1.35 +/- 0.11	18
6	Alexa Fluor	1	100	1.5 +/- 0.18	2

[*] stated range is uncertainty on the mean value with 95% confidence

2.4.3 Experimental Results.

We performed a fairly extensive experimental parametric variation of key parameters. This includes over 100 realizations at 30 conditions. Experiments were performed at nanochannel heights of 50 and 100 nm and seven applied currents ranging from 50 pA to 16 nA. We used nine electrolyte solutions ranging from 100 μM to 10 mM sodium Fluorecein and 50 μM to 1 mM Alexa Fluor 488. Experimental conditions were chosen to span the range of available conditions at roughly logarithmic intervals where possible. A 50 nm channel was approximately the smallest channel which had reliably been make using our fabrication process. A 100 nm channel was the deepest channel we could use to keep the microchannel to nanochannel height ratio >> 1 (the microchannel height was set to a maximum of 1 μm for the dry-etch and photo-resist process we used). 50 pA was the lowest current setting on the electronic source-and-measure power supply where we were able to get stable current output. At currents higher than 16 nA we often saw unstable propagation of enrichment and depletion fronts (see Appendix B). Finally, 50 μm was the lowest Alexa Fluor concentration at which the electrolyte concentration was much greater than the estimated 10 μm concentration of OH- ions. 1 mM was less than one half the estimated Alexa Fluor solubility limit (~2.5 mM based on attempts to dissolve Alexa Fluor in DI water) which allows for an increase in concentration inside the enrichment region. Fluorescein has a higher solubility limit, therefore, these experiments were run at up to 10 mM initial concentration. Here we present a summary of these experiments and comparisons with our numerical predictions. We also compare trends to those predicted by the analytical model of Mani *et al.*[30].

Figure 2.4(d) and (e) show measured spatiotemporal plots for a channel initially filled with a uniform concentration of Alexa Fluor 488 dye and constant applied currents at the conditions of Figure 2.4(a) and (b), respectively. First, we see that the enrichment and depletion concentration shock motions and widths were consistent with the high $Pe \cdot L/h$ regime predicted and discussed in Mani *et al.*[30] (the $Pe \cdot L/h$ values for these cases are 54.4 and 165, respectively). The flow was clearly in a regime where propagations of enrichment and depletion zones are clearly observable and shock widths are much shorter than channel lengths. The enrichment and depletion shocks were linear, confirming the computational prediction that the shock velocities are constant in time. The shock velocities are also proportional to current density, as predicted by eqs (2.9) and (2.10) (confirmed in Figure 2.6). The shock widths of the 800 pA case are also smaller than those of the 200 pA case as predicted. (Note also that there is significant enrichment/depletion and CP propagates, yet the EDLs do not overlap for these cases with λ_D = 6.4 nm and h = 50 nm.)

Figure 2.4(f) shows sample experimental results for a reservoir concentration of 10 mM fluorescein (same as Figure 2.4(c)). For these conditions, the flow field is also in the high $Pe \cdot L/h$ limit (here $Pe \cdot L/h$ = 49), but in the regime where CP occurs but does not propagate, as predicted (e.g., see Figure 2.1(c)). Note also that a small disturbance in concentration advected away from the nanochannel at constant positive velocity. This disturbance is predicted by the computational model and, as discussed above, is caused by the readjustment of the nanochannel concentration to its steady-state value. The typical disturbance observed in experiments was sharper (narrower in space) than that predicted by the model as shown here. The experiment of Figure 2.4(f) also showed ~20 μm wide stationary, non-propagating regions of depletion and enrichment adjacent to the interfaces to/from the nanochannel. A diffusive depletion region is observed in the computations, although the predicted width of this region is ~100 μm; the local enrichment is barely apparent in computations.

We note that direct comparison of our experimental results to previous experimental visualizations of CP is very difficult, and could be misleading. One difficulty is that previous work has studied more complex geometries; such as intersections between multiple nanochannels and microchannels[16,20,31-32] or the CP type effects around randomly packed spheres,[77-78] membranes,[56] or ion perm-selective polymers.[22,33] Most importantly, comparison is made very difficult because we know of no other work which uses a fluorescent ion as one of two background electrolyte ions present in highest concentration, as we do here. Instead, all previous work in visualizaing CP[16,20,31-33,56,77-78] used an ionic, fluorescent species in low concentration relative to the background electrolyte. Such species may focus either because of CP or because of effects such as electrophoretic focusing of a single species in the background electric field gradients set up by CP of background electrolytes. In the latter case, fluorescent species accumulate and concentrate in regions where electrophoretic velocity is balanced by bulk velocity. We have published a preliminary analyses of the latter effect;[29] and will address this in more detail in a manuscript we are currently developing.

We performed experiments at conditions spanning ten combinations of $c_r^* h_n^*$ and ν_{2n}^*. A comparison between the predicted propagation vs. no propagation regime map and the experimental observations is shown in Figure 2.5. Experiments where CP shocks clearly propagated are shown as filled circles, while experiments where CP did not propagate are shown as open triangles. The $c_r^* h_n^*$ and ν_{2n}^* regime alone is an excellent predictor of whether CP shocks will propagate. All of the experimentally observed CP propagation cases fall within the predicted CP with propagation region. Similarly, ”no propagation” cases fall in the correct region. We note the open triangle nearest the U_1/V_5 = 0 boundary (at ν_{2n}^* = 0.45 and $c_r^* h_n^*$ = 1.3) showed a hybrid behavior.

For this case alone, the results show an initial (weak) development of CP with propagation followed by a decrease in cathode-side concentration and a reversal of shock velocities.

In Figure 2.5 we label the enrichment concentration ratio c_5/c_r for the experimental data where ion enrichment intensity was sufficiently above the noise for us to measure (these values can be compared to the c_5/c_r contours of the plot). The comparison shows that the theory is only a fair-to-good predictor of the absolute value of the enrichment ratio; differences between the predicted and observed absolute values of c_5/c_r from Alexa Fluor 488 experiments range from $\pm 20\%$. We hypothesize the discrepancy is related to the difficulties associated with accurate predictions of the nanochannel wall charge. As seen in Figure 2.4, we can well predict c_5/c_r if we use nanochannel wall charge as a fitting parameter.

Next, we present trends in measured depletion and enrichment shock velocities. To quantify shock velocities from measured spatiotemporal plots of fluorescence intensity (see Figure 2.4(d) and (e)), we thresholded the data (at approximately 10% and 50% of max intensity) to create binary images. We then used a simple edge-detection algorithm to identify 100-200 points along the shock boundaries and used a linear regression to measure velocity. We note, for many cases, enrichment and depletion shocks showed noticeable curvature over the first ~10 s. This behavior was also observed in computations and appears to be associated with initial transients in the nanochannel. In these cases, the reported shock velocity is measured after this initial transient. Other non-constant shock velocity behaviors are discussed in Appendix B.

Figure 2.6 shows scaled enrichment and depletion shock velocity measurements versus applied current. The shock velocities are scaled according to eqs (2.9) and (2.10) using the empirical relation for wall charge based on independent ζ measurements as well as v_{2n}^* and $c_r^* h_n^*$ computed as in Figure 2.5. The shock velocities, which varied from 0.7 to 282 μm/sec, varied proportionally with current density and were collapsed by the scaling. These magnitudes (and the strong concentration changes they propagate) are striking evidence to the importance of these shocks in determining the behavior and performance of hybrid micro- and nanochannel systems.

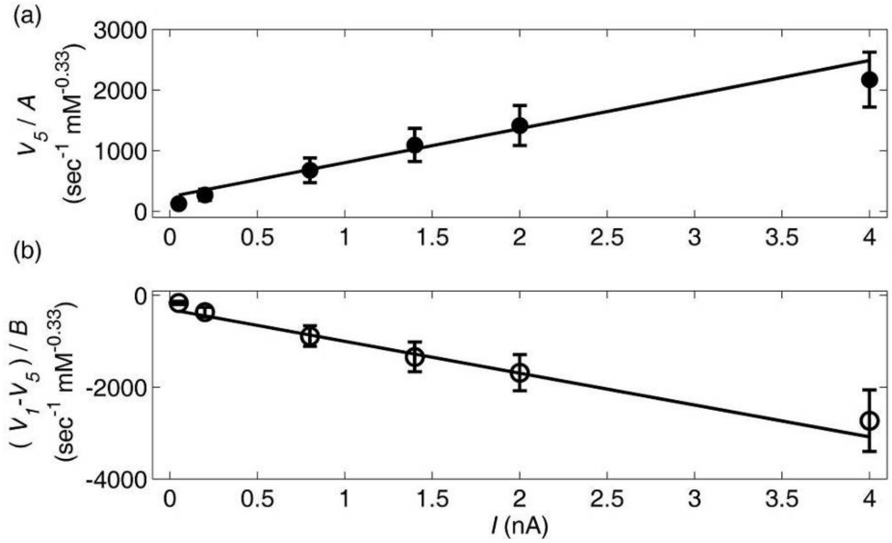

Figure 2.6 Measurements of enrichment (a) and depletion (b) shock velocities versus applied current for Alexa Fluor 488 experiments. In (a) we plot the enrichment shock velocity, scaled by *A*, where $A = h_n c_r^{0.33}$, and (b) presents the depletion shock minus enrichment shock velocity, scaled by *B*, where $B = h_n c_r^{0.33} \left(c_5^* h_n^* / c_r^* h_n^* \right)$. Data represent experiments with h_n = 50 nm and 50 μM, 100 μM and 1 mM dye concentrations as well as h_n = 100 nm and 100 μM dye concentration. We assumed σ varies with concentration according to a power law based on ζ potential measurements (this accounts for the fractional power in the scaling). v_{2n}^* and $c_r^* h_n^*$ were computed as in Figure 2.5. A solid black line shows a linear regression fit to all of the data. Error bars show 95% confidence intervals on the mean with $N \geq 12$. Shock velocities were computed by performing a linear least squares fit to the edge of the enrichment or depletion region on 73 spatiotemporal plots of concentration versus time (as shown in Figure 2.4). Shock velocities are clearly linearly proportional to current density as predicted by the model.

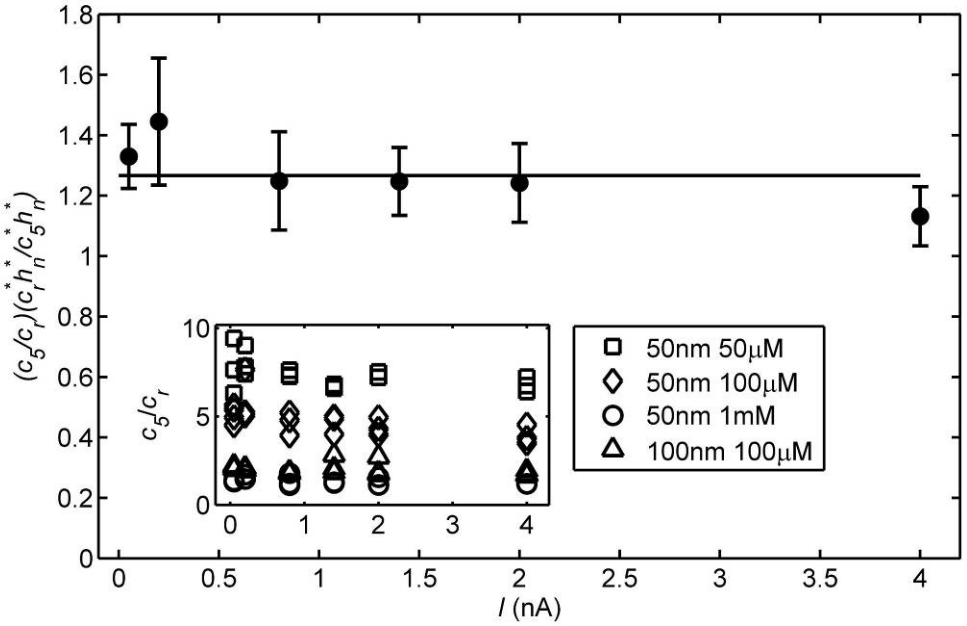

Figure 2.7 Scaled enrichment region concentration, $c_5/c_r\left(c_r^*h_n^*\right)/\left(c_5^*h_n^*\right)$,versus applied current. The line shows the average of all data as a visual reference. We computed v_{2n}^* and $c_r^*h_n^*$ for prediction of $c_5^*h_n^*/c_r^*h_n^*$ according to Mani *et al.*[30] eqs 41 and 43 and using the same parameter values as in Figure 2.5. Error bars show a 95% confidence interval on the mean at each value with $N \geq 12$. The insert shows raw, unscaled data for enrichment-to-initial ion density. As predicted, the scaled concentration data are approximately constant versus current.

Figure 2.7 shows the measured c_5/c_r divided by the predicted concentration factor, $c_5^*h_n^*/c_r^*h_n^*$ versus applied current.[‡] The scaled enrichment region concentration factor showed approximately no dependence on current density, as predicted by theory, confirming that (perhaps counter-intuitively) the magnitude of CP enrichment is not affected by current density. The mean value of the measured enrichment concentration factor divided by the predicted value is 1.3, demonstrating that the simple theory of Mani *et al.*[30] can be used as a fair predictor of c_5/c_r without fitting parameters or transient simulations. Raw data for c_5/c_r (insert) shows the significant scatter in the unscaled data (on average, c_5/c_r varies by a factor of ~7, while our scaled parameter varies by ~1.7).

[‡] To quantify the enrichment region concentration we averaged fluorescence intensities in a 200 pixel box after any initial, transient concentration increases. We assume the flatfield-corrected dye intensity is proportional to concentration. Quantitative measures of the depletion region concentration were not possible as most measured intensities were within the noise level. This result is consistent with the analytical prediction that the depletion region concentration is much less than the initial concentration.

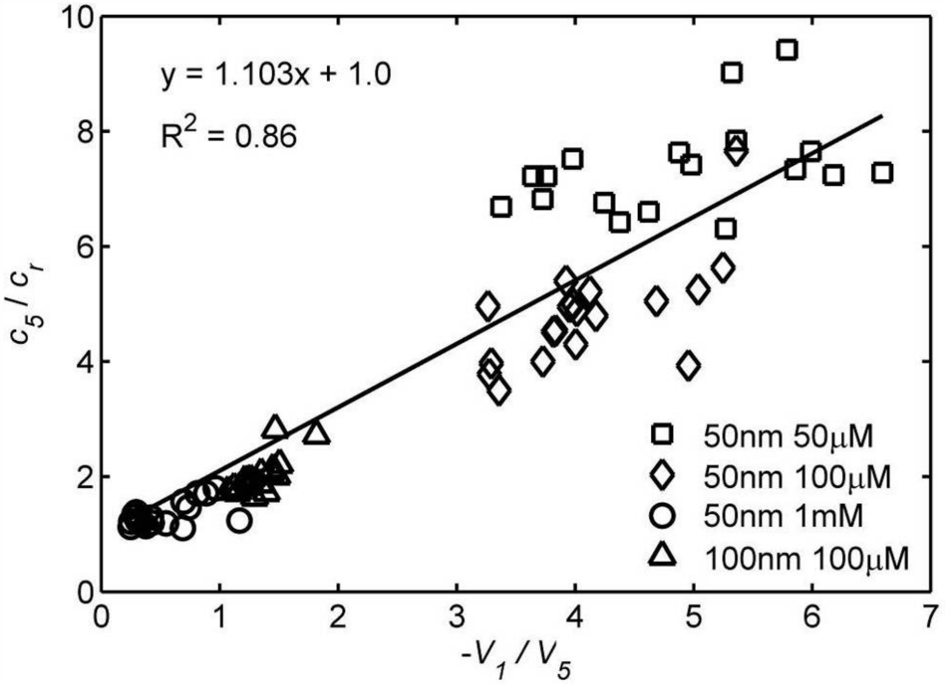

Figure 2.8 Background electrolyte enrichment factor, c_5/c_r, versus depletion-to-enrichment shock velocity ratio for 73 realizations. The solid line is a least squares best fit line with a fixed y-intercept of 1.0. The model predicts a linear dependence and we see it collapses the data very well for values of $-V_1/V_5$ below about 2, and adequately for larger values. This greater scatter may be due to the influence of impurity ions (e.g., carbonate) which were not controlled for in experiments.

Last, we present a collapse of all of the measured concentration and shock velocity data for the 73 relevant (CP with propagation) Alexa Fluor 488 experiments. Figure 2.8 shows the enrichment factor, c_5/c_r, versus the depletion-to-enrichment shock velocity ratio. All experiments approximately collapsed to one line, as predicted by eq (2.12). Figure 2.8 shows a regression fit with y-intercept fixed to 1.0 (consistent with experimental observations for cases where CP shocks did not propagate). In these experiments, V_1 was 0.0 μm/sec, and c_5/c_r was 1.0 (see Figure 2.4(f)). The fit line has a slope of 1.1; in good agreement with the predicted value of 1.0.

2.5 Section Conclusions

We have developed a computational model which accurately predicts the existence of CP with propagating enrichment and depletion shocks in a microchannel-nanochannel system based on separately determined zeta potential and ion mobilities. We presented the first experimental observations of CP in which the concentration field of the background electrolyte is directly observed and quantified. Experiments performed at constant current conditions showed constant growth of enrichment and depletion regions with time, validating our computational model and clearly demonstrating the predicted behavior of CP with propagation. The measured enrichment and depletion shock velocities scaled as predicted by Mani *et al.*[30]. In particular, the shock velocities increased linearly with current density, suggesting that, in a microchannel system, the extent of CP is determined by the current through the nanochannel. The magnitude of the CP enrichment relative to the reservoir concentration, c_5/c_r, also scaled as predicted by Mani *et al.*[30] and was essentially independent of current density.

For individual experimental conditions, we found excellent agreement to computational results using nanochannel wall charge as a single fitting parameter. This agreement includes the generation of depletion and enrichment zones on the anode and cathode sides of the nanochannel; the propagation of these zones upstream and downstream of the nanochannel; and trends in the ion concentration shock widths with current density. Overall, the results suggest that CP and its propagation can have long-range effects on the concentration in hybrid microchannel-nanochannel systems. These effects must be considered in the design of hybrid devices which attempt to leverage nanochannel physics.

3 Effects of Constant Voltage on Time Evolution of Propagating Concentration Polarization

The contents of this chapter have been submitted for publication in *Nano Letters* (Zangle, T. A., Mani, A., and Santiago, J. G., "Effects of constant voltage on time evolution of propagating concentration polarization," 2009).

In this chapter, we consider the time evolution of concentration polarization in one-dimensional microchannel-nanochannel systems (as in Figure 3.1). We investigate this system under two voltage conditions: one case in which the voltage across the system is set to a constant value, and another case in which current is maintained constant. We first present analysis based on the model of Mani *et al.*[30] and Zangle *et al.*[21] showing that for large times, the enrichment and depletion regions in a constant-voltage experiment grow proportional to the square root of time. We validate this prediction and compare to the constant current case using computational and experimental results. Finally, we use analytical and computational results to show that at long times, the growth rate of the enrichment shock thickness can match or exceed the growth rate of the enrichment region, leading to a diffusion-dominated steady-state profile.

3.1 Introduction

Recent work has shown that microfluidic-nanofluidic interfaces can be used to create preconcentration devices[16,20,24,79] or mixers,[59] and that microfluidic-nanofluidic interfaces can have profound effects on sample transport throughout microchannel-nanochannel systems.[28,33,56,80] In particular, concentration polarization (CP) can create a redistribution of ionic strength which has a significant influence on analyte concentrations and electric fields in these devices.[21,27,30-31]

In a series of papers,[21,30,80] we showed that under certain conditions, CP enrichment and depletion regions can spread as shocks. For constant-current conditions this leads to linear (in time) growth of enrichment and depletion zones at a rate proportional to the applied current. Experimentally, we confirmed that CP propagation is driven by a long-range mechanism controlled by electromigration and not merely a diffusion phenomena. These studies and experiments were performed for constant current conditions which more clearly and simply emphasize CP shock propagation physics.

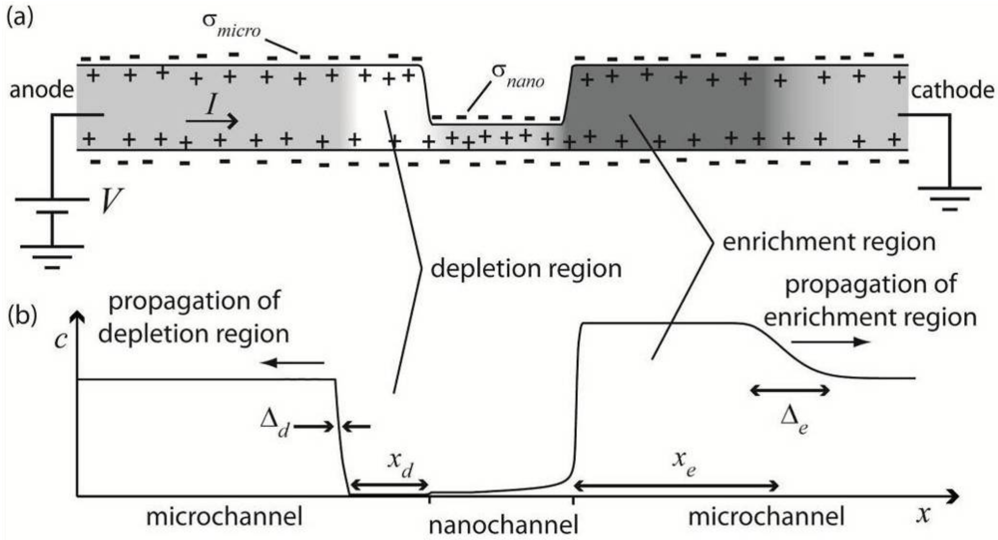
(a)
σ_{micro}
σ_{nano}
anode
cathode
I
V
depletion region
enrichment region
(b)
c
propagation of depletion region
propagation of enrichment region
Δ_d
Δ_e
x_d
x_e
microchannel
nanochannel
microchannel
x

Figure 3.1 Schematic of microchannel-nanochannel system. (a) shows the system with an applied voltage, V, current of I, microchannel surface charge density of σ_{micro} and nanochannel surface charge density of σ_{nano}. (b) shows the axial concentration distribution (matching the grayscale shading in (a)), c,[*] width of the enrichment and depletion regions, x_e and x_d, and enrichment and depletion shock thicknesses, Δ_e and Δ_d.

In this chapter, we consider the time evolution of CP in one-dimensional microchannel-nanochannel systems (as in Figure 3.1). We investigate this system under two applied power conditions: one case in which current is maintained constant and another (more common) case in which the voltage across the system is constant. We first present analysis based on the model of Mani *et al.*[30] and Zangle

---

[*] c represents the concentration of the counter-ion to the wall charge outside of the electrical double layer (EDL) for non-overlapped EDLs. For overlapped EDLs, c is the leading term of the Boltzmann distribution describing the concentration of ions through the EDL, $c\exp(-z\zeta e/kT)$.

et al.[21] to gain intuition into the spread of CP enrichment and depletion zones at constant voltage. This analysis provides closed-form relations showing that, for large times, the enrichment and depletion regions in a constant-voltage experiment grow proportionally to the square root of time. We validate this prediction and compare it to the constant current case using computational and experimental results. Finally, we use analysis and computations to show that at long times, the rate of thickening of the enrichment shock can match its propagation rate. This leads to growth which can be mistaken for simple diffusion or a non-propagating form of CP, but which is instead simply explained by an increasingly current-limited shock propagation phenomena.

3.2 Analytical Model

We present a simple one-dimensional analysis for the system shown in Figure 3.1. We draw on an existing model,[21,30] but explore and expand on the special case of constant applied potential. Previous work[21,30] showed that propagating CP enrichment and depletion fronts spread as shock waves with velocities linearly proportional to the current through the system. Furthermore, the shock thickness is inversely proportional to the difference of the characteristic ion transport velocities on either side of the shock and thus inversely proportional to the current:

$$\frac{d}{dt}x_d \sim I \text{ and } \Delta_d \sim I^{-1}, \tag{3.1}$$

where x_d and Δ_d represent the axial location and thickness of the depletion shock, respectively (see Figure 3.1). For constant-current this yields a constant-thickness shock advancing linearly in time as observed by Zangle *et al.*[21] In the constant voltage case, however, the current through the system changes as CP dynamics modify the system resistance. As the depletion shock propagates, it trails a region of low conductivity which dominates overall impedance. The resistance of the system increases linearly with axial length of this depleted region. Assuming the depletion shock interface is significantly smaller than the channel length:

$$R_{system}(t) \approx R_0 + Cx_d(t), \tag{3.2}$$

where R_{system} represents the total electric resistance of the system, R_0 is the initial resistance and C represents the resistance per unit length of the growing depletion region. In Eq. (3.2), we neglect the decrease of resistance due to growth of the enrichment region relative to the effect of the depletion growth. This is because typically the increase in concentration inside the enrichment region is of order unity whereas the concentration in the depletion region is orders of magnitude lower than the initial concentration.[21,30] Using Eq. (3.2) to express the resistance of the system, we can rewrite Eq. (3.1) as:

$$\frac{d}{dt}x_d \sim \frac{V}{R_{system}}, \tag{3.3}$$

where V is the applied voltage. Substituting Eq. (3.2) into Eq. (3.3) yields the following differential equation for x_d:

$$\frac{d}{dt}\left(R_0 x_d + \tfrac{1}{2} C x_d^2\right) \approx V. \tag{3.4}$$

Over sufficiently long times (when $Cx_d \gg R_0$) the second term on the left hand side of Eq. (3.4) dominates the first term, and this leads to the following scaling for shock location:

$$\frac{d}{dt}x_d \sim t^{1/2}. \tag{3.5}$$

Therefore, at long times the resistance of the depletion region dominates and I scales as V/x_d. From Eq. (3.1) this leads to the following scaling for the shock thickness:

$$\Delta_d \sim t^{1/2}. \tag{3.6}$$

Note that here we implicitly assumed that the shock structure has a fast response to instantaneous changes in current. A similar analysis (again assuming that the depletion shock dominates the total resistance) for the enrichment shock location and thickness yields

$$\frac{d}{dt}x_e \sim t^{1/2},\ \Delta_e \sim t^{1/2}. \tag{3.7}$$

From Eq. (3.5)-(3.7), we see that shock advancement and thickening are both proportional to $t^{1/2}$. Under certain conditions (i.e., low enough Peclet number, $Pe_L = U_b L / D$, where, L is characteristic axial channel length, U_b is bulk velocity and D is ion diffusivity) the theoretical rate of shock thickening can be on the order of the propagation rate. In this case, a moving "shock" structure (i.e., a sharp interface propagating away from the microchannel-nanochannel interface) is not clearly observed. Instead, the system's response is that of a gradually slowing and thickening enrichment interface. Over sufficiently long time ($t \sim \left(L/D\right)^{0.5}$), the growth of enrichment and depletion zones will be arrested by diffusive interaction with end-channel reservoirs.

For higher Pe_L, this scaling predicts growth of the depletion region as $t^{1/2}$, where shock widths are much smaller than the axial width of enrichment/depletion zones. In this case the shock scale can be distinguished from the propagation scale, although both grow as $t^{1/2}$.

Below, we verify the simple asymptotic behaviors predicted here using experiments and computations.

3.3 Computational Model

Figure 3.2 presents computational results for both constant-current and constant-voltage cases from the code and numerical scheme described in Zangle *et al.*[21]. Figure 3.2(a) shows a 1 mM initial concentration, and 2(b) a 250 μM initial concentration. In constant voltage simulations, we rescale the input current at each time step to maintain a specified voltage between the ends of the channel system. This rescaling is justified as the relation between current and voltage is linear (see Mani *et al.*,[30] equation 22).

As in Zangle *et al.*,[21] we used wall surface charge density inside the nanochannel, σ_{nano}, as the only fitting parameter between theory and experiments. Wall charge inside the microchannel, σ_{micro}, was set equal to the value determined by independent zeta-potential measurements. In Figure 3.2(a) $\sigma_{nano} = 0.25\sigma_{micro}$ and in Figure 3.2(b) $\sigma_{nano} = \sigma_{micro}$. All other parameters (including channel height, initial concentration, ion mobilities and diffusivities) were set equal to experimental values based on independent measurements reported previously.[21]

The constant current results in Figure 3.2(a) show linear growth of enrichment and depletion regions with time (shock fronts are linear on the spatiotemporal plot). In contrast, the constant voltage results in Figure 3.2(b) show curved, parabolic spreading of enrichment and depletion regions with time. We show parabolic fits to contours of $c = 0.6\ c_{max}$ and $c = 0.05\ c_{max}$ (dashed blue curve), which have R^2 values of 0.9996 and 0.994, respectively, indicating the scaling of the dynamics is well predicted by Eqs. (3.5) and (3.7).

Figure 3.3 shows computational results at applied voltages of 10, 100, and 1000 V, for the same conditions as those of Figure 3.2(b). For all of these cases, the analytical theory of Mani *et al.*[30] predicts propagating CP. At high voltages (1000 V in this case), the enrichment shock thickness, Δ_e, remains small relative to the enrichment region width, x_e, and this shock clearly propagates over long times. At lower voltages (10 V in this case) the growth of the CP enrichment region is slow relative to thickening of the enrichment shock. In this case, the enrichment region shock velocity slows down considerably, resulting in a long time condition where $t^{1/2}$-type growth of the interface width dominates. These results suggest that prior observations of CP at constant voltage in which the enrichment front appeared to gradually slow or stop[33,56] are consistent with the model of Mani *et al.*[30] and Zangle *et al.*[21] and can be explained by strong initial propagation followed by $t^{1/2}$-type decay of propagation velocity and $t^{1/2}$ growth of interface width. Note that diffusion plays an important role, but this process is primarily due to the coupling of shock dynamics and the decreasing current associated with constant voltage.

3.4 Experimental Measurements

We also performed a series of new experiments to test the predictions of Eqs. (3.5) and (3.7). Details of channel design and fabrication are described in Zangle *et al.*[21] We filled series microchannel-nanochannel-microchannel devices with either 1 mM

(Figure 3.2(c)) or 250 μM (Figure 3.2(d)) Alexa Fluor 488 dye in deionized water. With this system we can directly observe the behavior of the background electrolyte (the fluorescent Alexa Fluor species and its lithium counter-ion) using epifluorescent microscopy.[21]

Figure 3.2(c) shows experimental results for a constant 800 pA current in a system with an initial concentration of 1 mM Alexa Fluor 488. At this condition the enrichment and depletion shocks move at nearly constant velocity as predicted by theory and in agreement with the computations presented in Figure 3.2(a).

Figure 3.2(d) shows experimental results for a channel initially filled with 250 μM Alexa Fluor 488 at a constant voltage of 100 V. This result shows an enrichment front migrating as $t^{1/2}$ as predicted by equation (3.5) and consistent with the computational results in Figure 3.2(b). The R^2 values for the parabolic best fit line to $c/c_{max} = 0.6$ (210 points) and the $c = 0.05$ (45 points) contours were respectively 0.999 and 0.991. These fits are plotted in Figure 3.2(d) as dashed lines. The goodness-of-fit of these parabolas confirm the prediction of Eq. (3.7) that in a constant voltage experiment, CP enrichment shocks spread as $t^{1/2}$.

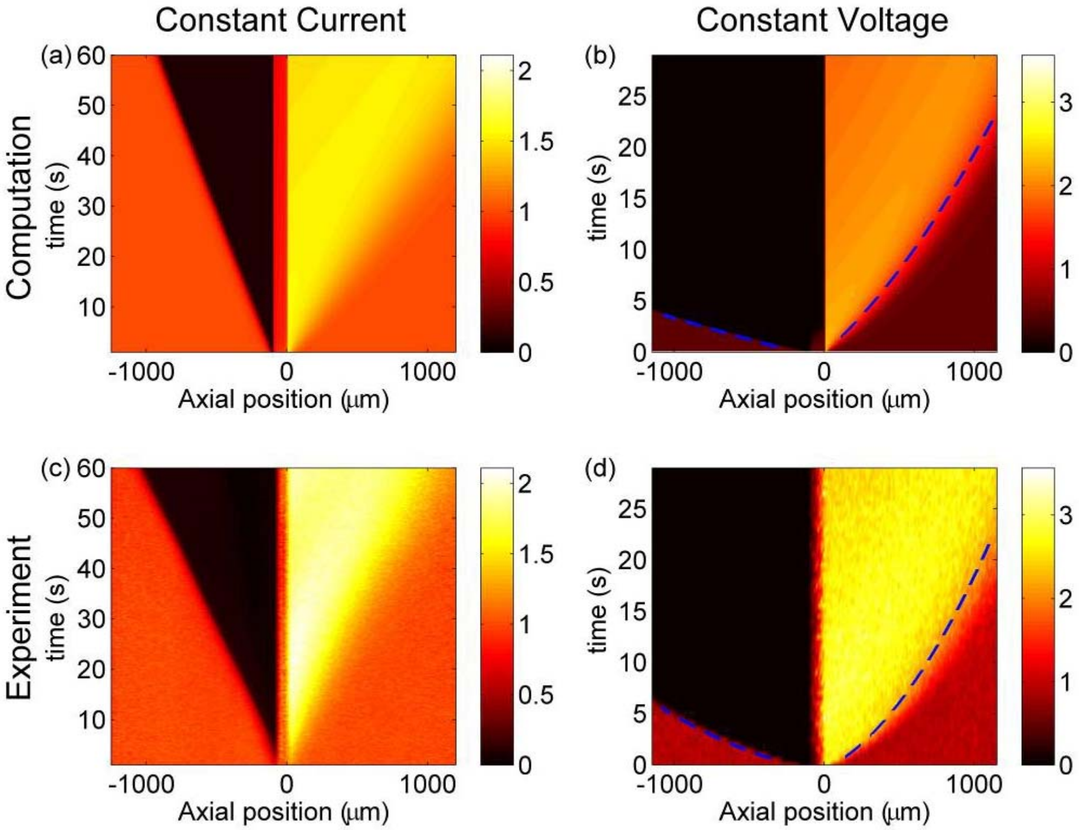

Figure 3.2 Computational and experimental results showing spatiotemporal plots for constant current and constant applied voltage. Computations are shown in the top row, experiments in the bottom row. The first column shows computational and experimental results for constant current conditions. The second column shows constant voltage results. In these spatiotemporal plots, distance is plotted on the *x*-axis, time on the *y*-axis, and the color map corresponds to concentration (yellow/white is high, black is low). The 100 μm long nanochannel starts at $x = 0$. Constant current conditions (a, c) show roughly linear spread of enrichment and depletion shocks with time while constant voltage conditions (b, d) show parabolic spread of enrichment and depletion shocks, as predicted by theory. Parabolic least-squares best fit lines ($t = Ax^2 + Bx + C$) to contours of $c = 0.6\ c_{max}$ and $c = 0.05\ c_{max}$ are shown as dashed, blue lines in (b) and (d). The colormap of concentration relative to initial concentration is shown to the left of each spatiotemporal plot.

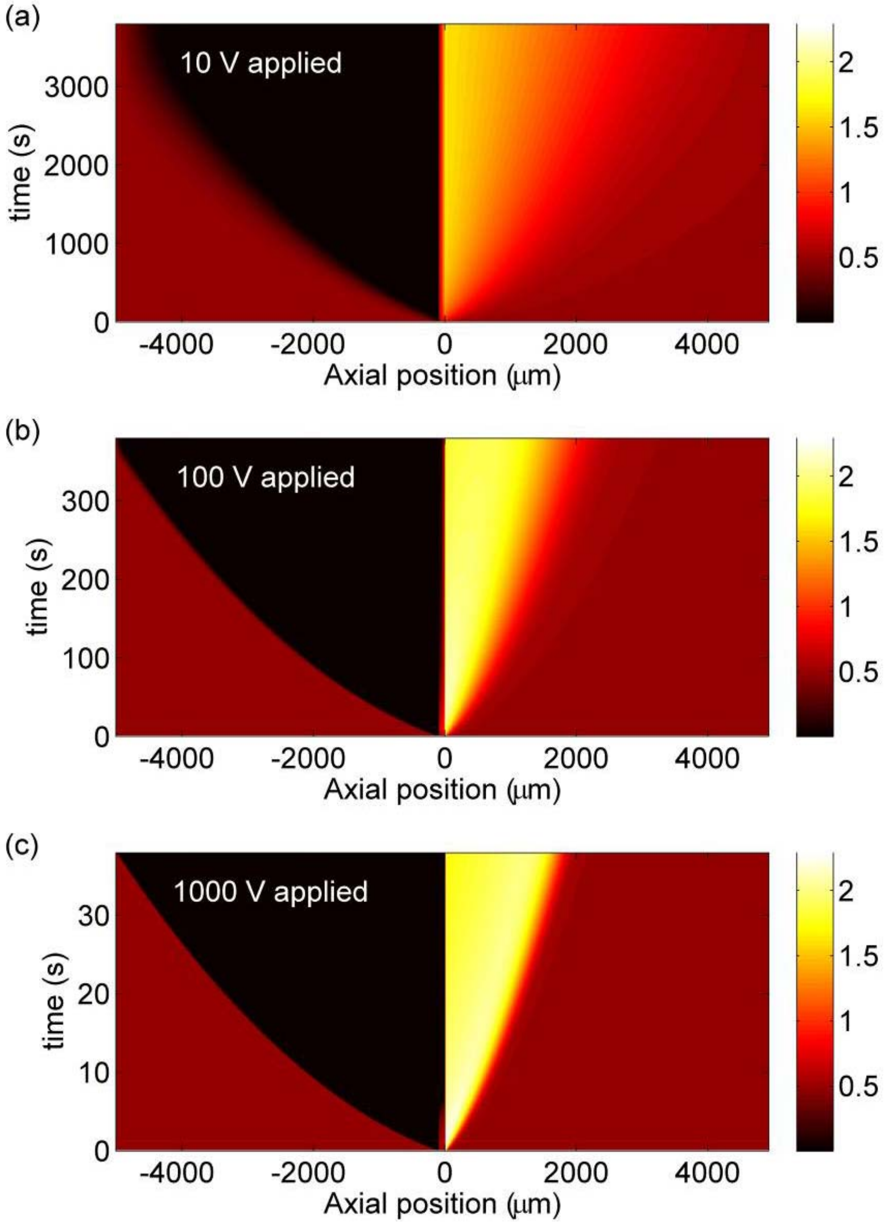

Figure 3.3 Computational results for applied potentials of (a) 10 V, (b) 100 V and (c) 1000 V, at otherwise the same conditions as in Figure 3.2(c) and Figure 3.2(d). At low voltage, the results show that (a) thickening of the enrichment shock dominates the spread of the enrichment region and the shock slows drastically and may be mistakenly reported to stop moving. At high voltage, (c) the shock thickness is small relative to the size of the growing enrichment region and the shock clearly propagates to the cathode side reservoir. The colormap of concentration relative to initial concentration is shown to the left of each spatiotemporal plot.

3.5 Section Conclusions

In summary, we presented a brief, analytical derivation which draws on the model of Mani *et al.*[30] showing that under constant voltage conditions, CP enrichment and depletion regions have propagation velocities which scale as $t^{1/2}$ while the enrichment and depletion shock thicknesses grow as $t^{1/2}$. Using new computations and experiments we confirmed this scaling derivation and the parabolic spatiotemporal growth of the width of CP enrichment and depletion regions for constant voltage conditions. Computations for low applied voltage show that at long times and low Peclet numbers, the growth of CP enrichment and depletion regions is slow relative to shock thickening. This $t^{1/2}$ shock thickening can be mistaken for an arrested (stopped) propagation of CP enrichment and depletion regions or for a simple one-dimensional diffusion-dominated process. Instead, this $t^{1/2}$ growth of the shock interface width is due to a coupling of the shock propagation dynamics (in which diffusion plays a key role) and the gradual decrease in current due to constant applied voltage and the growing depletion region. Together, these results help explain the distinctly different observations of CP at constant voltage versus constant current conditions.

4 Analyte Species Behavior in Systems with Concentration Polarization

The contents of this chapter have been accepted for publication by *Chemical Society Reviews* (Zangle, T. A., Mani, A., and Santiago, J. G., "Theory and experiments of concentration polarization and ion focusing at microchannel and nanochannel interfaces," Chemical Society Reviews, 2010, DOI: 10.1039/b902074h, http://xlink.rsc.org/?doi=B902074H.)[1] and are reproduced here by permission of The Royal Society of Chemistry with minor modifications.

4.1 Introduction

In order to use hybrid microfluidic-nanofluidic devices for biological or chemical analysis we must first understand the behavior of target ionic species (analytes) in these systems. A large number of experimental studies[16-17,20-22,24,27,29,31-33,47-48,52-59,78] have addressed the influence of CP on the transport of an analyte ion with a concentration relatively low compared to background ions in hybrid microfluidic-nanofluidic systems. To date we know of only two papers which have attempted to explain and categorize several of these experimental results. However, the first is only a preliminary work we published on this topic,[29]and the second consisted of a (transient) one-dimensional computational model.[28] In this chapter we extend recent theoretical developments[30] to provide a more generalized analytical framework for understanding the effects of CP on both background and analyte ion transport in hybrid microfluidic-nanofluidic systems.

In this chapter we describe the effects of CP on cationic and anionic analytes, in systems with negatively charged nanochannel walls (we will focus all of our discussions on the case of negatively charged walls). A schematic of the system including possible focusing or stacking zones (which we will examine in detail in this chapter) is shown in Figure 4.1.

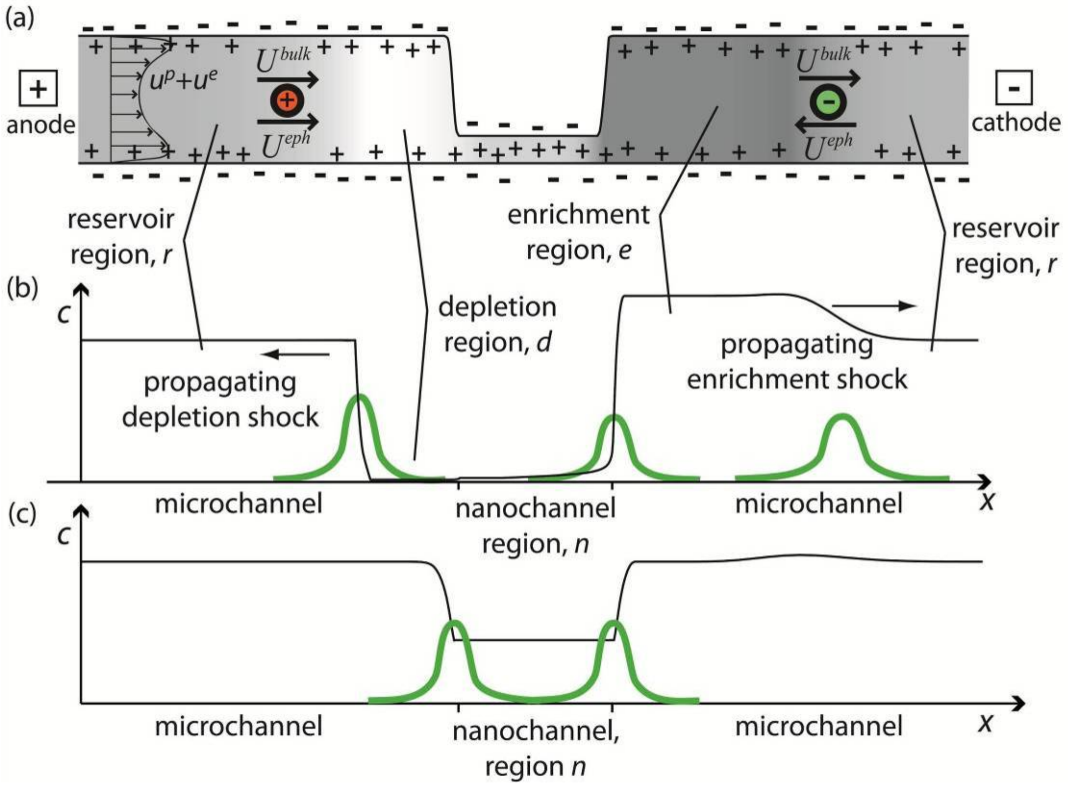

(a)
anode
cathode
u^p+u^e
U^{bulk}
U^{eph}
U^{bulk}
U^{eph}
reservoir region, r
enrichment region, e
reservoir region, r
(b)
c
depletion region, d
propagating depletion shock
propagating enrichment shock
microchannel
nanochannel region, n
microchannel
x
(c)
c
microchannel
nanochannel, region n
microchannel
x

Figure 4.1 Schematic showing various possibilities of anionic species focusing or stacking in a typical microchannel-nanochannel geometry. (a) shows a typical microchannel-nanochannel-microchannel layout with enrichment and depletion of the background electrolyte (BGE) shown as a greyscale map (darker regions correspond to enrichment). The 'reservoir' region is the section of microchannel which is not yet affected by progress of CP front; therefore, the concentration of each ion in this region is equal to the concentration inside the end-channel reservoir (not shown). Focusing of a low-concentration anionic species occurs in zones where the sum of the electrophoretic and (area-averaged) bulk velocities are locally zero with a negative divergence.[7] For counter-ionic (positive for negatively charged walls) species, focusing is not possible since these species always have positive total velocity. The black curve in (b) shows computed BGE concentration from a propagating CP case.[21] The green peaks represent possible focusing or stacking zones for a low concentration anionic analyte,[*]

---

[*] Consistent with Bharadwaj *et al.*,[7] we use focusing to describe the condition where there is a focal point for the analyte. A focal point is a point or region in some reference frame where the drift velocity of the focused species changes sign so that sample is driven to the focal point. We use "stacking" to describe the

whose concentration is much lower than the BGE. The black curve in (c) shows a computed no-propagation case.[21] Here we show two possible focusing locations for analyte anions.

In our discussion of low concentration analyte ions, we will examine electrokinetic preconcentration at microchannel-nanochannel interfaces. However, we note that other preconcentration modes are possible. For example, Foote *et al.*[81] fabricated silica nanoporous membranes and preconcentrated proteins using size exclusion. Similarly, Meagher *et al.*[82] used a size-exclusion preconcentrator to improve the limit-of-detection of an on-chip immunoassay from 300 pM to <10 pM. For a more thorough overview of size exclusion techniques using nanoporous membranes and nanochannels, see the recent review by Han *et al.*[83] We note, however, that CP has been observed to influence the performance of nanoporous membranes (including size-exclusion-based systems) under conditions in which the nanoporous membrane is charged. Hlushkou *et al.*[56] reported on the preconcentration efficiencies at charged and uncharged nanoporous membranes and found that much higher field strengths are required to achieve the same preconcentration factor with charged membranes due to the CP depletion region. This depletion zone acts as a large electrical resistance, increasing the required applied electric potential. In a paper on an integrated size-exclusion preconcentrator, Hatch *et al.*[25] reported a decrease in current with time due to growth of an anode-side, CP depletion zone; this had an adverse effect on repeatability of the subsequent separation in polyacrylamide sieving matrix. A similar effect has been observed in DNA capillary separation though a gel.[84]. CP effects in membrane preconcentration can perhaps be mitigated by avoiding trans-membrane current during a separation step (following a size-exclusion preconcentration)[25] or by applying current through the membrane only for a short time.[82]

---

less stringent situation where an analyte drift velocity decreases in magnitude (causing an increase in concentration) as the analyte migrates through some stacking region containing an electric field gradient.

4.2 Cationic species

In this section, we first present a model to predict the behavior of a cationic analyte (a positively charged species which is in low concentration relative to the background electrolyte). Next, we examine the predictions of the model relative to several sets of experiments from the literature. Several investigators have reported experiments with low concentrations of positively charged Rhodamine 6G[31-32,48,57-58,78] or Rhodamine 123[20] in a system with negatively charged nanochannel walls. Therefore, in this section we will analyze systems using these two fluorescent dyes as representative cationic analytes to test the analytical model predictions.

4.2.1 Analytical predictions

First, we will develop predictions for the behavior of a cationic analyte in a microchannel-nanochannel-microchannel system, as shown in Figure 4.2. Cationic analytes electromigrate in the direction of the bulk flow and, so, in a linear microchannel-nanochannel system with negative wall charge, the cation's total species velocity in the frame of reference of an interface (the sum of the electrophoretic and bulk velocities, $U_i^{eph} + U^{bulk}$, minus the interface velocity V^{int}) is always positive; and so the cation cannot focus in a microchannel-nanochannel system with CP.[†] Cationic analytes, however, can stack (i.e., increase in concentration as they traverse some interface due to a decrease in total species velocity, U_i^{tot}) or undergo electromigration dispersion (decrease concentration as they traverse some interface due to an increase in total species velocity, U_i^{tot}). We describe the behavior of cationic analytes by following an approach similar to that of Chambers *et al.*[85] who analyzed the analogous situation of ions which move through but do not focus in isotachophoretic (ITP) zones.[‡] Our analysis uses the analytical results of Mani *et al.*[30] to describe the background electrolyte (BGE) concentration and electric field everywhere in a microchannel-nanochannel-microchannel system. Then, we determine the concentration of cationic species which is required to balance the total flux across each interface in the system. Note that in this system the only interfaces where the total species velocity can change are the depletion shock, microchannel-nanochannel interfaces and the enrichment shock as shown in Figure 4.2. Because cationic species move from the anode to the cathode, we assume that cations of interest start at the anode-side microchannel where the concentration is equal to the reservoir concentration, and proceed towards the cathode. For simplicity we assume also that the valence of the analyte is the same as the valence of the cation in the BGE and that the mobility of each species in the system is constant (e.g., we do not consider ionic strength or pH effects on mobility[86]). This analysis is presented in detail in the following sections.

[†] The enrichment shock is the only interface in such a system where V^{int} is positive and nonzero. However, Mani *et al.*[30] and Zangle *et al.*[21] showed that this interface travels at the bulk velocity, so $U^{bulk} = V^{\mathrm{int}}$. Therefore, the total species velocity (in this interface frame of reference) on either side of this interface will be U_i^{eph} which has the same sign on either side of the enrichment shock.

[‡] Their work considers ions which move in the same (over-speeder) or opposite (counter-speeder) directions as the ITP velocity. We extend this to describe channels with variable depth and to include the effects of bulk flow on total species velocity.

As shown in Figure 4.2, the microchannel-nanochannel-microchannel system can in general be divided into the following five distinct zones: 1. the undisturbed left-side microchannel, with the same concentration as in the reservoir; 2. the depletion region (if CP propagates); 3. the nanochannel; 4. the enrichment zone (if CP propagates), and 5. the undisturbed right-side microchannel. These five zones are separated by four boundaries which present possible interfaces for stacking or focusing of a cationic analyte. We assume that the cationic analyte is released from the anode-side reservoir into the channel system. In addition, we assume that the analyte is released after the nanochannel establishes its equilibrium condition.[§] Furthermore, we consider low concentration cationic analytes compared to the background electrolyte (BGE), so that it cannot affect the axial electric field. Also, in this derivation and the anionic analyte derivation below, following the analysis of Mani *et al.*[30] we will assume high $Pe\,L/h$ (i.e., high product of Peclet number based on channel height and the ratio of channel length to nanochannel height) and so will not present results as a function of the applied potential or electric field.

[§] Since the nanochannel used in these experiments is typically short relative to the microchannel, we assume the nanochannel reaches its steady-state condition quickly relative to the propagation of shocks in the microchannel system.

We first review the results of the simple theory of Mani *et al.*[30] for the BGE, which determines transport regimes (final concentrations and electric fields in propagating vs. non-propagating CP) in the system. Then we use their theory as a foundation to describe the effects of CP on low concentration cationic analytes.

The simplest model presented by Mani *et al.*[30] suggests that the bulk concentration of binary electrolyte in a channel system satisfies the following one-dimensional differential equation:

$$\frac{\partial}{\partial t^*}\left(h^* c_0^*\right)+\frac{\partial}{\partial x^*}\left(c_0^*+\frac{I^*}{h^* c_0^*+1}\right)=\frac{1}{\mathrm{Pe}}\frac{\partial}{\partial x^*}\left(h^*\frac{\partial c_0^*}{\partial x^*}\right), \qquad (4.1)$$

where h^* is the height of the channel, non-dimensionalized by a nanoscale reference height, h_{ref}. c^* is the nondimensional bulk concentration using the wall surface-charge density, σ, which is assumed to be constant and uniform in this model:

$$c_0^*=\frac{\nu_1 z_1-\nu_2 z_2}{2\nu_1 z_1}\frac{F z_1 h_{\mathrm{ref}} c_0}{-\sigma}. \qquad (4.2)$$

With this notation, $c_0^* h^*$ is the local inverse Dukhin number. I^* is the nondimensional current through the system relative to the bulk flow rate:

$$I^*=\frac{\nu_2 z_2}{2\nu_1 z_1}\frac{I h_{\mathrm{ref}}}{\sigma Q}, \qquad (4.3)$$

where Q is the bulk flow rate. The axial coordinate and time are nondimensionalized by h_{ref} and h_{ref}^2/Q respectively.

Eqn (4.1) is a nonlinear advection-diffusion equation for evolution of the BGE, c_0^*. The nondimensional advection flux has two terms: c_0^* which represents linear advection by the bulk flow rate, and $I^*/(h^* c_0^*+1)$ which represents exchanges between the bulk and EDL. The axial electric field in the system is the ratio of the current and local conductivity:

$$E = \frac{I}{Fz_1\left[F\left(\nu_1 z_1 - \nu_2 z_2\right)hc_0 - 2\nu_1\sigma\right]}. \tag{4.4}$$

The total conductivity appeared in the denominator of eqn (4.4) consists of bulk effects of co- and counter-ions and the EDL conductivity. Note that c_0 is the bulk concentration of counter-ions in the BGE. From net neutrality, bulk concentration of coin would be $z_1 c_0 / \left|z_2\right|$, which would lead to the expression in denominator of eqn (4.4) for conductivity.

An analyte ion with mobility ν_i and valence number of z_i would experience an electromigration velocity equal to $\nu_i z_i FE$. Using eqn (4.4) and the nondimensionalization procedure from Mani *et al.*[30] we arrive at the following expression for nondimensional electromigration velocity of the analyte:

$$\frac{\text{electromigration velocty}}{\text{bulk velocity}} = \frac{\nu_i z_i FEH}{Q} = \frac{\nu_i z_i}{-\nu_2 z_2}\frac{h^* I^*}{h^* c_0^* + 1}. \tag{4.5}$$

In the system considered here, the current and flow rate are not independent of each other. The current drives the electroosmotic flow through the system and the internal pressure gradients created at the microchannel-nanochannel interfaces adjust the flowrate in accordance with mass conservation. Since the nanochannel has the dominant hydraulic resistance, one can assume that the electroosmotic flow in the nanochannel determines the flow rate of the entire system. Using this assumption Mani *et al.*[30] showed that:

$$I^* = \frac{\nu_2^*}{h_n^*}\left(h_n^* c_{0,n}^* + 1\right). \tag{4.6}$$

As described earlier, ν_2^* is the nondimensional mobility of coions to the wall charge. It is with the assumption of eqn (4.6) that the entire BGE system can be parameterized by two parameters, ν_2^* and inverse Dukhin number in the nanochannel, $c_{0,r}^* h_n^*$. Substituting eqn (4.6) into eqn (4.5) yields:

$$\frac{\nu_i z_i FEh}{Q} = \nu_i^* \frac{h^*\left(h_n^* c_{0,n}^* + 1\right)}{h_n^*\left(h^* c_0^* + 1\right)}, \tag{4.7}$$

where ν_i^* is the nondimensional mobility of the analyte specie. Eqn (4.7) can be used to determine the global translocation of ions at each zone in the channel system. In the following sections, we use this equation to analyze stacking of cationic analytes for different CP regimes.

4.2.2 Non-propagating CP

If CP does not propagate, the channel system will present three zones as shown in Figure 4.1c: 1. the left-side microchannel, with uniform concentration the same as concentration in the reservoir; 2. the nanochannel; and 3. the right-side microchannel with uniform concentration the same as in the reservoir. Stacking is possible at either of the two interfaces between the microchannels and the nanochannel. For this case, the equilibrium BGE concentration in the nanochannel would be lower than the reservoir's concentration due to significant flux carried by the EDL[30]

$$c_{0,n}^{*} = c_{0,r}^{*} - \frac{\nu_2^{*}}{h_n^{*}}. \qquad (4.8)$$

If one releases a cation analyte specie, *i*, into the left reservoir with concentration $c_{i,r}$, the analyte will travel through the left-side microchannel. Ignoring the EDL effects (in this microchannel with $c_{0,r}^{*} h_r^{*}$ >>1), the flux of the analyte in the left-side-microchannel is:

$$f_{i,r} = c_{i,r}\left(Q + \nu_i z_i F E_r h_r\right). \qquad (4.9)$$

In general, the concentration of the analyte in the nanochannel, $c_{i,n}$ would be different from its concentration in the microchannels. The flux of the analyte in the nanochannel can be written as:

$$f_{i,n} = c_{i,n}\left(Q + \nu_i z_i F E_n h_n\right) + f_{i,n}^{\mathrm{EDL}}, \qquad (4.10)$$

where $f_{i,n}^{EDL}$ is the flux of species *i* in the nanochannel (region *n*) through the EDL. We note that $c_{i,n}$ represents only the bulk concentration of the analyte; therefore, to account for the total flux, the EDL contribution should be added. To estimate the portion of the analyte in the EDL here we assume that the analyte is distributed between the bulk and the EDL with the same proportion as in the cationic BGE. This assumption is only valid when the analyte has the same valence number as the cation in the BGE and thus satisfies the same Boltzmann distribution in the wall-normal direction:

$$\frac{\int_0^h c_i^{\mathrm{EDL}} dy}{c_i^{\mathrm{Bulk}} h} = \frac{\int_0^h c_0^{\mathrm{EDL}} dy}{c_0^{\mathrm{Bulk}} h} = \frac{-2\sigma / F z_1}{c_0 h} . \tag{4.11}$$

The second equality in eqn (4.11) is consistent with the simple theory of Mani *et al.*,[30] assuming that only the excess concentration of cations contributes to formation of the EDLs. Following the nondimensionalization procedure of Mani *et al.*,[30] the right-hand-side of eqn (4.11) can be written in terms of nondimensional quantities as:

$$\frac{\int_0^h c_i^{\mathrm{EDL}} dy}{c_i^{\mathrm{Bulk}} h} = \left(\frac{1 - \nu_2 z_2 / \nu_1 z_1}{c_0^* h^*} \right) . \tag{4.12}$$

To simplify the algebraic manipulations, in the next steps we here assume that the BGE is a symmetric electrolyte (i.e., mobility and valence for the anionic BGE species equal the mobility and valence for the cationic BGE species. With this simplification, the numerator of eqn (4.12) reduces to a value of 2 and we arrive at a simple expression for the EDL to bulk contribution of analyte cations in terms Dukhin number based on the BGE concentration:

$$\frac{\int_0^h c_i^{\mathrm{EDL}} dy}{c_i^{\mathrm{Bulk}} h} = \frac{2}{c_0^* h^*} . \tag{4.13}$$

Using this expression we can write the EDL flux in eqn (4.10) as a simple correction to the bulk flux.

$$f_{i,n} = c_{i,n} \left[Q + \nu_i z_i F E_n h_n (1 + 2 / c_{0,n}^* h_n^*) \right] . \tag{4.14}$$

We note that consistent to the simple model of Mani *et al.*[30] we here assumed that ions in the EDLs are only transported via electromigration. The correction factor, $(1 + 2 / c_{0,n}^* h_n^*)$ is simply the total to bulk concentration ratio for counterions. Due to conservation of conterionic analyte *i,* the flux of the analyte in the microchannel is equal to that in the nanochannel. By equating the expressions in eqns (4.9) and (4.14) one can obtain an expression for the stacking ratio of the analyte:

$$\frac{c_{i,n}}{c_{i,r}} = \frac{Q + \nu_i z_i F E_r h_r}{Q + \nu_i z_i F E_n h_n \left(1 + 2 / c_{0,n}^* h_n^* \right)} . \tag{4.15}$$

With this form stacking ratio is defined in terms of analyte concentrations in the bulk. A more useful quantity, however, is the stacking ratio in terms of the cross-sectional area-averaged concentrations (height-averaged concentrations in this case). This requires us to include the EDL contribution in the definition of stacking ratio. In our notation we use $S_{i,n/r}$ to refer to the area-averaged stacking ratio from region *r* to region *n* for analyte specie *i*.

$$S_{i,n/r} \equiv \frac{c_{i,n}\left(1+2/c^*_{0,n}h^*_n\right)}{c_{i,r}} = \frac{1+\nu_i z_i F E_r h_r / Q}{1/\left(1+2/c^*_{0,n}h^*_n\right)+\nu_i z_i F E_n h_n / Q}. \qquad (4.16)$$

In the next step we can write the stacking ratio in terms of system parameters, $c^*_{0,r}h^*_n$, ν^*_2, and ν^*_i. This can be simple done by substituting eqn (4.7) into (4.16) and then substituting eqn (4.8) into the resulting expression. Ignoring the EDL contribution of the microchannel, when evaluating eqn (4.7) for region *r* (ie. ignoring 1 relative to $h^*_r c^*_{i,r}$) leads to the following expression for $S_{i,n/r}$:

$$S_{i,n/r} = \frac{c^*_{0,r}h^*_n + \nu^*_i\left(c^*_{0,r}h^*_n - \nu^*_2 + 1\right)}{c^*_{0,r}h^*_n - \nu^*_2 + \nu^*_i\left(c^*_{0,r}h^*_n - \nu^*_2 + 2\right)} \frac{c^*_{0,r}h^*_n - \nu^*_2 + 2}{c^*_{0,r}h^*_n}. \qquad (4.17)$$

It will be useful to write this expression in terms of stacking ratio of the background electrolyte, $S_{0,n/r}$ (here in terms of background cations). Having $S_{0,n/r} = (1+2/c^*_{0,n}h^*_n)c_{0,n}/c_{0,r}$ (see definition in eqn (4.16), eqn (4.17) can be written in the following form:

$$S_{i,n/r} = S_{0,n/r}\frac{1-\nu^*_i / c^*_{0,r}h^*_n + \nu^*_i S_{0,n/r}}{1-\nu^*_2 / c^*_{0,r}h^*_n + \nu^*_i S_{0,n/r}}, \qquad (4.18)$$

where $S_{0,n/r}$ is equal to $(c^*_{0,r}h^*_n - \nu^*_2 + 2)/(c^*_{0,r}h^*_n)$. We note that since this expression is for non-propagating CP the denominator of eqn (4.18) will never equal zero. Also, eqn (4.18) indicates that if the analyte is slower than the BGE ($\nu^*_i < \nu^*_2$) then the stacking ration of the analyte will be higher than the stacking ratio of the background electrolyte cation.

4.2.3 Propagating CP, $\nu^*_2 \geq 1$

For this case we will start by computing the stacking ratio across the depletion front. We consider a control volume around the depletion shock moving with the shock velocity. The flux of analyte species from region *r* into this control volume is:

$$f_{i,r} = c_{i,r}\left(Q - V_{\text{shock}} h_r + \nu_i z_i F E_r h_r\right). \tag{4.19}$$

The depletion shock velocity given by the theory of Mani *et al.* is equal to

$$\frac{V_{shock} h_r}{Q} = 1 - \frac{2\nu_2^* - 1}{c_{0,r}^* h_n^*}. \tag{4.20}$$

The flux of analyte species from the control volume into the depletion zone can be written in a similar fashion. However, note that since the bulk concentration is very low in the depletion zone, the EDL contribution is not negligible in this zone and should be considered in the expression for the flux. Following a similar method that lead to eqn (4.14), we can write:

$$f_{i,d} = c_{i,d}\left[Q - V_{\text{shock}} h_d + \nu_i z_i F E_d h_d \left(1 + 2 / c_{0,d}^* h_d^*\right)\right]. \tag{4.21}$$

Since the background electrolyte has a very low concentration in the depletion region, current conservation demands an extremely high electric field in this region. Therefore the flux associated with the electric field has the dominant contribution in the flux term and thus, $f_{i,d}$ can be approximated as:

$$f_{i,d} \simeq c_{i,d} \nu_i z_i F E_d h_d \left(1 + 2 / c_{0,d}^* h_d^*\right). \tag{4.22}$$

By equating the flux expressions in eqns (4.22) and (4.19) and using eqn (4.20), one can obtain an expression for the stacking ratio from the reservoir to the depletion zone:

$$S_{i,d/r} \equiv \frac{c_{i,d}}{c_{i,r}}\left(1 + 2 / c_{0,d}^* h_d^*\right) = \frac{\dfrac{2\nu_2^* - 1}{c_{0,r}^* h_n^*} + \nu_i^* \dfrac{h_r^*(c_{0,n}^* h_n^* + 1)}{h_n^*(c_{0,r}^* h_r^* + 1)}}{\nu_i^* \dfrac{h_d^*(c_{0,n}^* h_n^* + 1)}{h_n^*(c_{0,d}^* h_d^* + 1)}}. \tag{4.23}$$

Here, we used eqn (4.7) to express the ratios of electromigration fluxes to the advective flux. Mani *et al.*[30] found the following expressions for the BGE concentrations in the depletion zone and the nanochannel:

$$c_{0,d}^* h_d^* = \frac{(\nu_2^* - 1)^2}{2\nu_2^* - 1}, \quad c_{0,n}^* h_n^* = \nu_2^* - 1. \tag{4.24}$$

Using these expressions in eqn (4.23) and noting $c_{0,r}^* h_r^* \gg 1$ for a typical microchannel leads to

$$S_{i,d/r} = \frac{\nu_2^*(2\nu_2^* - 1 + \nu_i^* \nu_2^*)}{\nu_i^*(2\nu_2^* - 1) c_{0,r}^* h_d^*}. \tag{4.25}$$

Rewriting this equation in terms of stacking ratio of the BGE leads to

$$S_{i,d/r} = S_{0,d/r}\left(\frac{\nu_2^*}{\nu_i^*}\right)\frac{2\nu_2^* - 1 + \nu_i^*\nu_2^*}{2\nu_2^* - 1 + \nu_2^{*2}}, \tag{4.26}$$

which is a monotonically decreasing function of ν_i^*.

Next, we derive an expression for the stacking between depletion zone and the nanochannel. Since the electromigration flux is the dominant term in the depletion zone, eqn (4.22) is still a good approximation for the flux in the depletion zone (although this equation was originally derived for a moving control surface). The flux in the nanochannel is already derived in eqn (4.14) except here the value of the nanochannel concentration should be replaced from eqn (4.24).

$$S_{i,n/d} \equiv \frac{c_{i,n}(1+2/c_{0,n}^*h_n^*)}{c_{i,d}(1+2/c_{0,d}^*h_d^*)} = \frac{\nu_i z_i F E_d h_d}{Q/(1+2/c_{0,n}^*h_n^*) + \nu_i z_i F E_n h_n}. \tag{4.27}$$

Using eqns (4.7) and (4.24) into eqn (4.27) leads to

$$S_{i,n/d} = \frac{h_d}{h_n}\left(\frac{\nu_i^*}{\nu_2^*}\right)\frac{\left(\nu_2^* + 1\right)\left(2\nu_2^* - 1\right)}{\nu_2^* - 1 + \nu_i^*\left(\nu_2^* + 1\right)}. \tag{4.28}$$

Rewriting this equation in terms of stacking ratio of the BGE leads to

$$S_{i,n/d} = S_{0,n/d}\left(\frac{\nu_i^*}{\nu_2^*}\right)\frac{\nu_2^* - 1 + \nu_2^*(\nu_2^* + 1)}{\nu_2^* - 1 + \nu_i^*(\nu_2^* + 1)}. \tag{4.29}$$

We can obtain a direct stacking ratio from the reservoir to the nanochannel by multiplying the expressions in eqns (4.29) and (4.26):

$$S_{i,n/r} = S_{0,n/r}\,\frac{2\nu_2^* - 1 + \nu_i^*\nu_2^*}{\nu_i^* + \nu_2^* - 1 + \nu_i^*\nu_2^*}. \tag{4.30}$$

We can also write the stacking ratio from the reservoir to the nanochannel without relating it to the BGE concentration as:

$$S_{i,n/r} = \frac{(2\nu_2^* - 1 + \nu_i^*\nu_2^*)\left(\nu_2^* + 1\right)}{c_{0,r}^*h_n^*\left[\nu_2^* - 1 + \nu_i^*\left(\nu_2^* + 1\right)\right]} \tag{4.31}$$

Next, we derive an expression for the stacking ratio from the nanochannel to the enrichment zone. In the enrichment zone the EDL contribution to the flux can be neglected and the total flux can be written as:

$$f_{i,e} = c_{i,e}\left(Q + \nu_i z_i F E_e h_e\right). \tag{4.32}$$

Equating this flux to the flux associated with the nanochannel leads to an expression for the stacking ratio from nanochannel to the enrichment zone:

$$S_{i,e/n}=\frac{\dfrac{1}{1+2/c_{0,n}^{*}h_{n}^{*}}+\nu_{i}^{*}}{1+\nu_{i}^{*}\dfrac{h_{e}^{*}(c_{0,n}^{*}h_{n}^{*}+1)}{h_{n}^{*}(c_{0,e}^{*}h_{e}^{*}+1)}}. \tag{4.33}$$

Here, we used eqn (4.7) to express the ratios of electromigration fluxes to the advective flux. From Mani *et al.*[30] the BGE concentration in the enrichment zone for this case is:

$$c_{0,e}^{*}h_{n}^{*}=2\nu_{2}^{*}-1. \tag{4.34}$$

Using this expression together with eqn (4.24) in eqn (4.33) and noting $c_{0,e}^{*}h_{e}^{*}\gg 1$ for typical microchannels leads to:

$$S_{i,e/n}=\left(\frac{2\nu_{2}^{*}-1}{\nu_{2}^{*}+1}\right)\frac{\nu_{2}^{*}-1+\nu_{i}^{*}(\nu_{2}^{*}+1)}{2\nu_{2}^{*}-1+\nu_{i}^{*}\nu_{2}^{*}}. \tag{4.35}$$

Rewriting eqn (4.35) in terms of the BGE stacking ratio leads to:

$$S_{i,e/n}=S_{0,e/n}\frac{\nu_{i}^{*}+\nu_{2}^{*}-1+\nu_{i}^{*}\nu_{2}^{*}}{2\nu_{2}^{*}-1+\nu_{i}^{*}\nu_{2}^{*}}. \tag{4.36}$$

By combining eqns (4.36) and (4.30) one can see:

$$S_{i,e/r}=S_{0,e/r}. \tag{4.37}$$

We can also write:

$$S_{i,e/r}=\frac{2\nu_{2}^{*}-1}{c_{0,r}^{*}h_{n}^{*}}. \tag{4.38}$$

Finally we show that the concentration of the analyte in the cathode-side *r* region is the same as that in the anode-side *r* region. Here, we will temporarily use subscript *rc* for the cathode-side microchannel to distinguish it from the anode-side zone. We consider a control volume moving with the enrichment front and write the flux balance equation between the two sides of the front. Mani *et al.*[30] and Zangle *et al.*[21] showed that the enrichment shock advects at the bulk velocity. Furthermore, EDL contribution to the flux terms is negligible on either sides of the enrichment shock. Therefore, the only term contributing to the flux through the control surfaces is the electromigration of the bulk concentration, henceforth the flux balance equation leads to:

$$S_{i,rc/e} = \frac{c_{i,rc}}{c_{i,e}} = \frac{\nu_i z_i F E_e h_e}{\nu_i z_i F E_{rc} h_{rc}} = \frac{E_e}{E_{rc}} = \frac{c_{0,rc}}{c_{0,e}} = S_{0,rc/e}\,. \tag{4.39}$$

Combining eqns (4.37) and (4.39) leads to:

$$S_{i,rc/r} = S_{0,rc/r} = 1\,. \tag{4.40}$$

The second equality is due to the fact that the anode-side reservoir has the same BGE concentration as in the cathode-side reservoir.

4.2.4 Propagating CP, $\nu_2^* < 1$

The procedure of solving the problem in this case is exactly the same as what we presented in section 4.2.3. The only difference is that the BGE concentrations are different in this case and the following values from solution by Mani *et al.*[30] should be substituted into the expressions:

$$c_{0,d}^* = c_{0,n}^* = 0, \;\; c_{0,e}^* h_n^* = \nu_2^*\,. \tag{4.41}$$

For this case the depletion region shock velocity is given by:[30]

$$\frac{V_{shock} h_r}{Q} = 1 - \frac{\nu_2^*}{c_{0,r}^* h_n^*} \tag{4.42}$$

In this case in regions *d* and *n* the only term contributing to the fluxes is the EDL transport and the bulk term is zero. We avoid repeating the algebraic procedures here and only present the results of the analysis.

$$S_{i,d/r} = \frac{\nu_i^* + \nu_2^*}{h_d^* c_{0,r}^* \nu_i^*} = S_{0,d/r}\,\frac{\nu_i^* + \nu_2^*}{2\nu_i^*}\,, \tag{4.43}$$

For the depletion region we obtain:

$$S_{i,n/d} = \frac{h_d}{h_n} = S_{0,n/d}\,, \tag{4.44}$$

and combining eqns (4.44) and (4.43):

$$S_{i,n/r} = \frac{\nu_i^* + \nu_2^*}{h_n^* c_{0,r}^* \nu_i^*}\,. \tag{4.45}$$

Finally, for the enrichment region

$$S_{i,e/n} = \frac{\nu_i^* \nu_2^*}{\nu_i^* + \nu_2^*} = S_{0,e/n}\,\frac{2\nu_i^*}{\nu_i^* + \nu_2^*}\,, \tag{4.46}$$

where, using equation (4.45), we obtain:

$$S_{i,e/r} = \frac{\nu_2^*}{h_n^* c_{0,r}^*} \tag{4.47}$$

In Figure 4.2 we provide the resulting relations from the analysis presented here. The results describe the area-averaged stacking ratio of a cationic analyte species, *i*, between each region of the microchannel-nanochannel system and the reservoir concentration. In typical fluorescence microscopy, the area averaged stacking ratio is directly related to the measured increase in fluorescence intensity inside the channel. Therefore, the stacking ratio is the experimentally accessible quantity. Stacking ratios in each region of the microchannel-nanochannel-microchannel system are given in terms of the key system parameters: channel height ratios, nondimensional mobilities, and Dukhin number, $1/c_{0,r}^{*}h_{n}^{*}$. These are typically all known quantities.

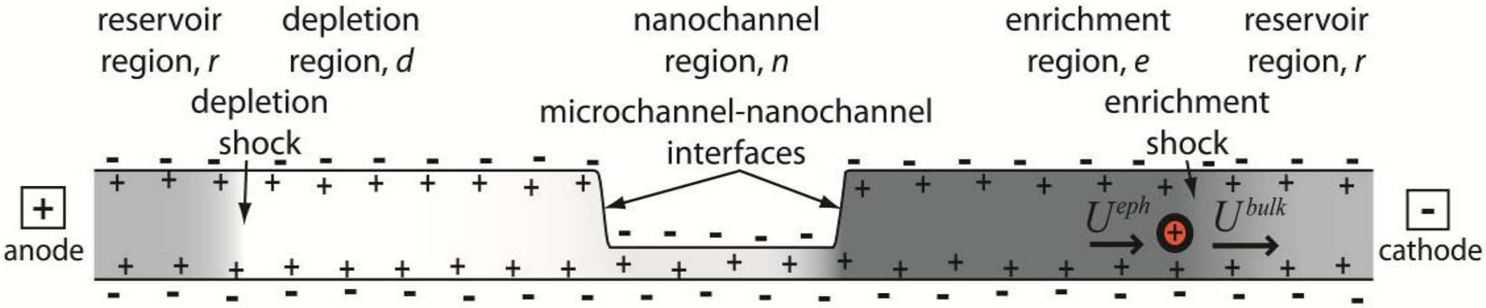
reservoir region, *r*
depletion region, *d*
nanochannel region, *n*
enrichment region, *e*
reservoir region, *r*
depletion shock
microchannel-nanochannel interfaces
enrichment shock
anode
cathode
U^{eph}
U^{bulk}

non-propagating CP	region *d* does not exist w/o propagation	$S_{i,n/r}=\frac{c_{0,r}^{*}h_{n}^{*}+\nu_{i}^{*}\left(c_{0,r}^{*}h_{n}^{*}-\nu_{2}^{*}+1\right)}{c_{0,r}^{*}h_{n}^{*}-\nu_{2}^{*}+\nu_{i}^{*}\left(c_{0,r}^{*}h_{n}^{*}-\nu_{2}^{*}+2\right)}\cdot\frac{c_{0,r}^{*}h_{n}^{*}-\nu_{2}^{*}+2}{c_{0,r}^{*}h_{n}^{*}}$	region *e* does not exist w/o propagation
propagating CP, $\nu_2^* < 1$	$S_{i,d/r}=\frac{\nu_{i}^{*}+\nu_{2}^{*}}{h_{d}^{*}c_{0,r}^{*}\nu_{i}^{*}}$	$S_{i,n/r}=\frac{\nu_{i}^{*}+\nu_{2}^{*}}{h_{n}^{*}c_{0,r}^{*}\nu_{i}^{*}}$	$S_{i,e/r}=\frac{\nu_{2}^{*}}{h_{n}^{*}c_{0,r}^{*}}$
propagating CP, $\nu_2^* \geq 1$	$S_{i,d/r}=\frac{\nu_{2}^{*}(2\nu_{2}^{*}-1+\nu_{i}^{*}\nu_{2}^{*})}{\nu_{i}^{*}(2\nu_{2}^{*}-1)c_{0,r}^{*}h_{d}^{*}}$	$S_{i,n/r}=\frac{(2\nu_{2}^{*}-1+\nu_{i}^{*}\nu_{2}^{*})\left(\nu_{2}^{*}+1\right)}{c_{0,r}^{*}h_{n}^{*}\left[\nu_{2}^{*}-1+\nu_{i}^{*}\left(\nu_{2}^{*}+1\right)\right]}$	$S_{i,e/r}=\frac{2\nu_{2}^{*}-1}{c_{0,r}^{*}h_{n}^{*}}$

Figure 4.2 Summary of results for area-averaged stacking ratios of cationic analytes. Results were derived by balancing cationic species flux across each of four labeled interfaces (depletion shock, microchannel-nanochannel interfaces, enrichment shock) in the system. Note that the depletion region stacking ratio, $S_{i,d/r}$, is inversely proportional to the microchannel height in the depletion region nondimensionalized by the nanoscale reference length, h_d^*. Since h_d^* is typically very large, the concentration of a cationic species will be very low in the depletion region. This makes cationic tracers suitable for tracking the boundary of the depletion region, as was observed by Pu *et al.*[31] and used in experiments by Kim *et al.*[32]

4.2.5 Comparison to results from literature

The results shown in Fig 5 indicate that a cation analyte may be used to trace the development of the enrichment and depletion fronts. In the depletion region (first column of equations in Fig 5), the local-to-reservoir cationic stacking ratio is inversely proportional to the nondimensional microchannel height, h_d^*. h_d^* is typically very large, therefore we expect the concentration of a cationic analyte to approach zero inside the depletion region. This is similar to the behavior of the depletion region background electrolyte concentration which also approaches zero, making cationic analytes suitable for tracking the extent of the depletion region. In the enrichment region, the cationic analyte stacking ratio (rightmost column of Figure 4.2), exactly matches the increase in the background electrolyte (eqns (1.7) and (1.8)). This makes a cationic tracer suitable as to both track the extent of and measure the concentration inside the enrichment region. Finally, the cationic stacking ratio inside the nanochannel is a function of both the analyte mobility, ν_i^*, and the BGE properties. Therefore, the cationic stacking ratio is not a simple measurement of the BGE concentration inside the nanochannel.

Pu *et al.*[31] examined the behavior of Rhodamine 6G in a Borofloat glass device with a 60 nm deep nanochannel. In these experiments an electric field was applied from right to left along a nanochannel oining two U-shaped microchannels. As predicted by the results in Figure 4.2, the concentration on the cathode side of the nanochannel (where we expect the enrichment region) increased and the concentration on the anode side decreased. Furthermore, their results showed that in the case where fluorescein is used as an analyte molecule an enriched region was formed at the nanochannel interface, then started to separate from it over time. In contrast their results show that the Rhodamine 6G enrichment region stays attached to the interface. This is consistent with the prediction that Rhodamine 6G, as a counter-ionic analyte, should trace the BGE enrichment region. Computational model results of background electrolyte behavior show that CP creates a net-neutral enrichment region which remains attached to the cathode-side interface.[21,28,33] The observed behavior of fluorescein in these experiments is consistent with simulation results for an anionic analyte[28,33] and will be discussed in more detail below.

As per Figure 4.2 the concentration of a counter-ionic dye will be very low in the depletion region, making it suitable for experiments to track the edge of the depletion region over time. Kim *et al.*[32] used Rhodamine 6G combined with fluorescent beads to image CP-induced vortices at the boundary of the depletion region.

Experiments by Huang and Yang[58] using Rhodamine 6G as a counter-ionic tracer showed similar results to those of Pu *et al.*[31] and also used a cationic dye to trace the extent of the depletion region. Additionally, Huang and Yang performed numerical simulations of the flow in the depletion region using a constant zeta potential model. This model found that recirculation occurs due to a change in the degree of EDL overlap inside the depletion region, which lowers the overall bulk velocity. They found that the pattern of the edge of the depletion front imaged using Rhodamine 6G correlated with their simulated recirculation flow profile.

Experiments with nanoporous glass beads imaged using Rhodamine 6G[78] showed a large decrease in concentration inside the beads and traced the formation of a strong enrichment zone on the cathode side of the bead. In similar experiments at a different set of condition, using normalized fluorescence intensity measurements inside a nanoporous glass bead, Tallarek *et al.*[48] visualized an increase in concentration inside the nanoporous structures as well as formation of enrichment and depletion zones. Again, to our best interpretation of the experiments, each of these results is consistent with Fig 5.

Kim *et al.*[20] performed experiments with Rhodamine 123 loaded into only one side of a nanochannel with strongly overlapped EDLs. They showed that Rhodamine 123 was able to translocate the nanochannel upon application of an electric field. This is expected for a counter-ion which will always move in the direction of the applied electric field, and so consistent with the theory presented here. Similar experiments performed with anionic fluorescent species showed that these ions were unable to pass through the nanochannel.

This behavior is also consistent with our theory and will be discussed in the next section describing behavior of anionic species.

4.3 Anionic species

In this section we consider the behavior of anionic analytes in a system with concentration polarization due to a nanochannel with negatively charged walls. Here we extend the results of preliminary work we have published on this topic[29] as well as the analysis of a recent paper by Plecis *et al.*[28] Plecis *et al.* identifies four focusing regimes for anionic analytes and presents a computational model which captures phase boundaries based on surface charge, σ, and applied potential. We here start in Section 4.3.1 by deriving results for the behavior of anionic species using the analytical theory of Mani et al.[30] Using an analytical model allows us to present a generalized regime map for arbitrary buffer and surface chemistry.

In sections 4.3.2-4.3.5, we compare both the analytical model based on Mani *et al.*[30] and the computational results of Plecis *et al.*[28] to published experimental results across a wide variety of conditions. We address separately each interface in a microchannel-nanochannel system with concentration polarization. Starting from the left side of Figure 4.3 we will look at anionic analyte behavior on the depletion shock (section 4.3.2), the depletion region side microchannel-nanochannel interface (section 4.3.3), the enrichment region side nanochannel-microchannel interface (section 4.3.4) and, finally, the enrichment shock (section 4.3.5)

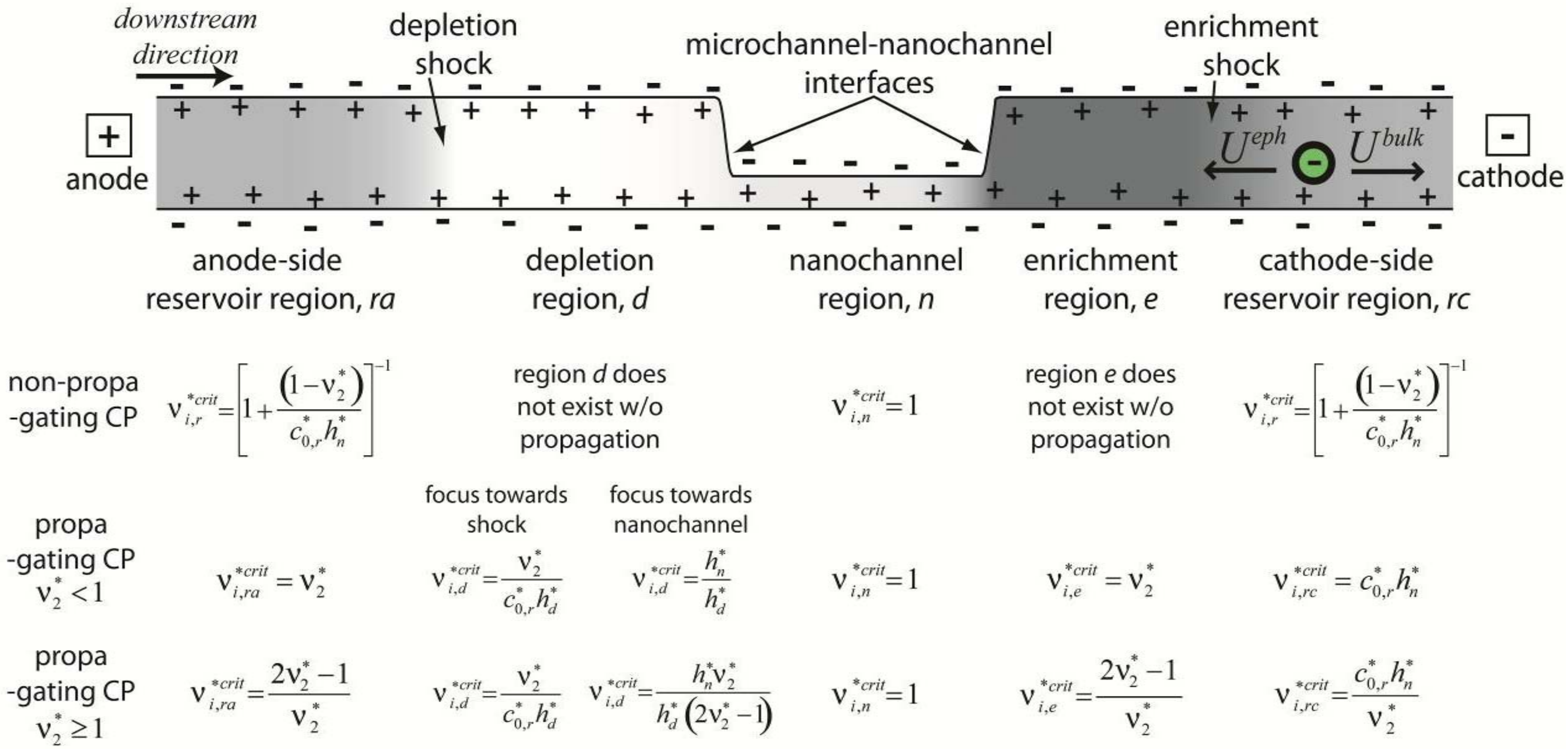
downstream direction
depletion shock
microchannel-nanochannel interfaces
enrichment shock
+
anode
-
cathode
U^{eph}
U^{bulk}
anode-side reservoir region, *ra*
depletion region, *d*
nanochannel region, *n*
enrichment region, *e*
cathode-side reservoir region, *rc*
non-propagating CP
$\nu_{i,r}^{*crit} = \left[1 + \frac{(1-\nu_2^*)}{c_{0,r}^* h_n^*}\right]^{-1}$
region *d* does not exist w/o propagation
$\nu_{i,n}^{*crit} = 1$
region *e* does not exist w/o propagation
$\nu_{i,r}^{*crit} = \left[1 + \frac{(1-\nu_2^*)}{c_{0,r}^* h_n^*}\right]^{-1}$
focus towards shock
focus towards nanochannel
propagating CP $\nu_2^* < 1$
$\nu_{i,ra}^{*crit} = \nu_2^*$
$\nu_{i,d}^{*crit} = \frac{\nu_2^*}{c_{0,r}^* h_d^*}$
$\nu_{i,d}^{*crit} = \frac{h_n^*}{h_d^*}$
$\nu_{i,n}^{*crit} = 1$
$\nu_{i,e}^{*crit} = \nu_2^*$
$\nu_{i,rc}^{*crit} = c_{0,r}^* h_n^*$
propagating CP $\nu_2^* \geq 1$
$\nu_{i,ra}^{*crit} = \frac{2\nu_2^* - 1}{\nu_2^*}$
$\nu_{i,d}^{*crit} = \frac{\nu_2^*}{c_{0,r}^* h_d^*}$
$\nu_{i,d}^{*crit} = \frac{h_n^* \nu_2^*}{h_d^* (2\nu_2^* - 1)}$
$\nu_{i,n}^{*crit} = 1$
$\nu_{i,e}^{*crit} = \frac{2\nu_2^* - 1}{\nu_2^*}$
$\nu_{i,rc}^{*crit} = \frac{c_{0,r}^* h_n^*}{\nu_2^*}$

Figure 4.3 Summary of results for critical values of ν_i^* for anionic analytes. For a given channel location and CP behavior (non-propagating, propagating $\nu_2^* < 1$, propagating $\nu_2^* \geq 1$) if ν_i^* is greater than ν_i^{*crit} then the ion will electromigrate upstream towards the anode, if ν_i^* is less than ν_i^{*crit} then species *i* will advect downstream towards the cathode. The downstream direction (direction of bulk flow) and all four interfaces discussed in the text (depletion shock, microchannel-nanochannel interfaces, enrichment shock) are labeled in the microchannel-nanochannel schematic at the top of the figure.

4.3.1 Analytical predictions

To predict analyte behavior, we will look at the direction of transport of analyte anions in each region of the micro-nanochannel system relative to each interface in the system. As noted earlier, there are only four possible interfaces in a microchannel-nanochannel system with CP at which the total species drift velocity, $U_i^{tot} = U_i^{eph} + U^{bulk} - V^{\text{int}}$, changes. As shown in Figure 4.3 these are the depletion shock, the microchannel-nanochannel interfaces and the enrichment shock. In this section to predict focusing versus stacking, we will examine U_i^{tot} at each of these interfaces. Unlike cations, anions can, in the frame of reference of an interface moving at V^{int}, migrate in opposite directions into a common focusing zone; so that U_i^{tot} changes sign on either side of the interface.*

The interfaces created by the junctions of the microchannels and nanochannel have zero velocity, so that $V^{\text{int}} = 0$. Since, for a negatively charged channel system, anions electromigrate in the opposite direction of bulk flow, we will examine the ratio of the local electrophoretic velocity of the co-ionic species divided by the local bulk velocity, U_i^{eph} / U^{bulk}. Each of these velocities is here measured relative to the laboratory frame. If $U_i^{eph} / U^{bulk} > 1$, then the local electrophoretic velocity is higher than the local bulk velocity and the anionic species electromigrates upstream, against the direction of bulk flow. When $U_i^{eph} / U^{bulk} < 1$, the anionic species advects downstream in the direction of bulk flow. The ratio U_i^{eph} / U^{bulk} in each region of the system, therefore, defines the critical value of the anion mobility, ν_i^{*crit}, at which the anion's total velocity changes sign. We can then compare the nondimensional analyte anion mobility, ν_i^*, which is assumed to be constant and uniform throughout a given system, to the computed values of ν_i^{*crit} in each region. If the analyte anion mobility, ν_i^*, is greater than the critical value, ν_i^{*crit}, downstream of a particular interface, and less than the critical value upstream of the same interface, then that analyte anion will be transported inwards towards that interface and will focus. We examine this condition in more detail in sections 4.3.3 and 4.3.4.

---

* The enrichment shock is the only interface in such a system where V^{int} is positive and nonzero. However, Mani *et al.*[30] and Zangle *et al.*[21] showed that this interface travels at the bulk velocity. Therefore, the total species velocity on either side of this interface will be U_i^{eph} which has the same sign on either side of the enrichment shock.

At the enrichment region shock, $V^{\text{int}} = U^{bulk}$.[21,30] Therefore, analyte anions can never focus at this interface (since U_i^{eph} cannot change sign). Experimental observations do show stacking at the enrichment shock, accompanied by a decrease in concentration in the near-nanachannel region[29,33,56]. This type of stacking is captured by the theory as regions where the critical mobility, ν_i^{*crit}, on the anode side of the enrichment shock is lower than ν_i^*, which is in turn lower than ν_i^{*crit} on the cathode side. We examine this condition in more detail in section 4.3.5.

At the depletion region shock V^{int} is a known function of the background electrolyte and channel properties.[30] Below, we derive results for the critical nondimensional analyte mobilities, ν_i^{*crit}, at which ions will focus on the moving depletion shock. We examine focusing on the depletion shock in more detail in section 4.3.2.

As a preliminary note, ν_i^* is defined as the ratio of the analyte electrophoretic velocity to the bulk (electroosmotic) velocity inside the nanochannel ($\nu_i^* = (\nu_i z_i F \eta)/(\zeta_n \varepsilon)$). Therefore, inside the nanochannel, $U_{i,n}^{eph} / U_n^{bulk} = \nu_i^*$ by definition, and for all conditions:

$$\nu_{i,n}^{*crit} = 1 . \tag{4.48}$$

Eqn (4.48) means that for $\nu_i^* > 1$ ions of species *i* will be fast enough to travel upstream inside the nanochannel, and for $\nu_i^* < 1$, ions of species *i* will be too slow to beat bulk flow and so will advect downstream through the nanochannel. In other zones of the channel system (e.g. the enrichment zone) the critical nondimensional mobility is not necessarily unity because the background electrolyte concentration and the electric field vary locally due to CP. For these zones the theory of Mani *et al.* [30] can be employed to predict the relative strength of the electrophoretic to bulk velocities in each region of the micro-nanochannel system. Equating this ratio to unity yields the critical mobility in each zone in terms of system key parameters (channel height ratios, Dukhin number, and nondimensional mobility of the co-in in the BGE). We present the derivation of critical mobilities in the following sections and present the results of critical mobilities in each zone in Figure 4.3.

It should be noted that the analysis of anion transport is less complex compared to that for cations since anions are mostly transported through the bulk and have a relatively low concentration in the EDLs. Therefore, for the purposes of this analysis, we will assume that an anionic analyte, *i*, is transported due to electromigration in the bulk in one direction and advection due to bulk flow in the opposite direction. The ratio of the electromigration velocity to the bulk flow velocity is, therefore:

$$\frac{U_i^{eph}}{U^{bulk}} = \frac{\nu_i z_i F E h}{Q} . \tag{4.49}$$

In section 4.2.1 we derived an expression for this ratio in the nondimensional form. Using eqn (4.7) in eqn (4.49) we have:

$$\left| \frac{U_i^{eph}}{U^{bulk}} \right| = \nu_i^* \frac{h^*(c_{0,n}^* h_n^* + 1)}{h_n^*(c_0^* h^* + 1)} , \tag{4.50}$$

where ν_i^* is nondimensionalized such that it is always positive ($\nu_i^* = \left| \nu_i z_i F \mu / \varepsilon \zeta_n \right|$). At either side of a stationary interface in the channel system, the critical analyte mobility can be computed by equating the right-had-side of eqn (4.50) to one:

$$\nu_i^{*crit} = \frac{h_n^*(c_0^* h^* + 1)}{h^*(c_{0,n}^* h_n^* + 1)} . \tag{4.51}$$

As discussed earlier, focusing will occur at a moving interface when the total species velocity in a frame moving with the interface, $U_i^{eph} + U^{bulk} - V^{\text{int}}$, changes sign. Therefore, at a moving interface, the critical analyte mobility can be computed by equating the right hand side of eqn (4.50) to one minus the interface velocity normalized by the bulk velocity:

$$v_i^{*crit} = \left(1 - \frac{V^{\text{int}}}{U^{bulk}}\right) \frac{h_n^*(c_0^* h^* + 1)}{h^*(c_{0,n}^* h_n^* + 1)}. \tag{4.52}$$

Note, however, that the enrichment shock velocity is equal to the bulk velocity[21,30] so at this interface analyte anions can never focus (on both sides of this interface, $v_i^* > v_i^{*crit}$, and so the analyte anion total velocty can never change sign). However, experimental observations have observed that, under some conditions anionic species can be transported inwards towards the enrichment shock in the lab frame.[28-29,33,56] Therefore, on either side of the enrichment shock we will look at the total species velocity in the lab frame and define v_i^{*crit} using eqn (4.51).

For different CP regimes, Mani *et al.*[30] derived expressions for concentration in the five zones of the channel system. In the following sections we substitute these expressions into eqn (4.51) and (4.52) and obtain closed form expressions for critical mobility in terms of known system parameters.

4.3.1.1 Non-propagating CP

For this case the channel system experiences three zones at equilibrium. The microchannels would have the same BGE concentration as in the supplying reservoir and the nanochannel would have a lower BGE concentration given by eqn (4.8). The only interfaces at which focusing is possible will be the two microchannel-nanochannel interfaces. Substituting eqn (4.8) into eqn (4.51) and noting $c_{0,r}^* h_r^* \gg 1$ (microchannel has low Dukhin number) leads to the following expressions for the critical mobility at different channel zones:

$$v_{i,r}^{*crit} = \left[1 + \frac{\left(1 - v_2^*\right)}{c_{0,r}^* h_n^*}\right]^{-1}, \quad v_{i,n}^{*crit} = 1. \tag{4.53}$$

Note that for non-propagating CP there are no enrichment or depletion shocks, therefore, we do not distinguish between anode and cathode side reservoir regions when discussing possible focusing.

4.3.1.2 Propagating CP, $\nu_2^* \geq 1$

For this case the BGE concentrations are given in eqns (4.24) and (4.34). For the microchannel-nanochannel interfaces and the enrichment shock we can substitute these results into eqn (4.51) which yields:

$$\nu_{i,rc}^{*crit} = \frac{c_{0,r}^* h_n^*}{\nu_2^*}, \quad \nu_{i,d}^{*crit} = \frac{h_n^*}{h_d^*} \frac{\nu_2^*}{2\nu_2^* - 1}, \quad \nu_{i,n}^{*crit} = 1, \quad \nu_{i,e}^{*crit} = \frac{2\nu_2^* - 1}{\nu_2^*}. \qquad (4.54)$$

For the depletion shock, we can substitute eqns(4.20) and (4.24) into eqn (4.52) to yield:

$$\nu_{i,ra}^{*crit} = \frac{2\nu_2^* - 1}{\nu_2^*}, \quad \nu_{i,d}^{*crit} = \frac{\nu_2^*}{c_{0,r}^* h_d^*}. \qquad (4.55)$$

4.3.1.3 Propagating CP, $\nu_2^* < 1$

For this case the BGE concentrations are given in eqn (4.41). For the microchannel-nanochannel interfaces and enrichment shock, we can substite these into eqn (4.51) resulting in:

$$\nu_{i,rc}^{*crit} = c_{0,r}^* h_n^*, \quad \nu_{i,d}^{*crit} = \frac{h_n^*}{h_d^*}, \quad \nu_{i,n}^{*crit} = 1, \quad \nu_{i,e}^{*crit} = \nu_2^*. \qquad (4.56)$$

For the depletion shock, we can substitute eqns(4.41) and (4.42) into eqn (4.52) to yield:

$$\nu_{i,ra}^{*crit} = \nu_2^*, \quad \nu_{i,d}^{*crit} = \frac{\nu_2^*}{c_{0,r}^* h_d^*}. \qquad (4.57)$$

4.3.1.4 Summary of Analytical Results

The results from sections 4.3.1.1-4.3.1.3 are presented in Figure 4.3. We again stress that the changes in ν_i^{*crit} across each of the four interfaces in Figure 4.3 indicate the existence and degree of a stacking or focusing situation due to local changes in electric fields and bulk flow velocities. For example, a decrease in the magnitude of ν_i^{*crit} from region *e* to *r* indicates slowing of anions as they move across the enrichment shock.[†] This change of velocity is due to a change in electric field which, in turn, is caused by the concentration difference across this interface. (Note that since fluid mass is conserved, the bulk flow velocities on either side of the enrichment (or depletion) region shock in a constant area microchannel are the same, so a change in ν_i^{*crit} reflects a change in local electric field.) This can lead to the case where an ion is transported downstream in one region relative to an interface (where $\nu_i^* < \nu_i^{*crit}$), and upstream in the next region relative to an interface (where $\nu_i^* > \nu_i^{*crit}$), hence focusing or stacking at the interface. Figure 4.3 is therefore a general framework for predicting both stacking and focusing behavior in these systems.

[†] First, consider an analyte species with $\nu_{i,n}^*$ greater than both values of ν_i^{*crit}. Such an ion moves quickly upstream toward the interface, as ν_i^{*crit} is low in the downstream region. When this species crosses into the upstream region, it slows down, since its ν_i^* is now closer to the local ν_i^{*crit} (at $\nu_i^* = \nu_i^{*crit}$ the total species velocity would be zero). This change in total velocity from a high to low value will cause local

The results for critical values of ν_i^* are plotted in Figure 4.4. Note that the critical value of ν_i^* in the depletion region (region *d*) relative to either the depletion shock or the microchannel-nanochannel interface depends on the nondimensional depletion region height, h_d^*. Over the domain of $c_{0,r}^* h_n^*$ and ν_2^* represented in Figure 4.4 and for the minimum reported value of h_1/h_n of 20,[21] $\nu_{i,d}^{*crit} \leq$ 0.05. This critical value is lower than any computed ν_i^* based on the literature surveyed here. In practice, this means that the electric field in the depletion region is high enough that all reported anionic species travel upstream faster than the depletion shock, with both $U_i^{eph}/U^{bulk} > 1$ and $U_i^{eph}/U^{bulk} > 1 - V^{shock}/U^{bulk}$, and, therefore, we do not plot values of $\nu_{i,d}^{*crit}$ in Figure 4.4.

---

stacking, but not focusing. Similarly, an ion advecting downstream with ν_i^* less than both values of ν_i^{*crit} will also change from high velocity to low velocity when $\nu_{i,upstream}^{*crit} > \nu_{i,downstream}^{*crit}$. Therefore, a species with very low ν_i^* will also stack under these conditions.

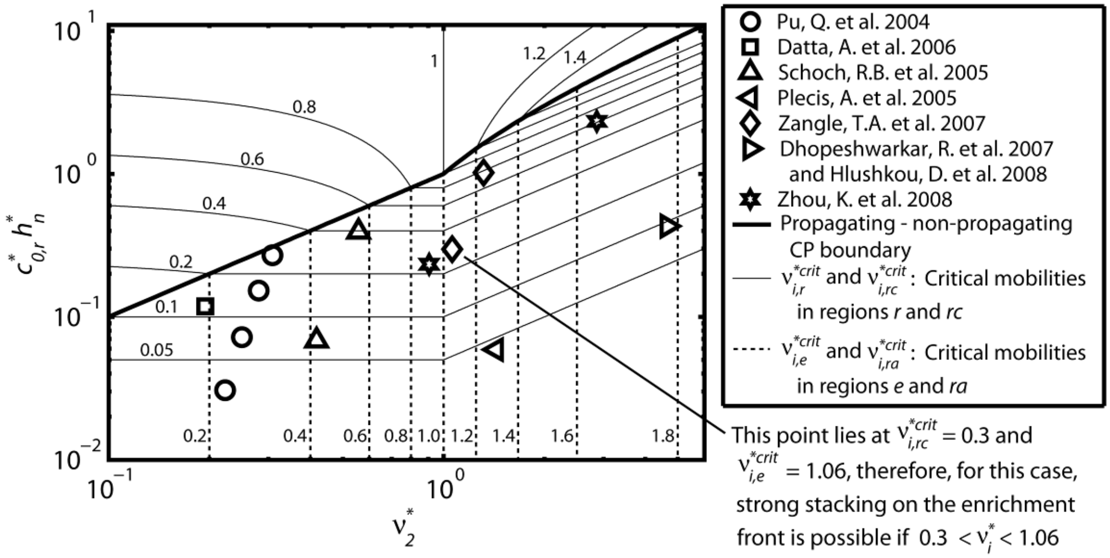

This point lies at $\nu^{*crit}_{i,rc} = 0.3$ and $\nu^{*crit}_{i,e} = 1.06$, therefore, for this case, strong stacking on the enrichment front is possible if $0.3 < \nu^*_i < 1.06$

Figure 4.4 Phase boundaries in the field defined by $c^*_{0,r}h^*_n$ versus ν^*_2. $c^*_{0,r}h^*_n$ describes the ratio of bulk conductance to surface conductance. ν^*_2 describes the ratio of background electrolyte (cation) mobility to the electroosmotic mobility in the nanochannel. The dashed contours are critical values of the nondimensional mobility of negatively charged analyte species in the enrichment region ($\nu^{*crit}_{i,e}$) or in the anode side reservoir region $\nu^{*crit}_{i,a}$. If, for example, the nondimensional analyte mobility (ν^*_i) is greater than the local $\nu^{*crit}_{i,e}$, then the analyte will electromigrate upstream in the enrichment region. The solid line contours are critical values of analyte mobility in the reservoir regions ($\nu^{*crit}_{i,r}$) for cases with no propagation, or contours of critical analyte mobility in the cathode side reservoir region ($\nu^{*crit}_{i,rc}$) for cases where CP propagates. These contours yield the mobility of an analyte which has zero total velocity in the reservoir region as a function of $c^*_{0,r}h^*_n$ and ν^*_2. The thick black line is the predicted phase boundary between propagating and non-propagating CP from the analytical theory of Mani *et al.*[30] Stacking and focusing predictions are discussed in the text below. Shown together with the theory are data from 8 studies. The predicted and observed focusing behaviors for each condition are discussed in the text and Table 4.1. Most of the results map as expected within our theoretical framework one exception is the experiments of Schoch *et al.*[53] where

enrichment side interface focusing was reported, but we predict stacking on the enrichment side interface.

Table 4.1 Predicted and Observed Analyte Ion Behaviors. The parameters $c_{0,r}^{*}h_{n}^{*}$, ν_{2}^{*} and ν_{i}^{*} are estimated based on literature data for zeta potential[60-61] and mobility.[5,87-89]

Reference	$c_{0,r}^{*}h_{n}^{*}$	ν_{2}^{*}	ν_{i}^{*}	Predicted behavior	Observed behavior
Pu, Q. *et al.* 2004[31]	0.03	0.22	0.37	Enrichment-side interface focusing	Enrichment-side interface focusing or enrichment shock stacking
	0.07	0.25	0.42		
	0.15	0.28	0.47		
	0.27	0.31	0.52		
Datta, A. *et al.* 2006[54]	0.12	0.19	0.33	Enrichment-side interface focusing	Enrichment-side interface focusing
Schoch, R.B. *et al.* 2005[53]	0.07	0.42	0.12	Enrichment side interface stacking	Enrichment-side interface focusing
	0.39	0.56	0.16		
Plecis, A. *et al.* 2005[52]	0.06	1.43	0.72	Enrichment-side interface focusing	Enrichment-side interface focusing
Zangle, T.A. *et al.* 2007[29]	0.30	1.06	0.34	Enrichment shock stacking and depletion shock focusing	Enrichment shock stacking and depletion shock focusing
	0.30	1.06	0.58		
	1.02	1.32	0.79		
Dhopeshwarkar, R. *et al.* 2008[33]	0.43	4.66	1.77	Enrichment shock stacking	Enrichment shock stacking
	0.43	4.66	2.33	No stacking	
Hlushkou, D. *et al.* 2008[56]	0.43	4.66	0.59	Enrichment shock stacking	Enrichment shock stacking
Zhou, K. *et al.* 2008[17]	0.23	0.91	0.72	Depletion shock focusing	Depletion shock stacking/focusing
	2.33	2.87	1.43		

We illustrate the utility of Figure 4.4 by considering an example case: a data point from Zangle *et al.*[29] at $c_{0,r}^{*}h_{n}^{*}$ = 0.3 and $\nu_{2}^{*} = 1.06$: In this case, experiment conditions (including the specific background electrolyte or buffer used) determine $c_{0,r}^{*}h_{n}^{*}$ and ν_{2}^{*}. We plot this point at these coordinates as shown in Figure 4.4. Since the point is below the thick solid line, then the model predicts propagating CP with large enrichment and depletion regions (a point above the line indicates non-propagating CP). We then either compute $\nu_{i,e}^{*crit}$, $\nu_{i,rc}^{*crit}$ and $\nu_{i,ra}^{*crit}$ from the results in Figure 4.3 or read their values from the $\nu_{i,e}^{*crit}$, $\nu_{i,rc}^{*crit}$ and $\nu_{i,ra}^{*crit}$ contours of Figure 4.4 to establish stacking or focusing situations. Keep in mind that the critical value of ν_i^* in the nanochannel is unity, and the critical value of ν_i^* in the depletion region is typically lower than ν_i^* for most analytes. In this example, $\nu_{i,e}^{*crit}$ = 1.06, $\nu_{i,rc}^{*crit}$ = 0.3 and $\nu_{i,ra}^{*crit}$ = 1.06. Next, we compute the analyte nondimensional mobility ν_i^*. In this case, we found ν_i^* = 0.34 for one of the analytes studied (see Table 4.1). Finally, stacking or focusing is possible only if the analyte slows down as it moves through an interface. Therefore, we identify interfaces where the critical analyte mobility is higher upstream than downstream (downstream direction defined as the direction of bulk flow in the system). In this example $\nu_{i,ra}^{*crit} > \nu_{i,d}^{*crit}$ and $\nu_{i,e}^{*crit} > \nu_{i,rc}^{*crit}$, so we predict an increase in analyte concentration at both the depletion and enrichment shocks. Next, we look at how the value of ν_i^* for our analyte of interest compares to the critical values in the system. In this case $\nu_i^* < \nu_{i,e}^{*crit}$ and $\nu_i^* >$ $\nu_{i,rc}^{*crit}$, therefore, this analyte is expected to stack strongly on the enrichment shock. This matches well with the experimental observation of strong enrichment shock stacking. This procedure was carried out for each of the experimental conditions in Figure 4.4. The results of this analysis are summarized in Table 4.1 and the sections below. Figure 4.5 shows a graphically worked out example of anionic analyte behavior.

In the following sections, we will consider possible focusing and stacking criteria at each interface shown in Figure 4.3. We will also compare the model presented here (based in part on Mani *et al.*[30]) to published experimental results. This comparison is summarized in Table 4.1.

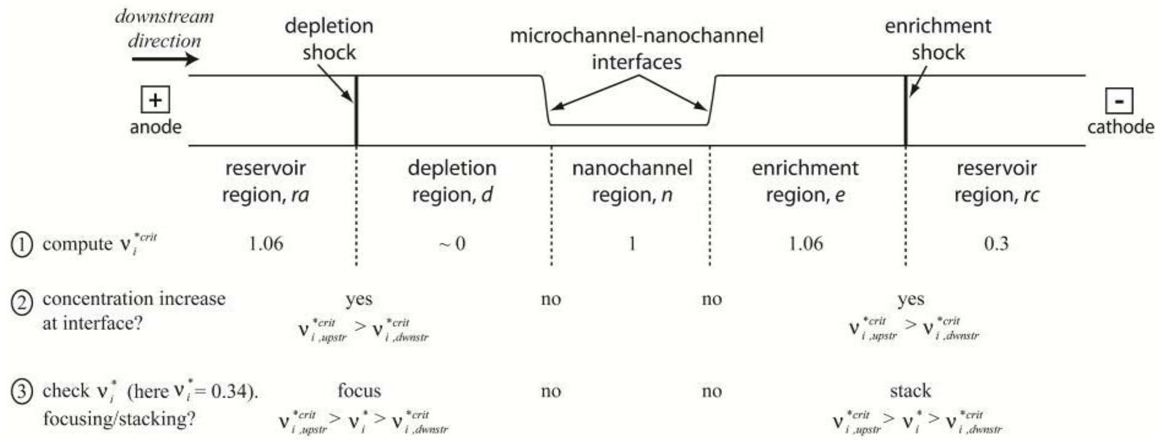
downstream direction
depletion shock
microchannel-nanochannel interfaces
enrichment shock
+
anode
-
cathode
reservoir region, ra
depletion region, d
nanochannel region, n
enrichment region, e
reservoir region, rc
① compute ν_i^{*crit}
1.06
~0
1
1.06
0.3
② concentration increase at interface?
yes
$\nu_{i,upstr}^{*crit} > \nu_{i,dwnstr}^{*crit}$
no
no
yes
$\nu_{i,upstr}^{*crit} > \nu_{i,dwnstr}^{*crit}$
③ check ν_i^* (here $\nu_i^* = 0.34$). focusing/stacking?
focus
$\nu_{i,upstr}^{*crit} > \nu_i^* > \nu_{i,dwnstr}^{*crit}$
no
no
stack
$\nu_{i,upstr}^{*crit} > \nu_i^* > \nu_{i,dwnstr}^{*crit}$

Figure 4.5 Worked example of predictions for anionic analyte behavior. Step 1: Compute ν_i^{*crit} for each region (reservoir, depletion, nanochannel and enrichment if propagating CP, reservoir and nanochannel if non-propagating CP) in the system. Note that ν_i^{*crit} in the depletion region is lower than ν_i^* (indicated by ~0 in the above figure) for most practical analytes and that ν_i^{*crit} in the nanochannel is unity by definition. ν_i^{*crit} in the reservoir and enrichment regions depends only on the background electrolyte and channel properties. Step 2: Check for interfaces where concentration can increase by looking for higher ν_i^{*crit} upstream (*upstr*) than downstream (*dwnstr*). If $\nu_{i,upstr}^{*crit} > \nu_{i,dwnstr}^{*crit}$ then anionic analytes will slow as they pass through the interface, resulting in an increase in concentration. Step 3: Check the value of ν_i^* for the analyte being considered. If $\nu_{i,upstr}^{*crit} > \nu_i^* > \nu_{i,dwnstr}^{*crit}$ then the analyte will stack or focus at the interface in question. As per the discussion in sections 4.3.1-4.3.5 anionic analytes can focus at the depletion shock or either microchannel-nanochannel interface. However, anionic analytes can only ever stack at the enrichment shock.

4.3.2 Depletion shock

When CP propagates, focusing of analytes at the depletion shock occurs when the analyte mobility is low enough that analytes travel in the direction of bulk flow inside the reservoir region but high enough that they travel against bulk flow in the depletion region. This condition can be written as: $\nu_{i,d}^{*crit} < \nu_i^* < \nu_{i,ra}^{*crit}$. For all reported cases of ν_i^*

from the literature, $v_{i,d}^{*crit} < v_i^*$. This is because the concentration in the depletion region is very low, therefore, the electric field is very high. The high electric field in the depletion region causes all analytes to have a very high electrophoretic velocity here. Therefore, for all practical anions we know of in systems with typical microchannel heights ($c_{o,r}^* h_d^* \gg 1$), analyte ions will move upstream inside the depletion region (against the direction of bulk flow) faster than the depletion region shock velocity. Plecis *et al.*[28] termed this regime anode cathode gradient focusing (ACGF).

Analytes which do not meet the focusing condition can still stack on the depletion shock as long as $v_{i,d}^{*crit} < v_{i,ra}^{*crit}$. For all CP cases examined here, this condition is met, and stacking at the depletion shock interface should occur. Physically, this condition means that anionic analyte ions traveling towards the depletion shock through the depletion region will slow down once they reach the shock, causing an increase in concentration.

The depletion shock is a strong shock[30] and, therefore, has large changes in concentration over very short distances. These large concentration gradients in the background electrolyte create high electric field gradients. These field gradients, in turn, are very suitable for focusing of analytes to very high concentrations. As already discussed, many applications of CP focus analytes on a depletion shock.[16,20,22,24,67-68]

In experiments with the same buffer and channel conditions as Zangle *et al.*[29] we noted focusing on the depletion shock, as predicted by theory (see Figure 4.6(b)). Zhou *et al.*[17] also noted focusing on the depletion shock, as expected by theory.

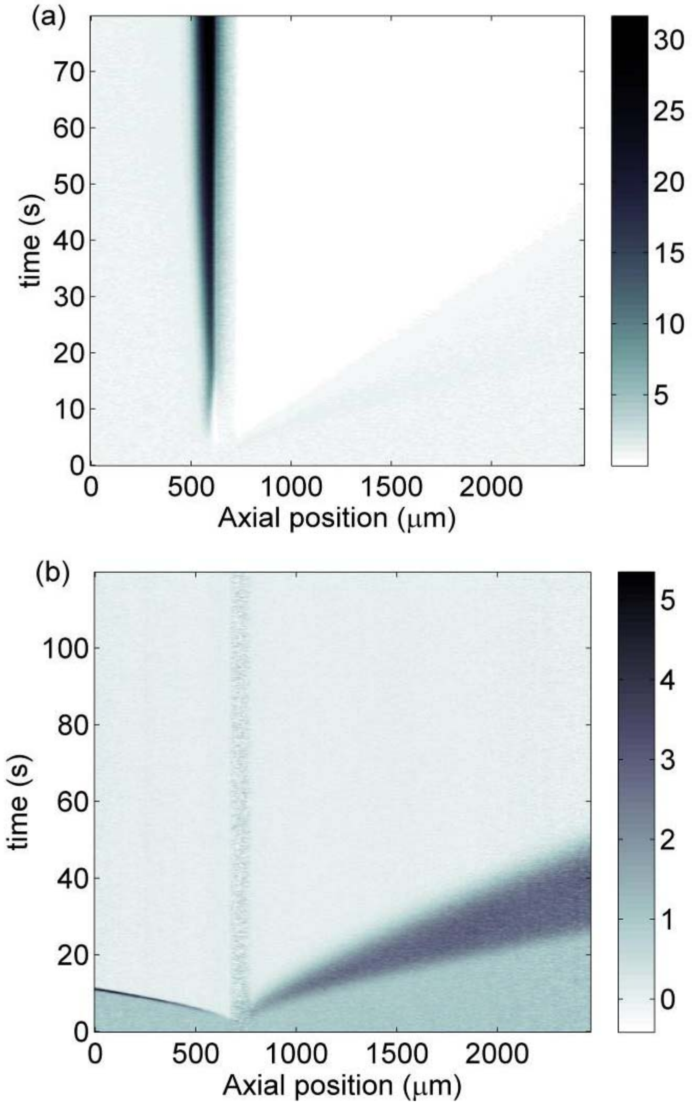

Figure 4.6 Experiments showing (a) non-propagating CP with focusing on the depletion side nanochannel and (b) propagating CP with focusing on the depletion shock and stacking on the enrichment shock. Experiments were performed using a 50 nm deep nanochannel and 1 μm deep microchannel as in Figure 2.2. In these images, the nanochannel is visible from approximately x = 600 μm to x = 700 μm. Before application of 2 nA constant current, the channels were filled by pressure with a solution containing (a) 10 mM Tris-HCl, 100 μM Alexa Fluor 488 and (b) 2.5 mM Tris-HCl, 50 μM Alexa Fluor 488. These results are consistent with the analytical predictions presented in section 4.3.1. Colormap shows measured change in fluorescence intensity relative to the initial value.

4.3.3 Depletion Side Microchannel-Nanochannel Interface

In the previous section we showed that anions can focus on the moving boundary of the depletion shock. Next, we will examine possible anion behaviors at the depletion-side microchannel-nanochannel interface. According to the theory presented in Figure 4.3 and Figure 4.4, focusing or stacking at the depletion side microchannel-nanochannel interface should not be possible if CP propagates. This is because the concentration in the depletion region is very low, therefore the electric field is very high, and co-ionic species travel very quickly upstream in this region. This corresponds to very low values of $\nu_{i,d}^{*crit}$ in the analytical theory outlined above. This focusing or stacking location corresponds to the anode stacking (AS) regime of Plecis *et al.*[28]

As indicated schematically in Figure 4.1, in cases where CP does not propagate, focusing or stacking is possible at this interface if $\nu_{i,n}^{*crit} < \nu_{i,r}^{*crit}$. Focusing will occur if $\nu_{i,n}^{*crit} < \nu_i^* < \nu_{i,r}^{*crit}$. Stacking will occur if $\nu_{i,n}^{*crit} < \nu_{i,r}^{*crit}$ and ν_i^* is either larger or smaller than the critical mobilities in the nanochannel and the reservoir.

A conference paper by Plecis *et al.*[55] presents visualizations of depletion side preconcentration of an analyte. The channel layout consisted of a very wide microchannel connected to a much narrower nanochannel. The visualizations show an increase in fluorescence intensity very close to the depletion side nanochannel interface (in contrast to the model described here which predicts stacking on the depletion shock). We hypothesize that their geometry (which is difficult to analyze with our model) may result in a propagating CP case where stacking of the analyte appears to be very similar to focusing on the depletion side interface. To the best of our knowledge, focusing or stacking at the depletion side interface for propagating CP has not been demonstrated experimentally in a device with constant (in-plane) width channels.

Figure 4.6(a) shows an experiment with non-propagating CP where Alexa Fluor 488 focuses on the depletion side nanochannel interface, as predicted by theory.

4.3.4 Enrichment Side Microchannel-Nanochannel Interface

In this section we consider the enrichment side microchannel-nanochannel interface. The analysis above shows that focusing or stacking can occur at this interface with either propagating or non-propagating CP. We are not aware of any observations of an increase in analyte concentration at the enrichment side nanochannel interface in non-propagating CP. Plecis *et al.*[28] termed focusing or stacking at the enrichment side nanochannel interface as cathode stacking (CS).

When CP propagates, an analyte species focuses on the enrichment side nanochannel interface if its mobility is too low to travel against bulk flow inside the nanochannel, but high enough to travel against bulk flow in the enrichment region. This condition can be written as: $\nu_{i,e}^{*crit} < \nu_i^* < \nu_{i,n}^{*crit}$, or, since the critical analyte nondimensional mobility inside the nanochannel is always unity, we can write the condition for focusing on the enrichment side nanochannel interface as

$$\nu_{i,e}^{*crit} < \nu_i^* < 1. \qquad (4.58)$$

For non-propagating CP there is no appreciable length enrichment region (any increase in background electrolyte concentration due to CP will be very localized). Therefore, we only need to consider the behavior of anions in the reservoir region. The condition for focusing at the enrichment side nanochannel interface for non-propagating CP is

$$\nu_{i,r}^{*crit} < \nu_i^* < 1. \qquad (4.59)$$

Finally, for propagating CP, stacking is possible at this interface if analyte ions have a higher electrophoretic velocity in the enrichment region than in the nanochannel. Therefore the stacking condition is

$$\nu_{i,e}^{*crit} < 1. \qquad (4.60)$$

The stacking condition for non-propagating CP is

$$\nu_{i,r}^{*crit} < 1. \qquad (4.61)$$

Pu *et al.*[31] show behavior consistent with either focusing at the enrichment side nanochannel interface or stacking at an enrichment shock. The ambiguity is because, in the last time-series images reported, the regions of increased analyte concentration appear to be moving slightly away from the microchannel-nanochannel interface, though they have not propagated very far. For all reported experimental cases our model predicts focusing at the enrichment side interface. Better comparison to experiments would require longer time series data. In related work, Datta *et al.*[54] show results consistent with focusing on the enrichment side nanochannel interface and in agreement with our model.

Schoch, *et al.*[53] also report focusing at the enrichment side nanochannel interface, however, for their reported conditions, our model predicts either stacking on the enrichment side nanochannel interface or stacking on a propagating enrichment shock. This discrepancy may be due to the low applied potential in this experiment (10 V or less). A low applied electric field (and low Peclet number) may prevent the enrichment shock from propagating far enough to overcome diffusion in the vicinity of the pore. Another possible reason for this discrepancy may be our uncertainty in the mobility of GFP (we roughly estimated its mobility as $1\text{x}10^{-9}$ m^2/V-s[89]). We also note that this Schoch paper discusses an increase of fluorescence concentration over time at a higher ionic strength. At this higher ionic strength, our model also predicts stacking at the enrichment side interface.

4.3.5 Enrichment Shock

Here, we consider the final interface shown in Figure 4.3, the enrichment shock. The model presented in section 4.3.1 predicts that anionic species can stack at the interface between the enrichment region and the reservoir region during propagating CP. This behavior is accurately described as stacking because in a frame of reference moving with the enrichment shock, the anionic total species velocity does not change its sign across the shock.[7] Physically, the enrichment shock propagates at the bulk velocity,[21,30] so in a frame moving with the enrichment shock, the only component of the species velocity is due to electrophoresis. The electrophoretic velocity is always negative, and therefore, does not cross zero at the shock front. It is possible, however, for anions to have a net inward velocity (towards the enrichment shock) in the lab frame.

When CP propagates, analytes move inwards on either side of the enrichment shock if their mobility is low enough to travel in the direction of bulk flow inside the enrichment region but high enough to travel against bulk flow in the reservoir region. This condition can be written as: $\nu_{i,rc}^{*crit} < \nu_i^* < \nu_{i,e}^{*crit}$. Analytes which do not meet this condition can still stack on the enrichment shock provided $\nu_{i,rc}^{*crit} < \nu_{i,e}^{*crit}$. If this second condition is met, analyte ions traveling towards the shock will slow down once they reach the shock, causing an increase in concentration.

Enrichment shock stacking was described analytically by Zangle *et al.*[29] and computationally by Plecis *et al.*,[28] who called this type of stacking cathodic counter gradient focusing, or CCGF. Zangle *et al.* presented results for two specific buffer cases in terms of a Dukhin number and the nondimensional mobility of the focusing species and correctly predicted the observed stacking behavior. The latter paper also presented experiments in which the enrichment region shock was used to stack and separate ions on the basis of their electrophoretic mobilities. This is possible because, in propagating CP, the enrichment shock is a weak shock[21,30] which creates an order 100 μm long[21] region with gradients in concentration and electric field. In contrast, the strong shock of the depletion region shock is typically much shorter (roughly on the order of the microchannel width), and, therefore, not typically appropriate for separation. In contrast, the length of the enrichment shock is typically large compared to the ~10 μm peak widths of focused species; and so species visibly separate.[29] To date, we have not been able to (and have not seen in published work) significant separation resolution achieved using enrichment shocks. We hypothesize that the relatively low ratio of electric fields across these interfaces simply yield low peak capacity; further, preconcentration is limited to order 100x.[29,56]

Papers by Hlushkou *et al.*[56] and Dhopeshwarkar *et al.*[33] each presented an enrichment region stacking scheme along with a supporting computational model. As summarized in Table 4.1, these experimental results agreed well with the prediction of enrichment shock stacking.

In experiments with the same buffer and channel conditions as Zangle *et al.*[29] we noted stacking on the enrichment shock, as predicted by theory (see Figure 4.6(b)).

4.4 Section Conclusions

In this chapter we used the results of Mani *et al.*[30] to predict the behavior of cationic and anionic analytes in a microchannel-nanochannel system with negative wall charge. This included an extension of this theory to predict the conditions required for focusing or stacking of analytes in systems with CP. We predict stacking and/or focusing at four interfaces which can occur in a microchannel-nanochannel-microchannel system. We presented a comparison of this theory to published experimental data. Again we found good agreement between the reported cases from literature and the extension of the published analytical theory of Mani *et al.*[30] and Zangle *et al.*[21] presented here which predicts the existence and location of stacking and/or focusing regions.

Overall, the theory we summarize and validate in view of experimental data can be used to understand and interpret the effects of CP on analyte transport in systems containing both micro- and nanochannels.

5 Temporal Variations in Nanochannel Conductance and Concentration

In this chapter we present the first simultaneous measurements of background electrolyte concentration and channel conductance in nanofluidic systems. We find that channel conductance is linearly proportional to the measured concentration. We also evaluate the description of nanofluidic channels given by the analytical model of Mani *et al.*[30] We find that while their model captures some trends in the measured nanochannel concentration, our observation at two different experimental conditions of a large, transient increase in concentration is not predicted by their theory.

5.1 Introduction

Fabrication technology has enabled fluidic channels with length scales of order 1-100 nm.[23,90-91] These nanofluidic devices exploit heights on the order of the Debye length,[12-13] apertures on the order of biomolecule size,[14-15] or dimensions such that the number of ions associated with EDLs is comparable to the number of ions inside the channel in the absence of wall charge[16-17,80] for biological and chemical analysis. However, understanding and optimizing these devices requires evidence and studies of basic nanofluidic electrokinetics. In this paper we present experimental results describing the behavior of (diffuse) ion concentration inside nanofluidic systems. These data refute the standard assumptions made about these systems (e.g., that ion density in the channels is steady state). We also evaluate the descriptions of (internal) nanofluidic channel ion density given by the analytical model of Mani *et al.*[30]

Investigations into nanochannel physics have focused on predicting and describing nanochannel conductance measurements.[36-38,92-93] Experiments with AC applied field showed that nanochannel conductance can be modeled as the sum of the conductance due to the concentration inside the nanochannel plus a conductance associated with the wall charge.[37] Extension of this model to experiments with DC applied fields has often led to the frequently made assumption that nanochannel concentration does not change when an electric field is applied.[13,15,40,50,83,94-96] Recent modeling work on concentration polarization, however, suggests that nanochannel concentration should change over time to maintain a balance of ionic fluxes between the nanochannel and adjacent fluidic elements such as end-channel reservoirs or larger scale microchannels.[30,93,97]

In particular, Mani *et al.*[30] and Zangle *et al.*[21] showed that concentration shock waves will propagate from microchannel-nanochannel interfaces when:

$$c_r^* h_n^* < \max(\nu_{2n}^*, 2\nu_{2n}^* - 1), \tag{5.1}$$

where $c_r^* h_n^* = (\nu_1 z_1 - \nu_2 z_2) F h_n c_r / (-2\nu_1 \sigma)$ is an inverse Dukhin number which describes the ratio of bulk to surface conductance, and $\nu_{2n}^* = \nu_2 z_2 F \eta / \zeta \varepsilon$ is the mobility of the co-ion to the wall charge nondimensionalized by the electroosmotic mobility. Here, c_r is the reservoir concentration. h_n is the nanochannel height; ν_1 and ν_2 are the mobilities of the positive and negative species; z_1 and z_2 are the valences of the positive and negative species, σ is wall charge, ζ is the zeta potential, *F* is Faraday's constant, ε is permittivity and η is viscosity. Under these conditions, the concentration inside the nanochannel at steady state is given by:

$$c_n/c_r = 0 \text{ for } \nu_{2n}^* < 1 \text{ and } c_n/c_r = \left(\nu_{2n}^* - 1\right) / \left(c_r^* h_n^*\right) \text{ for } \nu_{2n}^* \geq 1 \tag{5.2}$$

Finally, the concentration inside the nanochannel for cases without propagation is predicted to be:

$$c_n/c_r = 1 - \nu_{2,n}^* / \left(c_r^* h_n^*\right) \tag{5.3}$$

Equations (5.2) and (5.3) indicate that, for all conditions, the concentration inside a nanochannel should change over time when an electric field is applied, and in some conditions (propagating CP) the nanochannel concentration will be independent of the reservoir concentration given the same initial nanochannel surface charge density.* Predictions of nanochannel initial to final concentration (c_n/c_r) based on Equations (5.2) and (5.3) are plotted in Figure 5.1.

---

* In terms of the nondimensional concentration, $c_n^* h_n^* = (\nu_1 z_1 - \nu_2 z_2) F h_n c_n / (-2\nu_1 \sigma)$, we can write $c_n^* h_n^* = 0$ for $\nu_{2n}^* < 1$ and $c_n^* h_n^* = \left(\nu_{2n}^* - 1\right)$ for $\nu_{2n}^* \geq 1$.

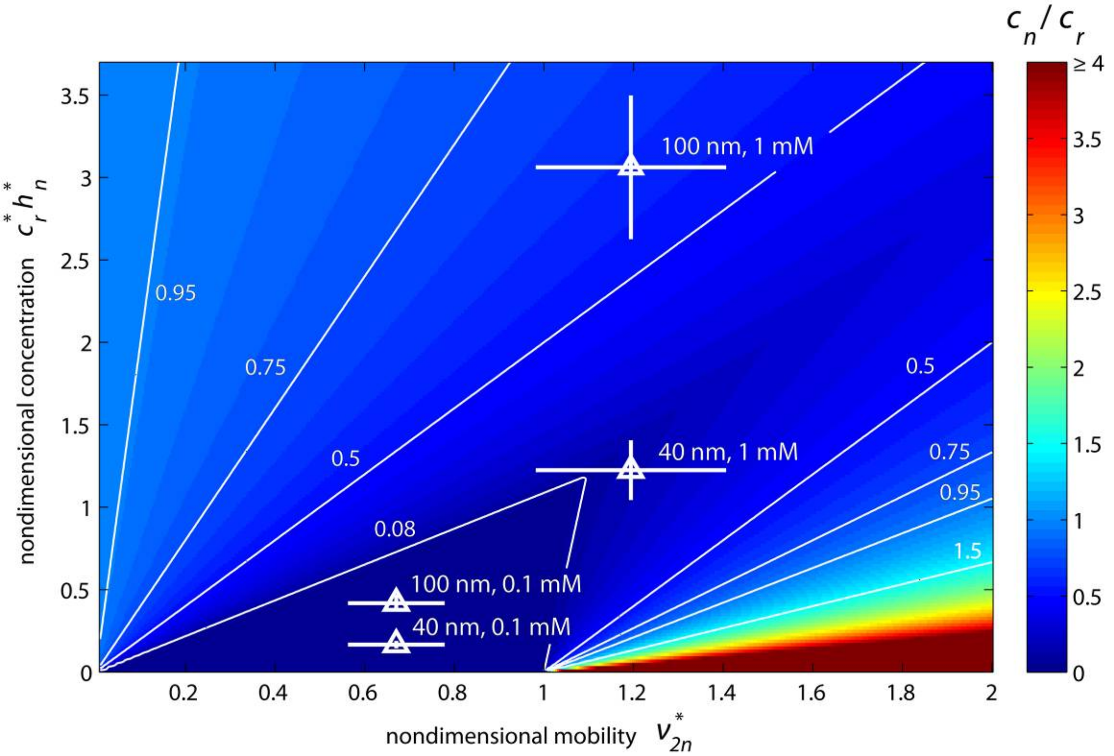

Figure 5.1 Analytical results for ratio of final nanochannel concentration to reservoir concentration, c_n/c_r. Symbols represent experimental measurements scaled with independently measured zeta potential and ion mobility. Error bars represent 95% confidence intervals on the parameters v_{2n}^* and $c_r^* h_n^*$ based on a propagation of measurement uncertainty analysis.[98] c_n/c_r. values from these experimental conditions are shown in Table 5.1, below.

Table 5.1 Summary of experimental results and analytical predictions based on the theory of Mani *et al.*[30] Uncertainty bars on measured values are 95% confidence intervals on the mean value based on *N* measurements at each condition. Predicted c_n/c_r values are reported as a nominal value followed by a range of predictions

h_n (nm)	c_r (mM)	N	meso-state c_n/c_r	final-state c_n/c_r	predicted c_n/c_r
40	0.1	4	0.10 +/- 0.06	0.10 +/- 0.06	0 (0, 0)
40	1	10	0.08 +/- 0.06	0.08 +/- 0.06	0.16 (0.06, 0.39)
100	0.1	8	0.16 +/- 0.06	13 +/- 2	0 (0,0)
100	1	6	0.75 +/- 0.17	1.7 +/-0.6	0.61 (0.46, 0.72)

Recent experimental work has explored the effects of concentration polarization (CP) on the concentration and electric fields within the microchannels of microchannel-nanochannel systems.[21,27-28,32] However, we are not aware of studies which have measured directly the background electrolyte inside a nanochannel under an applied electric field. Such measurements are necessary to evaluate Equations (5.2)-(5.3) and to examine the assumption that nanochannel concentration is equal to an initial value (e.g., an ion distribution set by an equilibrium at zero applied field).

In this letter, we present (to our knowledge, the first) simultaneous ionic current and background electrolyte concentration measurements inside a nanochannel. The data show that nanochannel conductance is a strong function of time and can vary over an order of magnitude during a single measurement. The data also show that the ion concentration inside the nanochannel is a strong function of time, refuting previous assumptions that nanochannel concentration is directly set by the reservoir concentration or the initial condition.[13,15,40,50,83,94-96] We find that the temporal variations in nanochannel conductance are well described by a linear fit to the measured concentration inside the channel, as expected. We also find that an analytical theory of concentration polarization (CP) captures some of the early trends in nanochannel concentration. In some cases, the concentration briefly establishes a meso state and then transitions to a final state which is often significantly higher ion density. In these cases, this transition and final state phenomenon is not predicted by previous CP models including our own[30],[21] Overall, this work suggests that nanochannel concentration dynamics, and perhaps CP-coupled transport, play a role in determining nanochannel conductance.

5.2 Experimental Setup

Channels were fabricated by dry-etching of fused silica followed by dry bonding of cover wafers to form sealed channels.[13] Figure 5.2 shows a schematic of the two channel designs used in this study. The channel in Figure 5.2(a) consists of a 3.6 cm long nanochannel between two end channel reservoirs (40 μL). The nanochannels were either 40 or 100 nm deep and 10 μm wide. The channel in Figure 5.2(b) consists of a 100 μm long, 100 nm deep, 20 μm wide nanochannel between two 1 μm deep, 20 μm wide microchannels.

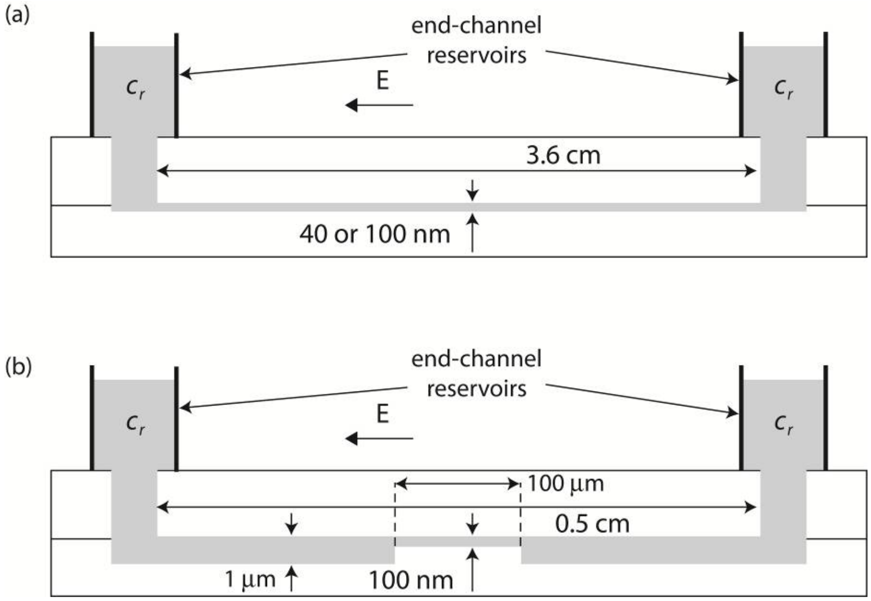

Figure 5.2 Channel geometries used in nanochannel concentration study. (a) 3.6 cm long nanochannel between two reservoirs. (b) 100 μm long nanochannel between two 0.5 cm long, 1 μm deep microchannels. The channel layout shown in (a) consists of a 40 or 100 nm deep channel between two reservoirs. The layout shown in (b) consists of a 1 μm deep microchannel, a 100 nm deep channel, and a second 1 μm deep microchannel, all between two reservoirs.

For experiments using either channel layout the system was filled by pressure-driven flow with a solution of Alexa Fluor 488 in deionized water at concentration c_r before each experiment. Concentration inside the channel was measured using epifluorescent microscopy and calibrated against images with the channel filled (flatfield) and outside the channel where no dye was present (background). As in Zangle *et al.*[21] this allows for direct quantification of the concentration of the background electrolyte inside the system. For experiments with the layout shown in Figure 5.2(a), we measured current using a high-resistance electrometer (Electrometer 6514, Keithley Instruments, Inc., Cleveland, OH) at a constant applied voltage of 1 kV. Fluorescence intensity was measured using a 60x, 0.9 NA water immersion objective (Olympus, Happauge, NY). Experiments with the design in Figure 5.2(b) were performed at constant current using of 800 pA using a high-voltage, source-and-measure power supply (Sourcemeter 2410, Keithley Instruments, Inc., Cleveland, OH). In the latter case, fluorescence intensity was measured using a 10x, NA 0.4 objective (Olympus, Happauge, NY). All fluorescence intensity measurements were made using an upright, epifluorescent microscope (Olympus IX-70, Happauge, NY) with a 0.31x demagnifier (Diagnostic Intruments, Inc., Sterling Heights, MI) to increase field of view while preserving sensitivity.

The fluorescence intensity of Alexa Fluor 488 was assumed to be linear with concentration as reported by Jung *et al.*[99] Fluorescence measurements were normalized as: $D(t) = (R(t)-B)/(I-B)$, where $D(t)$ is the reported fluorescence intensity over time, $R(t)$ is the raw fluorescence measurement, B is the average measured background fluorescence intensity (measured outside of the channel, as the channel could not be completely cleared of fluorophores between each experiment), and I is the average measured initial fluorescence intensity in the channel. Both B and I were averages of 100 image frames. Data in $D(t)$ was then averaged across the channel width (10 pixels) and over 300 pixels along the channel length. Zero measured fluorescence intensity would indicate zero relative to the background (outside of the channel) fluorescence.

5.3 Experimental Results

In this section we will describe and evaluate experimental results at four different conditions by varying nanochannel height (h_n) and reservoir concentration (c_r). Figure 5.3 shows typical example experimental results for simultaneous measurements of nanochannel ionic current and concentration performed using channels with the layout shown in Figure 5.2(a). Results for a 40 nm channel initially filled with 1 mM Alexa Fluor 488 show conductance (current in this constant voltage experiment, Figure 5.3(a)) strongly decrease followed by a gradual increase over time. This is accompanied by a strong, persistent decrease in concentration (fluorescence intensity, Figure 5.3(b)) to a value of $c_n/c_r = 0.012$. Results for a 100 nm channel initially filled with 100 mm Alexa Fluor 488 show conductance (current, Figure 5.3(c)) initially decrease followed by an increase to well over its initial value. As shown in Figure 5.3(d), this is accompanied by a transient, initial decrease in measured concentration to c_n/c_r = 0.22 followed by a strong increase over time to a final-state value of c_n/c_r = 13.8.

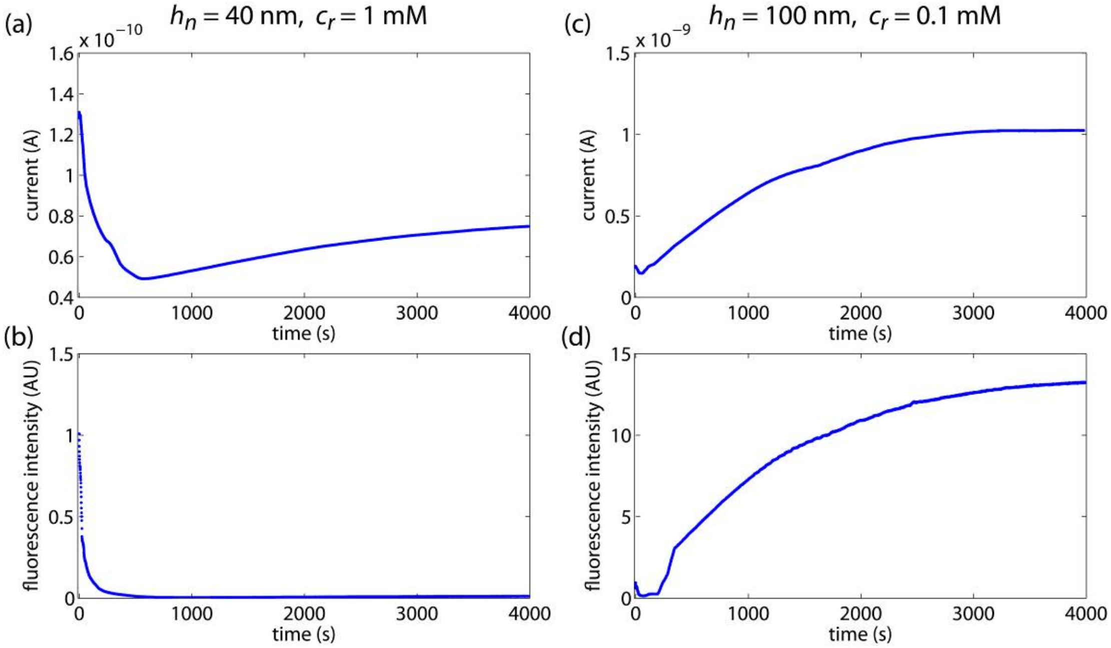

Figure 5.3 Sample experimental results showing current measurements and fluorescence intensity measurements for channels of the design shown in Figure 5.2(a) with (a) and (b) 40 nm channel with 1 mM reservoir concentration, (c) and (d) 100 nm deep channel with 100 μM reservoir concentration. At t = 0, a constant voltage of 1 kV was applied. Fluorescence intensities in (b) and (d) are averages across the channel width over a 360 μm long window and normalized relative to the initial fluorescence intensity.

Figure 5.3 shows anecdotally a strong correlation between measured concentration and conductance. To quantify the degree of this correlation we computed correlation coefficients between our simultaneous concentration and conductance measurements for each of 28 different experimental measurements at the conditions summarized in Table 5.1. Over all experiments we measured an average, linear correlation coefficient between current and fluorescence intensity of 0.90 +/- 0.04 with no significant variation among the four different experimental conditions. This correlation between conductance and ion density is consistent with, for example, the AC measurements of current measurements and model of Schoch *et al.*[37] which show that nanochannel conductance is well described by a term proportional to concentration plus a term proportional to wall charge.[†]

Figure 5.4 shows a sample spatiotemporal plot of fluorescence intensity (width averaged inttensities in the channel system versus axial position and time) in the layout shown in Figure 5.2(b). This channel was initially filled with 1 mM Alexa Fluor 488. The enrichment and depletion shocks described by Mani *et al.*[30] and Zangle *et al.*[21] are clearly visible propagating into the microchannels on the left and right of the nanochannel region. Additionally, fronts of a decreased concentration (meso-state, ending at about 20 s) and increased concentration (final-state, after about 35 s) observably propagate through the nanochannel. This two-state concentration dynamics are also shown in Figure 5.3(d) for the long, straight nanochannel design of Figure 5.2(a).

The last column of Table 5.1 presents predicted values of c_n/c_r (see Figure 5.1) based on independently measured zeta potential and mobility.[21] The propagated (expected) uncertainty in ν_{2n}^* and $c_r^* h_n^*$ for each experimental condition is reflected by uncertainty bars in Figure 5.1. Based on Figure 5.1, we present three values for each experimental condition. First, we list the predicted c_n/c_r based on the nominal computed ν_{2n}^* and $c_r^* h_n^*$. In parentheses after the nominal value are the estimated minimum and maximum values of c_n/c_r based on propagation of uncertainties.

[†] Assuming that the wall charge is constant over the duration of our experiment, which were typically short relative to the timescale for equilibrium between the wall charge and bulk solution.[60]

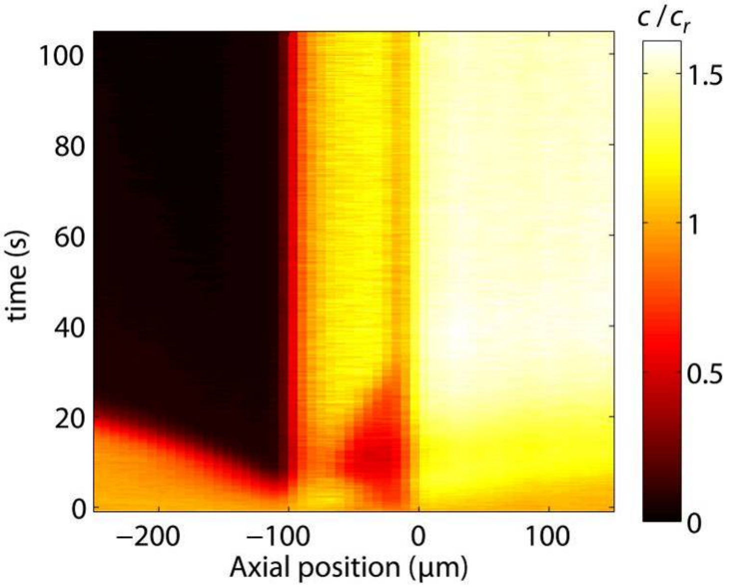

Figure 5.4 Sample spatiotemporal plot of 100 nm deep, 100 μm long nanochannel between two microchannels (of the design shown in Figure 5.2(b)). The right side of the nanochannel is located at an axial position of 0 μm. The color map corresponds to the ratio of measured width-averaged concentration (c) relative to the initial, reservoir concentration (c_r = 1 mM Alexa Fluor 488). 800 pA constant current with the cathode located at the right was applied at t = 0 s. Propagating enrichment and depletion fronts observably move away from the nanochannel interfaces. Initially, a front of low (meso-state) concentration can be seen to sweep across the nanochannel from the cathode side with c/c_r = 0.55. This is followed by a front of high (final-state) concentration moving across the nanochannel from the anode side with c/c_r = 1.17.

Trends in the final concentration for 40 nm channels and the meso-state concentration in 100 nm channel experiments agree fairly well with the analytical theory of Mani *et al.*[30] For example, Table 5.1 shows that the 40 nm, c_r = 1 mM final concentration and the 100 nm, c_r = 1 mM meso-state concentration match the predictions shown in Figure 5.1 to within (the albeit large) experimental uncertainty. Additionally, the measured final concentration for 40 nm, c_r = 100 μM and the meso-state concentration for 100 nm, c_r = 100 μM are an order of magnitude lower than the initial concentrations. This is consistent with the predicted value of zero (ignoring dissociation of water) for both of these cases. We never measured zero fluorescence intensity, but speculate that there may have been adsorbed dye on channel walls (which was not accounted for by our background subtraction during image processing).

Although trends in the meso-state concentration for the 100 nm channel experiments are captured by predictions, the final-state concentrations for the 100 nm channel measurements are not well-described by the theory. For cases where we observe a meso- and final state, the final-state concentrations are typically very much higher than the initial concentration. This meso-state transition and final value is also not captured by the computational model presented in Zangle *et al.*[21] We note that meso-state to final state transition was observed in two distinct channel geometries with 100 nm deep nanochannels. Furthermore, these channels were fabricated separately and used in separate experiments. The experiments with 40 nm deep, 3.6 cm long nanochannels (which did not show a meso to final-state transition) were performed concurrently with the 100 nm deep, 3.6 nm long channels. Therefore, we do not believe the observed meso to final state transition is an artifact of the specific prototypes or experiment design. We are unable, however, to provide a model describing the final concentration in these cases.

5.4 Summary

We presented the first simultaneous measurements of nanochannel conductance and background electrolyte concentration. In all cases, the nanochannel concentration was observed to change with time, refuting the assumption that nanochannel concentration is equal to an initial value (e.g., set by equilibrium conditions at the start of the experiment). Our nanochannel concentration measurement values correlate well with measured transients of nanochannel conductance. This correlation is consistent with the view that nanochannel conductance can be expressed (as in Schoch *et al.*[37]) as the sum of a bulk conductance plus a conductance associated with ions shielding wall charge.[37] We found that, in some cases, nanochannel conductance quickly trends to a meso state, but then transitions to a final state of increased ion density. Interestingly, this meso-state is fairly well described by the theory of Mani et al.[30] but the transition to and value of the final ion density is not well described. Overall, the measurements show more work is likely needed to both quantify nanochannel dynamics experimentally and incorporate new physical mechanisms into models.

6 Conclusions and Future Work

In this chapter we summarize the overall conclusions and contributions of this dissertation. We also present recommendations for future work based on this thesis.

6.1 Conclusions and Contributions

1. We developed a system for direct measurement of the dynamics of background electrolyte concentration inside a microfluidic-nanofluidic system using epifluorescent microscopy. This system uses a pH-insensitive fluorescent dye and its counter-ion as the background electrolyte.
2. We validated the description of the effects of CP on microchannel concentration given by the analytical model of Mani *et al.*[30] using computations and experiments. In particular, this work showed that:
    a. Enrichment and depletion shock velocities are linearly proportional to the current through the series microchannel-nanochannel-microchannel system.
    b. The enrichment region concentration is not a function of applied current.
    c. The analytical theory of Mani *et al.*[30] is a fair predictor of propagating vs. non-propagating CP conditions.
    d. The ratio of enrichment to depletion shock velocities can be related to the enrichment region concentration using a simple control volume argument. This relationship reveals that CP in a microfluidic-nanofluidic system primarily redistributes ionic strength from one side of the nanochannel to the other.
3. We developed a channel conditioning procedure for experiments using nanofluidic devices which cannot be cleaned by conventional means (which require etching of the channel surface and corresponding changes in the nanochannel characteristic dimension).
4. We presented measurements of zeta potential for two electrolyte systems made up of a fluorescent dye and its counter-ion.

5. We derived a model of the effects of constant voltage on CP propagation. We validated this model through experiment and computation. This work showed that, under constant applied voltage, CP enrichment and depletion fronts propagate as $x \sim t^{1/2}$.
6. We presented a model for the effect of CP on cation transport in microfluidic-nanofluidic systems. We validated this model through comparison to published experiments.
7. We presented a new model for the effects of CP on analyte transport in microfluidic-nanofluidic systems. We validated this model through comparison to our own work and published experiments.
8. We presented the first simultaneous measurements of nanochannel conductance and concentration.
9. We showed that, under an applied electric field, the concentration inside a nanochannel is a strong function of time. This work experimentally verifies that the standard assumption of nanochannel concentration equal to reservoir concentration does not hold for DC nanochannel conductance measurements.
10. We demonstrated that transient, DC nanochannel conductance is a linear function of the concentration inside a nanochannel.
11. We showed that the analytical theory of Mani *et al.*[30] does a fair job of predicting some trends in nanochannel concentration under an applied electric field. However, we also provided the first observations of a transition from a meso to final-state concentration inside of nanochannels. This transition is not captured by the model of Mani *et al.*[30].

6.2 Recommendations for Future Work

Below are a few summary recommendations for future work.

1. All microchannel-nanochannel experiments were performed with channel widths of 20 μm and microchannel heights of 1 μm. The effects of varying channel heights and widths should be explored further.
2. Axial variations in channel width may impact shock propagation rates throughout a microchannel-nanochannel system. These effects will be studied

analytically in a forthcoming paper by A. Mani and M. Bazant.[100] The effects of variable width channels on propagation of CP should be examined experimentally.

3. Peclet number effects have been demonstrated in two analytical papers[1,21] and one computational paper[28] related to this work (here Peclet is defined as $Pe = UL / D$, where U is the bulk fluid velocity, L is the channel length and D is diffusivity). In particular, the computational model of Plecis *et al.*[28] where applied voltage across a microchannel-nanochannel system was varied suggests that Peclet number can have a significant effect on analyte focusing and stacking behaviors. All experiments in this work, however, were at moderately high Peclet numbers, where the shock thickness is small relative to the channel length. The effects of low Peclet number on microchannel concentration should be demonstrated experimentally. Additionally, the effects of Peclet number on analyte transport should be examined further in the context of the analytical model presented in this work
4. Further experiments with well quantified background electrolyte, analyte species and surface properties should be carried out to further verify the analytical predictions for both cationic and anionic analytes.
5. Preliminary results indicated that the enrichment front may be used to simultaneously preconcentrate and separate analyte anions.[29] Although this technique showed low resolution separations, the limits of this technique should be explored further, either through computational modeling or experiments
6. Nanochannel concentration and conductance experiments were only performed at two nanochannel heights and two ion concentrations, for four total conditions. Experiments should be attempted at other conditions as well.
7. All microchannels in this study were fabricated using photoresist as an etch mask for a plasma, dry etch process. This limited the channel depth to less than 2 μm. Additional devices should be fabricated using a chrome etch mask and wet etched microchannels to achieve larger depths.

8. Additional channels should be fabricated using electron-beam lithography. This would allow for strong in-plane variations in channel width, down to tens of nanometers.
9. In order to vary ion mobility without sacrificing the favorable properties of Alexa Fluor dyes, experiments should be performed with variants of Alexa Fluor other than Alexa Fluor 488 succinimidyl ester.

7 Bibliography

[1] Zangle, T. A., Mani, A., and Santiago, J. G., "Theory and experiments of concentration polarization and ion focusing at microchannel and nanochannel interfaces," *Chemical Society Reviews (in press),* 2009.

[2] Squires, T. M. and Quake, S. R., "Microfluidics: Fluid physics at the nanoliter scale," *Reviews of Modern Physics,* vol. 77, pp. 977-1026, 2005.

[3] Beebe, D. J., Mensing, G. A., and Walker, G. M., "Physics and applications of microfluidics in biology," *Annual Review of Biomedical Engineering,* vol. 4, pp. 261-286, 2002.

[4] Easley, C. J., Karlinsey, J. M., Bienvenue, J. M., Legendre, L. A., Roper, M. G., Feldman, S. H., Hughes, M. A., Hewlett, E. L., Merkel, T. J., Ferrance, J. P., and Landers, J. P., "A Fully Integrated Microfluidic Genetic Analysis System with Sample-In-Answer-Out Capability," *Proceedings of the National Academy of Sciences of the United States of America,* vol. 103, pp. 19272-19277, 2006.

[5] Bharadwaj, R., Santiago, J. G., and Mohammadi, B., "Design and optimization of on-chip capillary electrophoresis," *Electrophoresis,* vol. 23, pp. 2729-2744, 2002.

[6] Jung, B., Bharadwaj, R., and Santiago, J. G., "Thousandfold signal increase using field-amplified sample stacking for on-chip electrophoresis," *Electrophoresis,* vol. 24, pp. 3476-3483, 2003.

[7] Bharadwaj, R., Huber, D. E., Khurana, T. K., and Santiago, J. G., "Taylor Dispersion in Sample Preconcentration Methods," in *Handbook of Capillary and Microchip Electrophoresis and Asociated Microtechniques*, J. P. Landers, Ed., 3rd ed Boca Raton: CRC, 2008, pp. 1085-1120.

[8] Jung, B., Zhu, Y., and Santiago, J. G., "Detection of 100 aM fluorophores using a high-sensitivity on chip CE system and transient isotachophoresis," *Analytical Chemistry,* vol. 79, pp. 345-349, 2007.

[9] Khurana, T. K., "On-chip isotachophoresis assays for high sensitivity electrophoretic preconcentration, separation, anda indirect detection," Ph.D., Mechanical Engineering, Stanford University, Stanford, CA, 2008.

[10] Khurana, T. K. and Santiago, J. G., "Sample Zone Dynamics in Peak Mode Isotachophoresis," *Analytical Chemistry,* vol. 80, pp. 6300-6307, 2008.

[11] Khurana, T. K. and Santiago, J. G., "Preconcentration, separation, and indirect detection of nonfluorescent analytes using fluorescent mobility markers," *Analytical Chemistry,* vol. 80, pp. 279-286, 2008.

[12] Pennathur, S. and Santiago, J. G., "Electrokinetic transport in nanochannels. 1. Theory," *Analytical Chemistry,* vol. 77, pp. 6772-6781, 2005.

[13] Pennathur, S. and Santiago, J. G., "Electrokinetic transport in nanochannels. 2. Experiments," *Analytical Chemistry,* vol. 77, pp. 6782-6789, 2005.

[14] Howorka, S. and Siwy, Z., "Nanopore analytics: sensing of single molecules," *Chemical Society Reviews,* vol. 38, pp. 2360-2384, 2009.

[15] Sexton, L. T., Horne, L. P., Sherrill, S. A., Bishop, G. W., Baker, L. A., and Martin, C. R., "Resistive-pulse studies of proteins and protein/antibody complexes using a conical nanotube sensor," *Journal of the American Chemical Society,* vol. 129, pp. 13144-13152, 2007.

[16] Wang, Y.-C., Stevens, A. L., and Han, J., "Million-fold preconcentration of proteins and peptides by nanofluidic filter," *Analytical Chemistry,* vol. 77, pp. 4293-4299, 2005.

[17] Zhou, K., Kovarik, M. L., and Jacobson, S. C., "Surface-charge induced ion depletion and sample stacking near single nanopores in microcluidic devices," *Journal of the American Chemical Society,* vol. 130, pp. 8614-8616, 2008.

[18] Pennathur, S., Baldessari, F., Santiago, J. G., Kattah, M. G., Steinmen, J. B., and Utz, P. J., "Free-solution oligonucleotide separation in nanoscale channels," *Analytical Chemistry,* vol. 79, pp. 8316-8322, 2007.

[19] Sen, Y.-H. and Karnik, R., "Investigating the translocation of λ-DNA molecules through PDMS nanopores," *Analytical and Bioanalytical Chemistry,* vol. 394, pp. 437-446, 2009.

[20] Kim, S. M., Burns, M. A., and Hasselbrink, E. F., "Electrokinetic Protein Preconcentration Using a Simple Glass/Poly(dimethylsiloxane) Microfluidic Chip," *Analytical Chemistry,* vol. 78, pp. 4779-4785, 2006.

[21] Zangle, T. A., Mani, A., and Santiago, J. G., "On the propagation of concentration polarization from microchannel-nanochannel interfaces part II. Numerical and experimental study," *Langmuir,* vol. 25, pp. 3909-3916, 2009.

[22] Kim, S. J. and Han, J., "Self-sealed vertical polymeric nanoporous-junctions for high-throughput nanofluidic applications," *Analytical Chemistry,* vol. 80, pp. 3507-3511, 2008.

[23] Schoch, R. B., Han, J., and Renaud, P., "Transport phenomena in nanofluidics," *Reviews of Modern Physics,* vol. 80, pp. 839-883, 2008.

[24] Wang, Y.-C. and Han, J., "Pre-binding range and sensitivity enhancement for immuno-sensors using nanofluidic preconcentrator," *Lab on a Chip,* vol. 8, pp. 392-394, 2008.

[25] Hatch, A. V., Herr, A. E., Throckmorton, D. J., Brennan, J. S., and Singh, A. K., "Integrated preconcentration SDS-PAGE of proteins in microchips using photopatterned cross-linked polyacrylamide gels," *Analytical Chemistry,* vol. 78, pp. 4976-4984, 2006.

[26] Salieb-Beugelaar, G. B., Teapal, J., Nieuwkasteele, J. v., Wijnperle, D., Tegenfeldt, J. O., Lisdat, F., Berg, A. v. d., and Eijkel, J. C. T., "Field-dependent DNA mobility in 20 nm high nanoslits," *Nano Letters,* vol. 8, pp. 1785-1790, 2008.

[27] Kim, S. J., Li, L. D., and Han, J., "Amplified electrokinetic response by concentration polarization near nanofluidic channel," *Langmuir,* vol. 25, pp. 7759-7765, 2009.

[28] Plecis, A., Nanteuil, C., Haghiri-Gosnet, A.-M., and Chen, Y., "Electropreconcentration with charge-selective nanochannels," *Analytical Chemistry,* vol. 80, pp. 9542-9550, 2008.

[29] Zangle, T. A., Mani, A., and Santiago, J. G., "Novel device for electrophoretic focusing and separation at a microchannel-nanochannel interface," in *Eleventh*

International Conference on Miniaturized Systems for Chemistry and Life Sciences (µTAS2007), Paris, France, 2007, pp. 1204-1206.

[30] Mani, A., Zangle, T. A., and Santiago, J. G., "On the propagation of concentration polarization from microchannel-nanochannel interfaces part I. Analytical model and characteristic analysis," *Langmuir,* vol. 25, pp. 3898-3908, 2009.

[31] Pu, Q., Yun, J., Temkin, H., and Liu, S., "Ion-Enrichment and Ion-Depletion Effect of Nanochannel Structures," *Nano Letters,* vol. 4, pp. 1099-1103, 5/19/04 2004.

[32] Kim, S. J., Wang, Y.-C., Lee, J. H., Jang, H., and Han, J., "Concentration Polarization and Nonlinear Electrokinetic Flow near a Nanofluidic Channel," *Physical Review Letters,* vol. 99, p. 044501, 2007.

[33] Dhopeshwarkar, R., Crooks, R. M., Hlushkou, D., and Tallarek, U., "Transient effects on microchannel electrokinetic filtering with an ion-permselective membrane," *Analytical Chemistry,* vol. 80, pp. 1039-1048, 2008.

[34] Goosen, M. F. A., Sablani, S. S., Al-Hinai, H., Al-Obeidani, S., Al-Belushi, R., and Jackson, D., "Fouling of reverse osmosis and ultrafiltration membranes: A critical review," *Separation Science and Technology,* vol. 39, pp. 2261-2297, 2004.

[35] Chan, S. H. and Xia, Z. T., "Polarization effects in electrolyte/electrode-supported solid oxide fuel cells," *Journal of Applied Electrochemistry,* vol. 32, pp. 339-347, 2002.

[36] Stein, D., Kruithof, M., and Dekker, C., "Surface-charge-governed ion transport in nanofluidic channels," *Physical Review Letters,* vol. 93, p. 035901, 2004.

[37] Schoch, R. B., van Lintel, H., and Renaud, P., "Effect of the surface charge on ion transport through nanoslits," *Physics of Fluids,* vol. 17, p. 100604, 2005.

[38] Baldessari, F. and Santiago, J. G., "Electrokinetics in Nanochannels. Part II. Mobility Dependence on Ion Density and Ionic Current Measurements," *Journal of Colloid and Interface Science,* vol. 325, pp. 539-546, 2008.

[39] Lyklema, J., *Fundamentals of Interface and Colloid Science, Volume II: Solid-Liquid Interfaces* vol. 2. London: Academic Press, 1995.

[40] Burgreen, D. and Nakache, F. R., "Electrokinetic Flow in Ultrafine Capillary Slits," *The Journal of Physical Chemistry,* vol. 68, pp. 1084-1091, 1964.

[41] Karnik, R., Fan, R., Yue, M., Li, D., Yang, P., and Majumdar, A., "Electrostatic control of ions and molecules in nanofluidic transistors," *Nano Letters,* vol. 5, pp. 943-948, 2005.

[42] Dukhin, S. S. and Shilov, V. N., "Theory of static polarization of the diffuse part of the thin electric double layer of spherical particles," *Kolloidnyi Zhurnal,* vol. 31, pp. 706-713, 1969.

[43] Block, M. and Kitchener, J. A., "Polarization Phenomena in Commercial Ion-Exchange Membranes," *Journal of the Electrochemical Society,* vol. 113, pp. 947-953, 1966.

[44] Rubinshtein, I., Zaltzman, B., Pretz, J., and Linder, C., "Experimental verification of the electroosmotic mechanism of overlimiting conductance through a cation exchange electrodialysis membrane," *Russian Journal of Electrochemistry (Translation of Elektrokhimiya),* vol. 38, pp. 853-863, 2002.

[45] Rubinstein, I. and Zaltzman, B., "Electro-osmotically induced convetion at a permselective membrane," *Physical Review E,* vol. 62, pp. 2238-2251, 2000.

[46] Zaltzman, B. and Rubinstein, I., "Electro-osmotic slip and electroconvective instability," *Journal of Fluid Mechanics,* vol. 579, pp. 173-226, 2007.

[47] Nischang, I., Reichl, U., Sedel-Morgenstern, A., and Tallarek, U., "Concentration polarization and nonequilibrium electroosmotic slip in dense multiparticle systems," *Langmuir,* vol. 23, pp. 9271-9281, 2007.

[48] Tallarek, U., Leinweber, F. C., and Nischang, I., "Perspective on concentration polarization effects in electrochromatographic separations," *Electrophoresis,* vol. 26, pp. 391-404, 2005.

[49] Höltzel, A. and Tallarek, U., "Ionic conductance of nanopores in microscale analysis systems: Where microfluidics meets nanofluidics," *Journal of Separation Science,* vol. 30, pp. 1398-1419, 2007.

[50] Park, S. Y., Russo, C. J., Branton, D., and Stone, H. A., "Eddies in a bottleneck: An arbitrary Debye length theory for capillary electroosmosis," *Journal of Colloid and Interface Science,* vol. 297, pp. 832-839, 2006.

[51] Postler, T., Slouka, Z., Svoboda, M., Přibyl, M., and Šnita, D., "Parametrical studies of electroosmotic transport characteristics in submicrometer channels," *Journal of Colloid and Interface Science,* vol. 320, pp. 321-332, 2008.

[52] Plecis, A., Schoch, R. B., and Renaud, P., "On-Chip Separation and Concentration Processes Based on the Use of Charge Selective Nanochannels," in *Micro-TAS 2005*, 2005.

[53] Schoch, R. B., Caprioli, L., Bertsch, A., and Renaud, P., "Measurements of protein preconcentration obtained on-chip by using an electric field across a nanochannel," in *Nanotech*, Montreux, Switzerland, 2005.

[54] Datta, A., Gangopadhyay, J. Y. A. D. S., Temkin, H., Pu, Q., and Liu, S., "Nanofluidic channels by anodic bonding of amorphous silicon to glass to study ion-accumulation and ion-depletion effect," *Talanta,* vol. 68, pp. 659-665, 2006.

[55] Plecis, A., Svarnas, P., and Chen, Y., "Electro-preconcentration of biomolecules in nanofluidics: Concentration gradient focusing at low and high ionic strengths," in *Eleventh International Conference on Miniaturized Systems for Chemistry and Life Sciences (µTAS2007)*, Paris, France, 2007, pp. 1583-1585.

[56] Hlushkou, D., Dhopeshwarkar, R., Crooks, R. M., and Tallarek, U., "The influence of membrane ion-permselectivity on electrokinetic concentration enrichment in membrane-based preconcentration units," *Lab on a Chip,* vol. 8, pp. 1152-1162, 2008.

[57] Huang, K.-D. and Yang, R.-J., "A nanochannel-based concentrator utilizing the concentration polarization effect," *Electrophoresis,* vol. 29, pp. 4862-4870, 2008.

[58] Huang, K.-D. and Yang, R.-J., "Formation of ionic depletion/enrichment zones in a hybrid micro-/nano-channel," *Microfluidics and Nanofluidics,* vol. 5, pp. 631-638, 2008.

[59] Kim, D., Raj, A., Zhu, L., Masel, R. I., and Shannon, M. A., "Non-equilibrium electrokinetic micro/nano fluidic mixer," *Lab on a Chip,* vol. 8, pp. 625-628, 2008.

[60] Kirby, B. J. and Hasselbrink, E. F., "Zeta potential of microfluidic substrates: 1. Theory, experimental techniques, and effects on separations," *Electrophoresis,* vol. 25, pp. 187-202, 2004.

[61] Kirby, B. J. and Hasselbrink, E. F., "Zeta potential of microfluidic substrates: 2. Data for polymers," *Electrophoresis,* vol. 25, pp. 203-213, 2004.

[62] Kuo, S. M., Chang, S. J., and Wang, Y. J., "Properties of PVA-AA cross linked HEMA-based hydrogels," *Journal of Polymer Research,* vol. 6, pp. 191-196, 1999.

[63] You, J.-O. and Auguste, D. T., "Feedback-regulated paclitaxel delivery based on poly(N,N-dimethylaminoethyl methacrylate-co-2-hydroxyethyl methacrylate) nanoparticles," *Biomaterials,* vol. 29, pp. 1950-1957, 2007.

[64] Ge, S., Yi, B., and Ming, P., "Experimental determination of electro-osmotic drag coefficient in Nafion membrane for fuel cells," *Journal of the Electrochemical Society,* vol. 153, pp. A1443-A1450, 2006.

[65] Daiko, Y., Katagiri, K., and Matsuda, A., "Proton conduction in thickness-controlled ultrathin polycation/nafion multilayers prepared via layer-by-layer assembly," *Chemistry of Materials,* vol. 20, pp. 6405-6409, 2008.

[66] Song, S. and Singh, A. K., "On-chip sample preconcentration for integrated microfluidic analysis," *Analytical and Bioanalytical Chemistry,* vol. 384, pp. 41-43, 2006.

[67] Lee, J. H., Song, Y.-A., and Han, J., "Multiplexed proteomic sample preconcentration device using surface-patterned ion-selective membrane," *Lab on a Chip,* vol. 8, pp. 596-601, 2008.

[68] Lee, J. H., Song, Y.-A., Tannenbaum, S. R., and Han, J., "Increase of reaction rate and sensitivity of low-abundance enzyme assay using micro/nanofluidic preconcentration chip," *Analytical Chemistry,* vol. 80, pp. 3198-3204, 2008.

[69] Probstein, R. F., *Physicochemical Hydrodynamics: An Introduction,* Second ed. New York: John Wiley & Sons, Inc., 2003.

[70] Moin, P., *Fundamentals of Engineering Numerical Analysis*, 1st ed. Cambridge, UK: Cambridge University Press, 2001.

[71] Leveque, R. J., *Finite Volume Methods for Hyperbolic Problems*, 1st ed. Cambridge, UK: Cambridge University Press, 2002.

[72] van der Heyden, F. H. J., Stein, D., and Dekker, C., "Streaming currents in a single nanofluidic channel," *Physical Review Letters,* vol. 95, p. 116104, 2005.

[73] Panchuk–Voloshina, N., Haugland, R. P., Bishop–Stewart, J., Bhalgat, M. K., Millard, P. J., Mao, F., Leung, W.-Y., and Haugland, R. P., "Alexa Dyes, a Series of New Fluorescent Dyes that Yield Exceptionally Bright, Photostable Conjugates," *The Journal of Histochemistry & Cytochemistry,* vol. 47, pp. 1179-1188, 1999.

[74] Jacobson, S. C., Moore, A. W., and Ramsey, J. M., "Fused quartz substrates for microchip electrophoresis," *Analytical Chemistry,* vol. 67, pp. 2059-2063, 1995.

[75] Sze, A., Erickson, D., Ren, L., and Li, D., "Zeta-potential measurement using the Smoluchowski equation and the slope of the current-time relationship in electroosmotic flow," *Journal of Colloid and Interface Science,* vol. 261, pp. 402-410, 2003.

[76] Hunter, R. J., *Zeta Potential in Colloid Science*. London: Academic Press, 1981.

[77] Ehlert, S., Hlushkou, D., and Tallarek, U., "Electrohydrodynamics around single ion-permselective glass beads fixed in a microfluidic device," *Microfluidics and Nanofluidics,* vol. 4, pp. 471-487, 2007.

[78] Leinweber, F. C. and Tallarek, U., "Nonequilibrium Electrokinetic Effects in Beds of Ion-Permselective Particles," *Langmuir,* vol. 20, pp. 11637-11648, 2004.

[79] Kim, P., Kim, S. J., Han, J., and Suh, K. Y., "Stabilization of Ion Concentration Polarization Using a Heterogeneous Nanoporous Junction," *Nano Letters,* vol. 10, pp. 16-23, 2009.

[80] Zangle, T. A., Mani, A., and Santiago, J. G., "Theory and experiments of concentration polarization and ion focusing at microchannel and nanochannel interfaces," *Chemical Society Reviews,* 2010, DOI: 10.1039/b902074h.

[81] Foote, R. S., Khandurina, J., Jacobson, S. C., and Ramsey, J. M., "Preconcentration of proteins on microfluidic devices using porous silica membranes," *Analytical Chemistry,* vol. 77, pp. 57-63, 2005.

[82] Meagher, R. J., Hatch, A. V., Renzi, R. F., and Singh, A. K., "An integrated microfluidic platform for sensitive and rapid detection of biological toxins," *Lab on a Chip,* vol. 8, pp. 2046-2053, 2008.

[83] Han, J., Fu, J., and Schoch, R. B., "Molecular sieving using nanofilters: Past, present and future," *Lab on a Chip,* vol. 8, pp. 23-33, 2008.

[84] Bilenko, O., Bavrilov, D., Gorbovitski, B., Gorfinkel, V., Gouzman, M., Gudkov, G., Khozikov, V., Khozikov, O., Olga, K., Lifshitz, N., Luryi, S., Stepoukhovitch, A., Tcherevishinick, M., and Tyshko, G., "Formation of a resistive region at the anode end in DNA capillary electrophoresis," *Electrophoresis,* vol. 24, pp. 1176-1183, 2003.

[85] Chambers, R. D. and Santiago, J. G., "Imaging and quantification of isotachophoresis zones using nonfocusing fluorescent tracers," *Analytical Chemistry,* vol. 81, pp. 3022-3028, 2009.

[86] Persat, A., Suss, M. E., and Santiago, J. G., "Basic principles of electrolyte chemistry for microfluidic electrokinetics. Part II: Coupling between ion mobility, electrolysis, and acid-base equilibria," *Lab on a Chip,* vol. 9, pp. 2454-2469, 2009.

[87] Hirokawa, T., Nishino, M., Aoki, N., Kiso, Y., Sawamoto, Y., Yagi, T., and Akiyama, J.-I., "Table of isotachophoretic indices: I Simulated qualitative and quantitative indices of 287 anionic substances in the range pH 3-10," *Journal of Chromatography,* vol. 271, pp. D1-D106, 1983.

[88] Milanova, D., Chambers, R. D., and Santiago, J. G., p. unpublished work., 2009.

[89] Herr, A. E., Molho, J. I., Drouvalakis, K. A., Mikkelsen, J. C., Utz, P. J., Santiago, J. G., and Kenny, T. W., "On-Chip Coupling of Isoelectric Focusing

and Free Solution Electrophoresis for Multidimensional Separations," *Analytical Chemistry,* vol. 75, pp. 1180-1187, 2003.

[90] Abgrall, P. and Nguyen, N. T., "Nanofluidic devices and their applications," *Analytical Chemistry,* vol. 80, pp. 2326-2341, 2008.

[91] Eijkel, J. C. T. and van den Berg, A., "Nanofluidics: What is it and what can we expect from it?," *Microfluidics and Nanofluidics,* vol. 1, pp. 249-267, 2005.

[92] Baldessari, F. and Santiago, J. G., "Electrokinetics in Nanochannels. Part I. Electric Double Layer Overlap and Channel-to-Well Equilibrium," *Journal of Colloid and Interface Science,* pp. 526-538, 2008.

[93] Yossifon, G., Mushenheim, P., Chang, Y.-C., and Chang, H.-C., "Nonlinear current-voltage characteristics of nanochannels," *Physical Review E,* vol. 046305, 2009.

[94] Garcia, A. L., Ista, L. K., Petsev, D. N., O'Brien, M. J., Bisong, P., Mammoli, A. A., Brueck, S. R. J., and Lopez, G. P., "Electrokinetic molecular separation in nanoscale fluidic channels," *Lab on a Chip,* vol. 5, pp. 1271-1276, 2005.

[95] Griffiths, S. K. and Nilson, R. H., "Charged species transport, seperation, and dispersion in nanoscale channels: Autogenous electric field-flow fractionation," *Analytical Chemistry,* vol. 78, pp. 8134-8141, 2006.

[96] Schoch, R. B., Cheow, L. F., and Han, J., "Electrical detection of fast reaction kinetics in nanochannels with an induced flow," *Nano Letters,* vol. 7, pp. 3895-3900, 2007.

[97] Vlassiouk, I., Smirnov, S., and Siwy, Z. S., "Ionic Selectivity of Single Nanochannels," *Nano Letters,* vol. 8, pp. 1978-1985, 2008.

[98] Fox, R. W., McDonald, A. T., and Pritchard, P. J., *Introduction to Fluid Mechanics*, 6 ed. New York, NY: Wiley, 2003.

[99] Jung, B., Bharadwaj, R., and Santiago, J. G., "On-chip millionfold sample stacking using transient isotachophoresis," *Analytical Chemistry,* vol. 78, pp. 2319-2327, 2006.

[100] Mani, A. and Bazant, M. Z., "Desalination shock propagation in microstructures," *Physical Review E, submitted,* 2010.

[101] Pennathur, S., "Nanoscale Electrokinetic Transport," Ph.D., Mechanical Engineering, Stanford University, Stanford, CA, 2005.

[102] Zangle, T. A., Rant, R., Howe, R. T., and Santiago, J. G., "Microfluidic device with integrated nanopores for protein detection," in *Thirteenth International Conference on Miniaturized Systems for Chemistry and Life Sciences (µTAS2009)*, Jeju, Korea, 2009.

Appendix A Details of Experimental Setup

Appendix A.1 Channel Conditioning Procedure

Initially, channels were filled with DI only. It can be difficult to fill a microchannel-nanochannel device because of trapped bubbles at the microchannel-nanochannel interface. Typically, water was allowed to wick in from each reservoir individually (30 min to an hour), then 1 kV was applied across the device, periodically switching polarity. This was done for another 2-5 hours, or until most bubbles were gone (based on visual inspection under the microscope). Some small bubbles were typically dissolved into solution overnight.

Before and after each day of experiments, we cleaned our channels using DI water via pressure-driven flow (~1 atm). After cleaning, we flushed the microchannel-nanochannel devices by pressure driven flow (~1 atm) for 40 min with the electrolyte of interest, then allowed them to come to equilibrium under no-flow conditions for 5 min before the next experiment. Experiments were typically conducted on any given channel over a period of ~10 days, and nine were fabricated and used for the study. We found some channels degraded over time, making reproducible experiments difficult. To help validate reproducibility, we measured channel current at the start of each day after refilling the channel with deionized water. We retained channels for additional experiments if measured “steady-state” current was within about 20% of the average current measured when the channel was filled with deionized water. Here, “steady-state” refers to a relatively stable measured current after application of electric field for 100-1000 s. We hypothesize that the gradual degradation of performance from day to day may be due to long-term electrochemical changes of the surface.[76]

During current measurement before experiments began, strongly oscillating or steeply decreasing current was taken as evidence of trapped bubbles inside the channel (this can be confirmed by visual inspection). If bubbles were detected, the same bubble removal procedure outlined above was followed.

Completely changing channel ion density was difficult due to the long time required to change solution inside the channel by pressure driven flow. Also, the timescale for channel walls to come to equilibrium with new solution conditions is expected to be hours or days.[76] Therefore, most channels were only used with one type of electrolyte. This means a given channel was initially filled with deionized water, and refilled with deionized water at the end of every day and only filled with one type of electrolyte in between. Three to nine experiments were performed per day per channel with no noticeable dependence of the experimental results on experiment order.

Appendix A.2 Channel Fabrication

Channels were fabricated using the process described previously by Pennathur.[13,101] In order to make channels of two depths (microchannels and nanochannels) a three step etch process was used:

1. Etch alignment marks (1-2 μm deep)
2. Etch nanochannels (50-100 nm deep)
3. Etch microchannels (1-2 μm deep)

Step 1. is necessary because 50-100 nm deep alignment marks would not be visible enough to align the nanochannel and microchannel layers. If the microchannels were etched first, then the resist (3-5 μm) would not evenly coat the channel region.

Appendix A.3 Reservoir Attachment

Upchurch NanoPorts (N-123H, IDEX Corporation, Oak Harbor, WA) were used for all channel-designs and experiments listed in this thesis. Several different reservoir attachment methods were used in this study.

1. The supplied adhesive rings (N-100-01)
2. The Upchurch alternate epoxy (N-008)
3. Standard 5 or 30 minute two part epoxy

Best results were obtained using the Upchurch alternate epoxy. The adhesive rings supplied with the Upchurch NanoPorts are difficult to clamp to reservoirs located inside of a standard 4 inch wafer (channels were typically not diced out of the fused silica wafers in which they were fabricated). Standard two-part epoxies typically degraded over long duration exposure to water (over a period of several weeks). The Upchurch alternate epoxy (N-008) had excellent adhesion to fused silica even over very long times (months of storage filled with deionized water). One note, the Upchurch alternate epoxy is a two-part, liquid epoxy, therefore it must be applied sparingly to avoid wicking into the channels. If possible, apply the epoxy sparingly to the underside of the reservoir to be attached then wait for it to harden slightly (1-2 minutes) before attaching to the channel reservoir.

Appendix A.4 Imaging Setup and Image Analysis

All images were acquired using a Roper Scientific (Princeton Instruments) I-PentaMAX intensified CCD. To use the CCD camera, first turn on the temperature controller. Do not adjust the set point (-21°C). Wait for the temperature controller to stabilize at the set point temperature. Then make sure the lights are out and turn on the gain controller. First turn on the power switch (lower right), then the gain (leftmost switch), and finally, open the shutter (rightmost switch). Do not flip the middle switch for quantitative imaging. Gain can be adjusted using the knob beneath the display on the gain controller. Finally, set the microscope to send light to the side port (SP) by adjusting the selector knob on the right side of the microscope body. At this point, the camera is on and light from the microscope is directed towards it. Several pictures of the standard experimental setup are shown below:

Images were captured using Winview software from Roper Scientific. Images were analyzed using custom software written in Matlab. This software reads in the .spe data format from Winview and converts it into an array form which can be manipulated in Matlab. The speread.m code is reproduced in Appendix A.6. Then, the images are background and flatfield corrected as: $D(t) = (R(t)-B)/(F-B)$, where $D(t)$ is the sequence of data images over time, $R(t)$ is the sequence of raw images, F is the mean flatfield image, and B is the mean background image. F was taken with the channel filled with a uniform concentration of dye. B was taken either with the channel empty (no dye) or at a location just outside (and parallel to) the channel where no stray fluorescence from the channel was visible. Next, the data images were rotated a small amount to make the channel image parallel to the pixel rows. Then, a custom ROI was defined in the software (this corresponds to the channel width and length inside of the field of view). To make spatiotemporal images, each data image (in a given time series) was averaged over the width of the channel in the custom ROI, giving, at each time period, a vector of intensity vs. axial position. These intensities were then plotted as a colormap vs. axial position and time using the Matlab command imagesc or image.

For experiments with long straight nanochannels each data image was averaged over the entire custom ROI to give a single average intensity value at each measurement time. The field of view in these experiments was very short due to the high magnification objective used to be able to image low concentrations of dye inside a 40 or 100 nm deep nanochannel. Therefore, spatiotemporal plots from these experiments typically showed ‘fronts’ moving across the field of view over two or three images, and so, no reliable front velocity data was captured from these images.

In order to protect the sensitive CCD camera, several precautions were taken whenever the CCD was on. First, whenever possible, the room lights were left off. Room lights are bright enough to damage the CCD when the camera gain is on. Before turning on the room lights *two* of the following safety measures were put in place (two gives redundancy any of these measures alone should be enough to prevent stray light from damaging the CCD)

1. Shutter switch on CCD controller set to Off.
2. Microscope selector knob set to eyepieces instead of SP
3. Black box set on top of the microscope stage

It is not advised that you turn the camera gain on and off as this would typically wander slightly over time, especially immediately after startup.

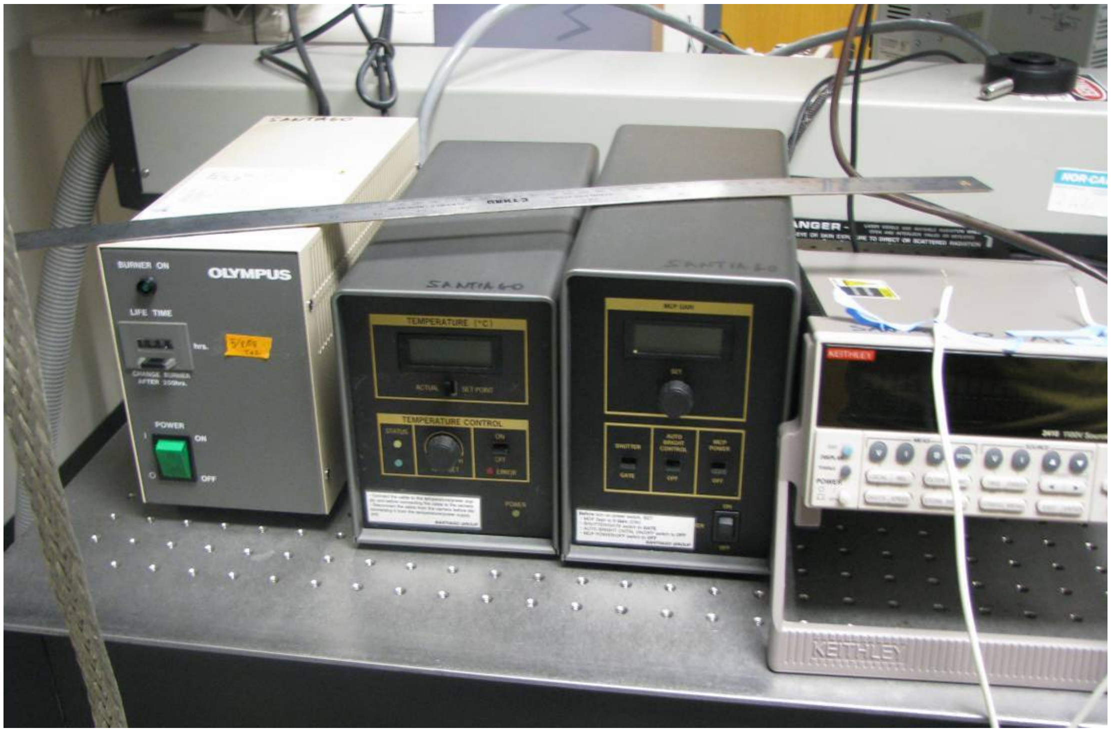

Figure A.1 Image of (from left to right) mercury bulb power supply, CCD camera temperature controller, CCD camera gain controller, Keithley sourcemeter.

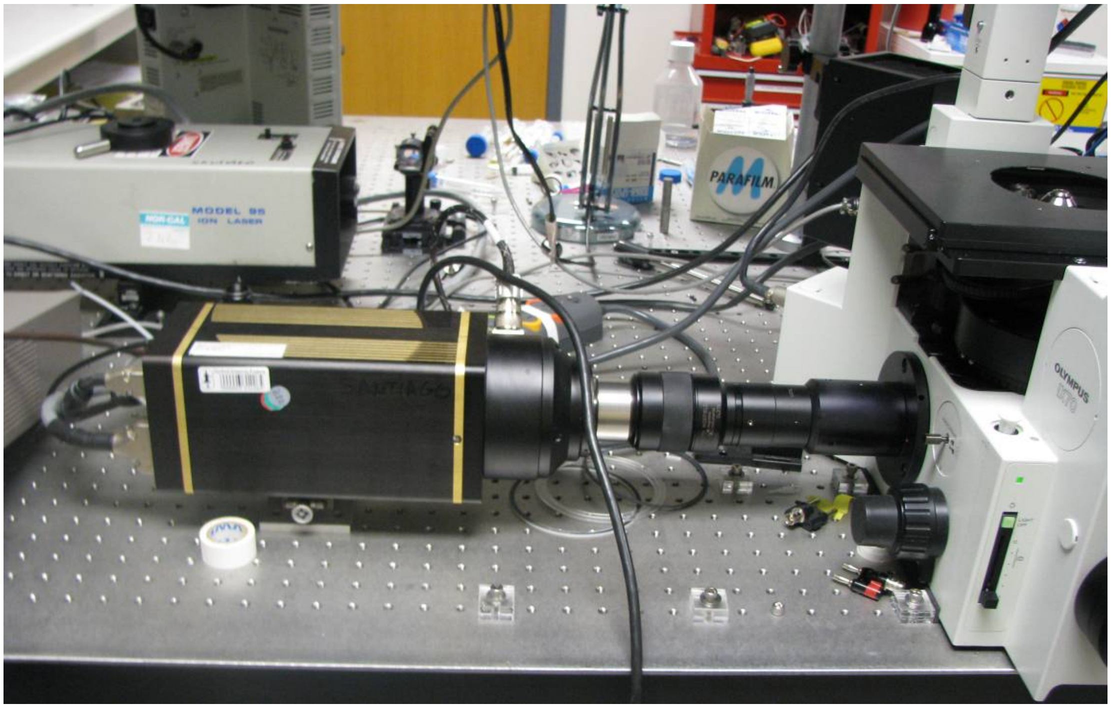

Figure A.2 Image of ICCD camera, 0.31x demagnifier, and Olympus IX70 inverted epifluorescence microscope.

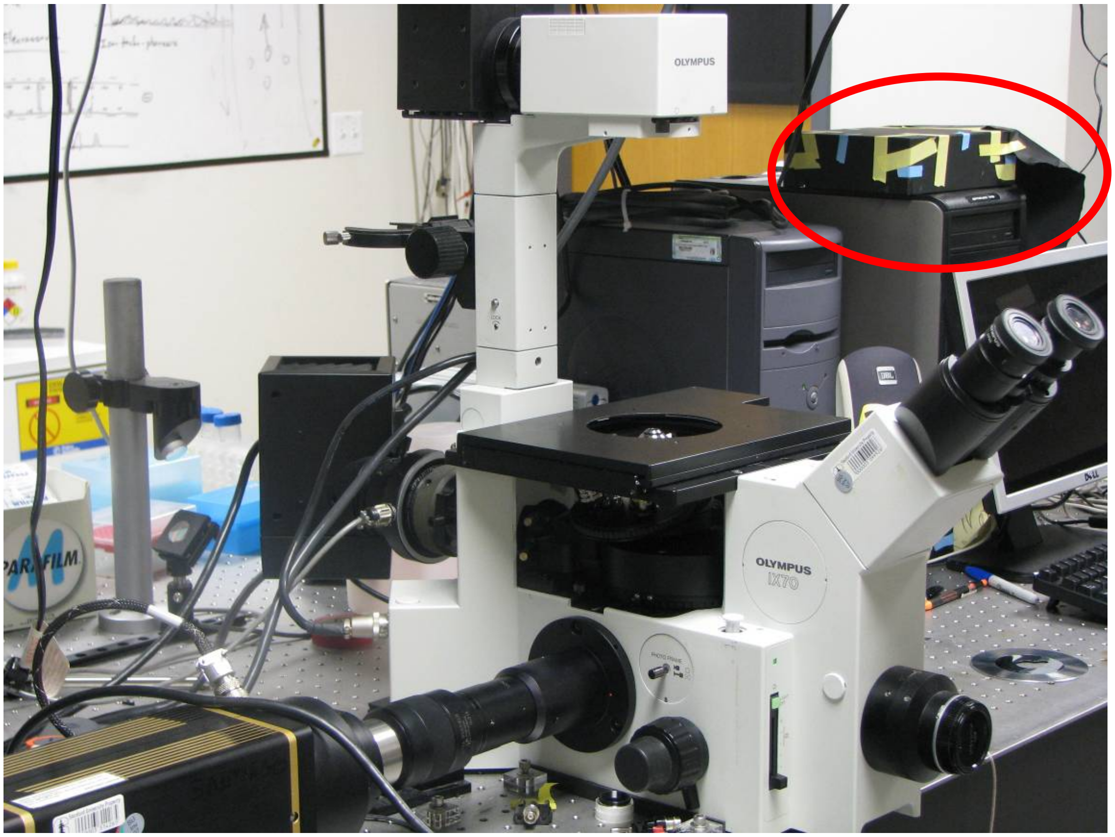

Figure A.3 Image of Olympus inverted epifluorescence microscope with the computer used to control the camera and Keithley sourcemeter in the background. To reduce background light and help protect a camera, a black box can be placed over the microscope stage during experiments. The homemade black box used during experiments is circled in red in this image. It consists of dense black cardboard taped together (on the outside only, so the inside is entirely black) with a black aluminum foil 'cape' down the right-hand side (when facing the microscope). This 'cape' shielded the microscope from stray light coming from computer monitors on the right-side of the room.

Appendix A.5 Current/Voltage Measurement Setup

All current measurements were made using a Keithley electrometer (model 6514, Keithley Instruments, Inc., Cleveland, OH) while potential was held constant using a Keithley sourcemeter (Model 2410, Keithley Instruments, Inc., Cleveland, OH) or other high-voltage power supply. Current measurements with the sourcemeter were made by controlling the sourcemeter over COM using a custom script written in

Matlab. Current measurements with the electrometer were made using a custom program written in Labview.

To reduce noise in measurements made with the sensitive electrometer, A Faraday cage was used. A picture of this Faraday cage is shown in Figure A.4, below.

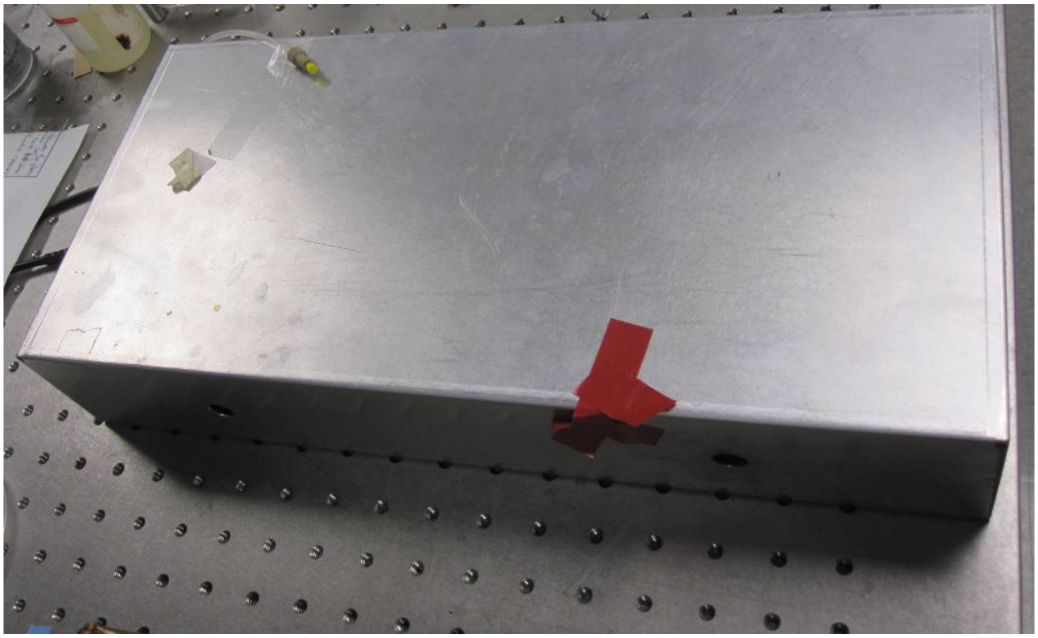

Figure A.4 Image of Faraday cage used for microchannel-nanochannel experiments. This Faraday cage was made out of aluminum and was placed in contact with the grounded, metallic top of the optics bench. The surface of the optics bench then forms the bottom of the cage.

For some experiments not described in this thesis (experiments performed using custom devices with lateral nanopores connected to microchannels[102]) Voltage measurements were made using a National Instruments USB DAQ controller (model 6211) placed inside of a copper faraday cage. This setup is shown in Figure A.5, below.

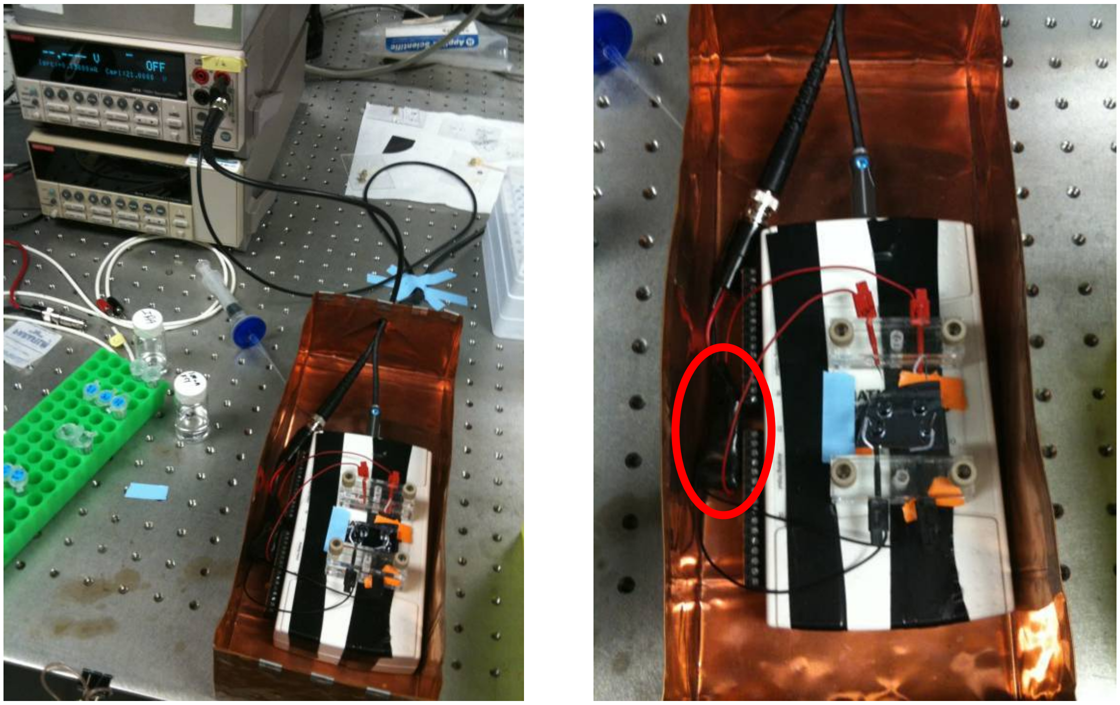

Figure A.5 Images of copper faraday cage used in microchannel-nanopore experiments. This Faraday cage is made out of copper foil which has been folded to resemble a shoe-box with a cover (not pictured). Note that the USB-DAQ card is located inside of the cage. AgCl electrodes are held in place over the custom-fabricated microchannel-nanopore device using an acrylic holder. The cables are taped to the workbench outside of the cage to reduce vibration. A Keithley electrometer was used to apply a constant current. A low-pass filter was soldered inline with the connectors to the device and isolated using shrink-wrap tubing (red circle). This filter was tuned to ~5 Hz and consists of a resistor in series with the power supply connection and a capacitor in parallel connected between the power supply output and ground.

Appendix A.6 Matlab Code to Read .spe Files

```
function [X, Xdim, Ydim, Zdim, exptime] = speread(file)
%function [X, Xdim, Ydim, Zdim, exptime] = speread(file)
%put together by Tom Zangle, with pieces from
Roper_ascii_to_mat_bin.m by
% Igal Brener from Roper Scientific, and speread.m by Haiou Shen
%8/8/06
%inputs: file, the name (with path) of the .spe file to read in
```

```
%outputs: X, the image data; Xdim, the Xdimension of the image data;
Ydim,
% the Y dimension; Zdim, the number of frames; exptime, the exposure
time
% of the images.

fid = fopen(file, 'r', 'l'); %'r' = read only, 'l' = little endian

% read in integer header information
header = fread(fid,2050,'uint16=>uint16'); % 2050 uint16 = 4100
bytes = 32800 bits
Xdim = header(22);
Ydim = header(329);
Zdim = header(724);
DataType = header(55);

%read float header info
fseek(fid,10,'bof');
exptime = fread(fid,1,'float');
fseek(fid, 4100, 'bof');

%read in image data
switch DataType
    case 0  % FLOATING POINT (4 bytes / 32 bits)
        ImMat = fread(fid,inf,'float32=>float32');
    case 1  % LONG INTEGER (4 bytes / 32 bits)
        ImMat = fread(fid,inf,'int32=>int32');
    case 2  % INTEGER (2 bytes / 16 bits)
        ImMat = fread(fid,inf,'int16=>int16');
    case 3  % UNSIGNED INTEGER (2 bytes / 16 bits)
        ImMat = fread(fid,inf,'uint16=>uint16');
end

fclose(fid);

X = reshape(ImMat,Xdim,Ydim,Zdim);
clear ImMat; %clear some memory

%permute the X and Y dimensions so that an image looks like it does
in Winview
```

Appendix B Supporting Information for Chapter 2

The contents of this appendix were previously published by Zangle, Mani and Santiago (2009)[21] and are reproduced here with minor modifications.

Anomalous Shock Propagation Behaviors

We observed oscillating enrichment region concentration and enrichment/depletion shock velocities in approximately 10 out of 81 experiments at the highest (1 mM) Alexa Fluor 488 concentration and highest applied currents (2 and 4 nA) (see Figure S-2a). Also, for several conditions, a front was observed to move into the microchannel from either the anode or cathode side well. When this front intersected the depletion or enrichment shock, respectively, the shock velocity abruptly changed (see Figure S-2c and S-2d). We hypothesize that this is due to a propagation of chemical disturbances from the reservoir (which is exposed to the room air and in which electrochemical reactions occur). The reported enrichment region concentration and shock velocities are measured before the onset of oscillations or the abrupt shift in shock velocity.

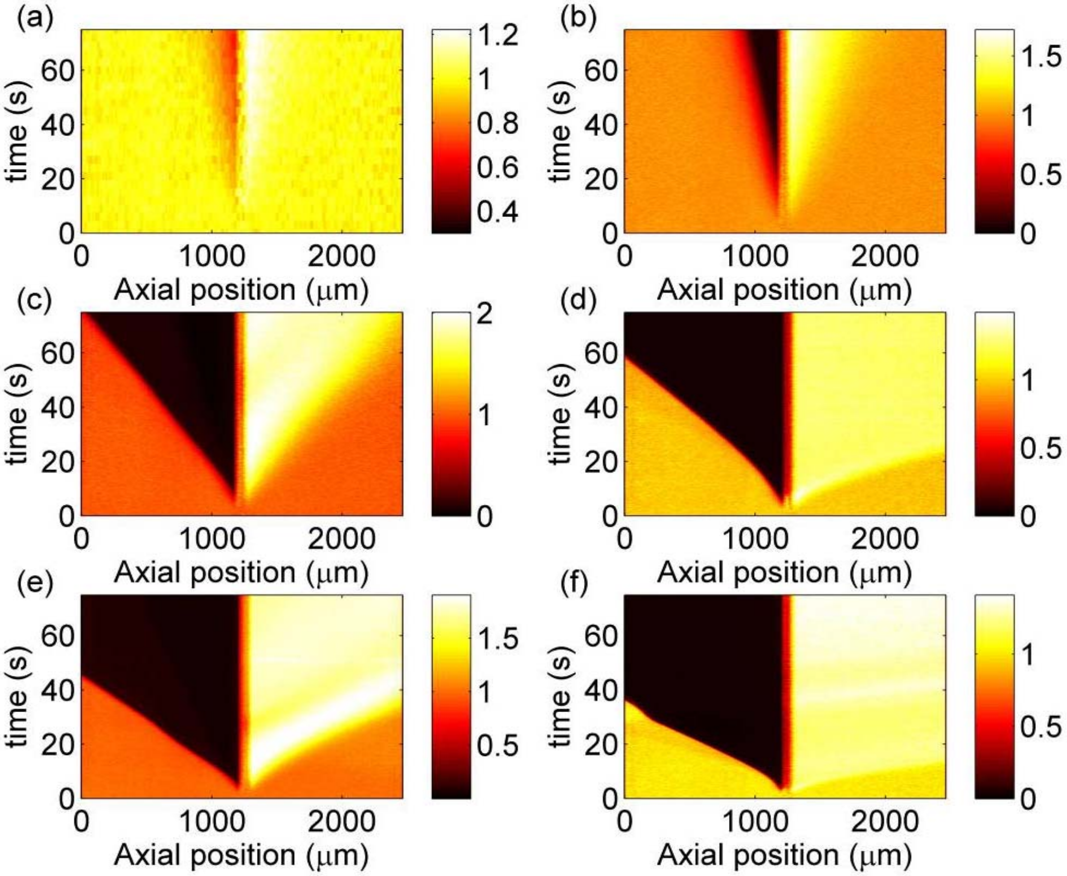

Figure B.1 Measured spatiotemporal plots showing the effect of increasing current density. (a) 50 pA, (b) 200 pA, (c) 800 pA, (d) 1.4 nA, (e) 2 nA, (f) 4 nA. The enrichment and depletion front velocities were approximately linear with applied current, as predicted by theory and shown in Figure 6. These images also show some other features of high current realizations including curved initial front velocities (d, f) and a high concentration intersecting the depletion region ((f), also discussed in Figure S-2). Images show measured, width-averaged concentration as a function of axial position and time. As indicated by the colorbars, white/yellow indicates high concentration, black indicates low concentration. We used a 100 μm long 50 nm deep nanochannel in series with two 1 μm deep microchannels. The total system length was 10 mm, and all channels were 20 μm wide. The nanochannel is visible at around *x* = 1200 μm. The system was initially filled with 1 mM Alexa Fluor 488 dye by pressure driven flow.

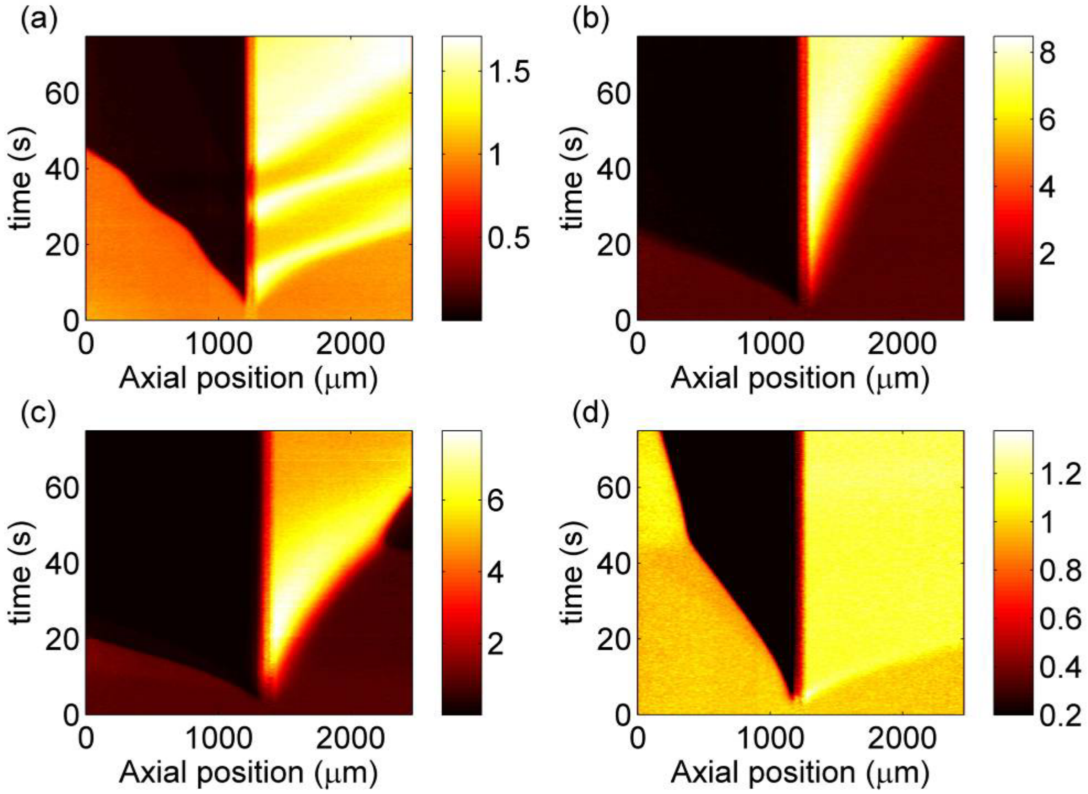

Figure B.2 Measured spatiotemporal plots showing several anomalous behaviors of propagating CP fronts. (a) Banded appearance of enrichment fronts accompanied by fluctuating depletion shock velocity for (high) 2 nA applied current and 1 mM initial concentration. Note that equation 8 of Part II predicts that a variation in the depletion front velocity should cause a change in the enrichment region concentration, as shown here. (b) Transient, curved fronts for 800 pA applied current and an initial concentration of 50 μM. As the enrichment and depletion shock velocities changed over time the enrichment region concentration also varied slowly. This may be due to changing conditions inside the nanochannel. Fronts from the (c) cathode and (d) anode side wells intersected the growing enrichment and depletion regions, respectively. The conditions for these experiments were (c) 1.4 nA, 100 μM, (d) 2 nA, 1 mM. In (c) a low concentration front intersects the enrichment region at approximately x = 2200 μm and t = 45 s. In (d) a high concentration front intersects the depletion region at approximately x = 400 μm and t = 45 s. As indicated by the colorbars, white/yellow indicates high concentration, black indicates low concentration. For all experiments shown here we used a 100 μm long 50 nm deep

nanochannel in series with two 1 μm deep microchannels. The total system length was 10 mm, and all channels were 20 μm wide. The nanochannel is visible at around x = 1200 μm. The system was initially filled with a uniform concentration of Alexa Fluor 488 dye by pressure driven flow.